

---

Electronic Thesis and Dissertation Repository

---

12-16-2021 2:00 PM

## Exploring Multimodal Cancer Cell Tracking Using Magnetic Particle Imaging and Akaluc BLI

Ryan J. Williams, *The University of Western Ontario*

Supervisor: Ronald, John A, *The University of Western Ontario*

Co-Supervisor: Foster, Paula J, *The University of Western Ontario*

A thesis submitted in partial fulfillment of the requirements for the Master of Science degree in Medical Biophysics

© Ryan J. Williams 2021

Follow this and additional works at: <https://ir.lib.uwo.ca/etd>



Part of the [Medicine and Health Sciences Commons](#)

---

### Recommended Citation

Williams, Ryan J., "Exploring Multimodal Cancer Cell Tracking Using Magnetic Particle Imaging and Akaluc BLI" (2021). *Electronic Thesis and Dissertation Repository*. 8309.  
<https://ir.lib.uwo.ca/etd/8309>

This Dissertation/Thesis is brought to you for free and open access by Scholarship@Western. It has been accepted for inclusion in Electronic Thesis and Dissertation Repository by an authorized administrator of Scholarship@Western. For more information, please contact [wlsadmin@uwo.ca](mailto:wlsadmin@uwo.ca).

## Abstract

Magnetic Particle Imaging (MPI), a novel imaging technology, offers hotspot visualization and quantification of superparamagnetic iron oxide (SPIO) labelled cells *in vivo*. Bioluminescence imaging (BLI), with the sensitive reporter Akaluc, can provide complementary information on cell viability and proliferation. Here, we combined MPI, and Akaluc BLI for a more holistic picture of cancer cell fate in mice. Breast cancer cells labelled with Akaluc and the SPIO Synomag-D, were injected into the mammary fat pad (MFP) of mice and imaged on BLI and MPI for 2-weeks. Over this period, BLI signal increased due to tumour progression, while MPI signal decreased due to probe dilution in proliferating cells. Both modalities detected metastases, however, they were visualized in different locations. Overall, Akaluc BLI complemented MPI, providing sensitive detection of distant metastases, and longitudinal measures of cell viability. This multimodal approach should improve our understanding of metastasis, and aid development of novel therapeutics.

## Keywords

Magnetic Particle Imaging (MPI), Superparamagnetic Iron Oxide (SPIO), Synomag-D, Bioluminescence Imaging (BLI), Akaluc, Akalumine-HCl, Multimodal imaging, Cancer cell tracking

## Summary for Lay Audience

The purpose of this thesis is to combine two imaging tools to help visualize cancer cells injected into mice. Magnetic particle imaging or MPI, is a new imaging system which can directly detect and quantify iron particles. Cells can be labelled with these iron particles and tracked throughout the body. However, when cells divide, the amount of iron within each cell gets diluted, and may get dispersed throughout the body. Additionally, dead cells will continue to produce a signal. For these reasons MPI cannot be used to study cell proliferation or viability. We believe that bioluminescence imaging or BLI would nicely complement MPI as it can be used to measure both proliferation and viability over long durations. One major limitation of BLI however, is that the light used in BLI gets absorbed by various tissues, reducing the signal which can be detected. This makes it very difficult to see areas deep inside the body. A solution to this is to use a reporter which produces near infrared light (NIR), as it is absorbed in lower amounts than visible light. Recently the BLI reporter Akalumine was developed, which when in contact with the enzyme Akaluc, produces NIR light. This project combines MPI with Akaluc BLI to track cancer cells injected into mice. Described in chapter 2, breast cancer cells were labelled with both iron particles and Akaluc, and then injected into mice. Following this, MPI and BLI scans were taken for 2-weeks. MPI and BLI signals were compared to determine the strengths and limitations of each, as well as to determine how they complemented each other. Chapter 3 highlights the limitations of this work, and the future directions of this project.

## Co Authorship Statement

The work contained in this thesis was conducted by Ryan J Williams, under the direct supervision of Dr. John Ronald, and Dr. Paula Foster, who aided in both study design and data interpretation. Dr. Ronald and Dr. Foster were also responsible for reviewing the writing of this thesis. Shirley Liu and Dr. John Kelly assisted with IP injections of Akalumine-HCl for *in vivo* experiments. Julia Gevaert and Olivia Sehl assisted with MPI scans and data analysis.

## Acknowledgments

First, a huge thank you goes out to my amazing supervisors Dr. John Ronald, and Dr. Paula Foster. I couldn't imagine getting through my Masters without your guidance and support. Thank you for all the late-night problem solving, the countless edits, and the weekends dedicated to helping me understand difficult concepts. Over these past two years you have pushed me to become a better researcher, and a better person. Additionally, thank you to Dr. Tim Scholl and Dr. Laura Flynn who served on my advisory committee. You were both critical in ensuring that my research progressed to the point where it's at now.

To everyone in the Ronald and Foster Labs, you have all greatly contributed to the success of this project and made coming into the lab everyday something to look forward to. Dr. Katie Parkins, you were an inspiration, and role model. Thank you for taking me under your wing when I started at Robarts. JK, Ying, Amanda, and Chen, thank you for always being there to answer a question or teach me a new technique. Olivia, you were always there for me to help troubleshoot MPI problems or give a second opinion on my data. Your positivity and feedback were greatly appreciated. Julia, we entered grad school and you were always there to lean on for both class and lab work. Shirley, you were an endless well of knowledge for BLI. I'm sure you will go on to do great things.

Finally, to my family and friends, thank you for all the support you have given me at every step of my academic journey. A special thank you goes to Alex, you always seemed to know just the right way to help me. Thank you for making the long drives to London, for the virtual study dates, and for being my best friend. I could not have finished this thesis without each and every one of you.

## Table of Contents

Abstract.....	i
Keywords.....	i
Summary for Lay Audience.....	ii
Co Authorship Statement.....	iii
Acknowledgments.....	iv
Table of Contents.....	v
List of Tables.....	viii
List of Figures.....	ix
List of Acronyms and Abbreviations.....	xiv
<b>Chapter 1</b> .....	<b>1</b>
1.1 General Introduction.....	1
1.1.1 Breast Cancer.....	1
1.1.2 Preclinical Models of Breast Cancer.....	2
1.2 Cellular Imaging.....	2
1.2.1 Probe-Based Cell Tracking (Direct Labeling).....	3
Magnetic Particle Imaging (MPI).....	9
MPI Cell Tracking.....	14
1.2.2 Reporter Gene Imaging (Indirect Labelling).....	18
Bioluminescence Imaging (BLI).....	19
Akaluc and Akalumine.....	21
1.2.3 Multimodal Optical and MPI Studies.....	26
1.3 References.....	29
<b>Chapter 2</b> .....	<b>56</b>

Abstract.....	56
2.1 Introduction.....	57
2.2 Materials and Methods.....	59
2.2.1 Cell Line Origins and Culture .....	59
2.2.2 Transduction of 4T1Br5 cells with TdTomato-Akaluc .....	59
2.2.3 Cell Characterization .....	60
2.2.4 Cell Labelling.....	60
2.2.5 Cell Viability .....	60
2.2.6 In Vitro BLI.....	61
2.2.7 General MPI Scan Setup and Protocol.....	61
2.2.8 Characterization of Synomag-D.....	63
2.2.9 In Vivo BLI and MPI .....	64
2.2.10 Image analysis .....	66
2.2.11 Statistics.....	66
2.2.12 Ex Vivo Analysis.....	67
2.3 Results.....	68
2.3.1 Transduction of 4T1Br5 cells with TdTomato-Akaluc .....	68
2.3.2 In Vitro BLI.....	70
2.3.3 Characterization of Synomag-D.....	72
2.3.4 Iron Labeling of Cells.....	72
2.3.5 In Vitro MPI .....	74
2.3.6 In Vivo Imaging of Primary Tumours.....	77
2.3.7 In Vivo Imaging of Spontaneous Metastases .....	78
2.3.8 Ex vivo Histology for transduced TdTomato-Akaluc reporter .....	82
2.3.9 Ex vivo Analysis of the MPI reporter Synomag-D .....	82

2.4 Discussion.....	85
2.5 References.....	89
<b>Chapter 3</b> .....	<b>95</b>
3.1 Chapter 2 Summary and Discussion.....	95
3.2 Challenges and Limitations of MPI.....	97
3.2.1 Contamination .....	97
3.2.2 Unwanted sources of signal.....	98
3.2.3 MPI hardware failure.....	98
3.2.4 Limitations of MPI .....	98
3.3 Challenges and Limitations of BLI.....	99
3.3.1. BLI light scattering.....	99
3.3.2 Akaluc BLI background signal.....	101
3.3.3 BLI Signal Saturation.....	101
3.3.4 Akalumine Cytotoxicity .....	101
3.3.5 Limitations of BLI.....	102
3.4 General Challenges and Limitations.....	102
3.4.1 Covid-19 Pandemic .....	102
3.4.2 Limitations of Study.....	103
3.5 Future Work .....	104
3.5.1 Short Term Work.....	104
3.5.2 Long-Term Goals .....	105
3.6 Significance and Impact.....	106
3.7 References.....	107



## List of Tables

<b>Table 2.1. Cell detection limits for Synomag-D labelled 4T1Br5-TdT-Akaluc cells.</b> A dilution of Synomag-D loaded cells ranging from 1.024 million to 500 was done. Average SNR calculated by dividing the average mean signal from 3 replicates by the standard deviation of an empty bed (0.366). SNR below 5 is undetectable based on the Rose Criterion and is not shown. Total Iron Content calculated by dividing the total MPI signal (n=3) by the slope of the calibration curve shown in Figure 2.6C (6772).....	76
--	----

## List of Figures

**Figure 1.1. Common limitations of probe-based imaging.** While highly sensitive, probe-based imaging techniques share some common limitations based on their labelling method. (A) The concentration of tracer (represented by “Fe” within red circles) in cells is diluted upon cell division, and daughter cells may receive unequal amounts of said tracer. This makes quantification of cells for proliferative populations difficult. (B) As cells die, iron remains in the vicinity, causing false positive signals. This prevents the visualization of viability. (C) This remaining iron may be engulfed by bystander cells such as macrophages. This results in signal clearance and may cause erroneous signal in distant locations. Figure made in BioRender..... 4

**Figure 1.2 Schematic of signal voids associated with T2 MRI of superparamagnetic contrast agents.** MRI of superparamagnetic iron oxide (SPIO) contrast agents, denoted as “Fe” in this image, results in a blooming artifact (grey circles). These blooming artifacts far exceed the diameter of the SPIO tracer resulting in higher sensitivity but severely reduced resolution. Figure made in BioRender..... 6

**Figure 1.3. Schematic of MPI magnetic fields.** MPI uses two electromagnets opposite one another, in inverse orientation. The magnets generate electromagnetic fields, as represented by the arrows. Where these fields cancel out in the middle, a field free region is formed (FFR), as highlighted by the red circle. Figure made in BioRender.....10

**Figure 1.4. Schematic for the Behaviour of SPIO in Magnetic Fields for MPI.** When in the presence of a magnetic field, SPIO (red arrows) will align with the field. Depending on the position of the SPIO with respect to the magnetic fields, this can result in negative saturation (i), or positive saturation (iii). When in the field free region, SPIO are randomly aligned, and have no net magnetization (ii). As the FFR passes over SPIO, their saturation will flip from negative to positive, as plotted by the Langevin function in (B). The derivative of this curve gives a point spread function (PSF) shown in cyan. This PSF is the generated signal in MPI. Figure made in BioRender..... 12

**Figure 1.5. Schematic of haemoglobin light absorbance in relation to the emission spectra of BLI reporters.** The extinction coefficient of oxygenated haemoglobin (black dashed line) is

dependent on the wavelength of light. Based on this coefficient, blue light is more readily absorbed than red light. D-luciferin oxidized by Fluc (blue line) has a peak emission wavelength of 562 nm, corresponding to green light. This restricts Fluc to imaging superficial tissue as it is readily absorbed by haemoglobin. Akalumine-HCl oxidized by Akaluc has a peak wavelength of 677 nm, falling in the red-light range. Haemoglobin has a lower extinction coefficient at this range allowing for deep tissue imaging. Haemoglobin extinction data taken from the American Chemical Society, 2010 (263). D-Luciferin and Akalumine-HCl emission spectra data taken from Kuchimaru et al., 2016 (264)..... 23

**Figure 2.1. Schematic of MPI set up.** All MPI experiments were conducted on the Momentum Scanner from Magnetic Insight seen in A. The *in vitro* set up can be seen in B. SPIO, or cell pellets labelled with SPIO were loaded into a PCR tube, and placed into an empty ELISA well. This well was taped onto the bed of the MPI. The *in vivo set up* can be seen in C. Mice were positioned in the prone position. Hind legs were extended backwards and taped to the side of the bed. An additional piece of tape was used around the abdomen to hold the mouse in place. Isoflurane was administered via nose cone by a tube running beneath the bed..... 62

**Figure 2.2. Schematic of *in vivo* MPI and BLI experimental outline.** Mice were injected with One million dual labelled 4T1Br5 cells via the 4<sup>th</sup> mammary fat pad. Mice were imaged on BLI 0-, 6-, and 13-days post cell injection, following the administration of 100 µl of 5mM Akalumine-HCl via intraperitoneal injection. Scans were done in supine position. MPI scans were conducted 1-, 8-, and 14-days post cell injection while mice were in the prone position. All scans done under 1-2% isoflurane anaesthesia. Figure made in BioRender..... 65

**Figure 2.3. Design and validation of Reporter Construct.** (A) Vector map consisting of pEF1α promoter, TdTomato and Akaluc. (B) Flow cytometry of untransduced (blue) and transduced (red) cell populations at passage 3. Cell Count vs. TdT fluorescence was plotted in a histogram. TdT positive cells within gate. (C) Confocal microscopy further confirms expression of TdT.....69

**Figure 2.4. Characterization of Transduced Cells.** Total BLI signal versus cell numbers ranging from  $6 \times 10^4$ -  $1 \times 10^6$  cells (A, B). BLI Signal scale shown in Photons per second (P/s). Unlabelled (Black), and Synomag-D labelled (Red) cells, 1 week post loading (C, D)..... 71

**Figure 2.5. Characterization of Synomag-D.** Relaxometry scans (A, B) were normalized to iron content for Synomag-D (10  $\mu\text{g}/\mu\text{l}$ ) (red), and Vivotrax (5  $\mu\text{g}/\mu\text{l}$ ) (black). Sensitivity (A), denoted by amplitude. Resolution (B) shown by FWHM. Synomag-D was 3.8x more sensitive than Vivotrax per gram of iron. 3D Calibration line (C) was made for a serial dilution of Synomag-D ranging from 50  $\mu\text{g}$  to 0.7  $\mu\text{g}$ . Calibration line later used to calculate unknown iron content from known values. Synomag-D loading of 4T1Br5-TdT-Akaluc cells was validated with Perl's Prussian stain and Nuclear Fast Red counterstain. Loading efficiency calculated by dividing number of cells with Synomag-D present by total number of cells (n=9). Viability assay conducted through Flow Cytometry for unlabelled and Synomag-D labelled cell populations. Viable cells are negative for Zombie Violet, plotted against Forward Scatter (E, F). Live cells shown in green..... 73

**Figure 2.6. Cell detection limits for Synomag-D labelled 4T1Br5-TdT-Akaluc cells.** (A) Representative MPI Images for respective cell numbers, where M" denotes million, and "k" denotes thousand. White boxes enclose "undetectable signal" (signal below SNR = 5). (B) Maximum MPI signal for low cell numbers is plotted. Thresholds of 5, and 3 times the standard deviation of the background noise (SNR 5, SNR 3) are shown in red and blue, respectfully. (C) Total MPI signal was plotted against the number of cells loaded with Synomag-D to show a positive and linear relationship. (D, E) Iron mass measured by MPI is significantly different for various cell numbers in the range of 8-64  $\times 10^3$  cells (D), and 64-1024  $\times 10^3$  cells (E).....75

**Figure 2.7. Dual Akaluc BLI and MPI for tracking transplanted Synomag-D labelled 4T1Br5 cells *in vivo*.** Representative *in vivo* BLI and MPI scans (A) are shown for days 0/1, 6/8, and 13/14 post MFP injection of labelled cells. Anatomical left and right are denoted by "L" and "R" Bright field images used to localize MPI signal in respect to BLI signal. MPI signal in Arbitrary units (A.U.) enclosed by red circles. BLI displayed as photon flux (P/s). Total MPI (B), average iron content (calculated by dividing MPI signal by the slope of the 3D calibration line) (C) and Average BLI signal (D) were all plotted with respect to days post initial injection. Individual mice are colour coded to aid trend observation. Pairwise comparisons were done for (B), (C), and (D), showing significant differences in signal over time.....78

**Figure 2.8. All secondary signals observed in MPI and Akaluc BLI *in vivo*.** (A) MPI signals, separate from the primary signal are enclosed by red circles. Scans were overlaid on a bright field image for anatomical reference. (B) Quantification of secondary signals from each mouse, with M denoting mouse, followed by a number (M1, M2, M3, M4). (C) Akaluc BLI signals separate from the primary signal. A dark covering was taped to the bottom half of each mouse to prevent signal saturation. This allowed for visualization of the secondary signals as circled in red. (D) Quantification of secondary signals from each mouse. Mouse 2 had two secondary signals (M-2a, M-2b) while mouse 4 had no secondary signals. The signal observed for mouse 4 was due to scattering.....80

**Figure 2.9. In vivo MPI and Akaluc BLI signal in distant regions.** All images are from the same representative mouse on day 13/14. The left and right of the mouse are marked by “L” and “R” The MPI scan in (A) is windowed to the full dynamic range, while (B) is the same scan set to a lower window level. This allows visualization of a secondary signal location, marked by the red circle. A histogram (C) was made by drawing a line through both the primary and secondary signal locations in (B) and plotting signal intensity relative to location. Two distinct peaks can be observed indicating that the signals are indeed separate. BLI of the primary tumour signal (D) is the same image as seen in Figure 2.7. A dark covering was taped to the bottom half of the mouse in (E) to prevent signal saturation. This allowed for visualization of the secondary metastasis as circled in red. An overlay of MPI and BLI scans (G) allows for comparison of signal location anatomically. MPI signal was flipped to align with BLI..... 81

**Figure 2.10. Ex vivo fluorescence microscopy of primary tumour and axillary lymph node.** Representative histology from one mouse, after tissue perfusion. DAPI (blue) stains all cell nuclei (A,D,G,J). Florescence in the TdTomato (red) channel, confirms expression of the transduced reporter (B, E, H, K). An overlay of DAPI and TdTomato was done to compare expression (C,F,I,L). Sections are shown at both 10 X (A-C, G-I) and 8 X (D-F, J-L) magnification. All cells of the primary tumour (A-F) were positive for TdTomato. A small fraction of cells in the lymph node were positive for TdTomato (G-L). All images taken on an ECHO Resolve microscope..... 83

**Figure 2.11. Ex vivo analysis of primary tumour for the MPI reporter Synomag-D.** 2D MPI of excised primary tumour (A), highlights that Synomag-D was present in the tumour. A representative PPB stain is displayed for one section of the primary tumour. Iron (blue) can be seen amongst the pink cancer cells, further confirming the presence of Synomag-D within the primary tumour. White arrows point to two examples of iron present in the tumour. Image of slide taken on an ECHO Resolve microscope..... 84

**Figure 3.1. BLI light scattering observed on the arm of a mouse.** One limitation of BLI is that skin and fur will scatter light giving false signal. An example of this was observed in one of the mice during the *in vivo* experiments described in chapter 2. The left arm has a signal due to the scattering of light off the extended arm, making detection of secondary lesions difficult..... 100

## List of Acronyms and Abbreviations

BLI	Bioluminescence Imaging
MPI	Magnetic Particle Imaging
CAR-T	Chimeric Antigen Receptor T Cell
NK	Natural Killer
FLI	Fluorescence Imaging
PET	Positron-Emission Tomography
SPECT	Single Photon-Emission Computed Tomography
MRI	Magnetic Resonance Imaging
$^1\text{H}$	Proton
SPIO	Super Paramagnetic Iron Oxide Particle
MPIO	Micron Sized Iron Oxide Particle
FFR	Field Free Region
CNR	Contrast to Noise Ratio
hESC	Human embryonic Stem Cells
MSC	Mesenchymal Stem Cells
EPR	Enhanced Permeability and Retention
SNR	Signal to Noise Ratio
CT	Computed Tomography
$^{19}\text{F}$	Fluorine 19

BF	Bright Field
ATP	Adenosine Triphosphate
CCD	Charged-Coupled Detector
Fluc	Firefly Luciferase
D-luc	D-Luciferin
Rluc	<i>Renilla</i> Luciferase
FDG	Fludeoxyglucose
HCl	Hydrogen Chloride
BBB	Blood Brain Barrier
NIR	Near Infrared
PDX	Patient Derived Xenografts
DMEM	Dulbecco's Modified Eagle Medium
EDTA	Ethylenediaminetetraacetic acid
pEF1 $\alpha$	Prokaryotic Translation Elongation Factor-1 Alpha-1
TdT	TdTomato
PBS	Phosphate Buffered Saline
FACS	Fluorescence-Activated Cell Sorting
PPB	Perl's Prussian Blue
ELISA	Enzyme-Linked Immunosorbent Assay
PCR	Polymerase Chain Reaction



FOV	Field of View
PSF	Point Spread Function
FWHM	Full Width Half Max
IVIS	In Vivo Imaging Systems
ROI	Region of Interest
A.U.	Arbitrary Units
ANOVA	Analysis of Variance
DAPI	4',6'-diamidino-2-phenylindol

# Chapter 1

This chapter will serve to provide all necessary background information pertinent to this thesis. Topics covered include breast cancer, probe-based cellular imaging, and reporter gene cellular imaging. Findings from relevant literature will also be discussed.

## 1.1 General Introduction

This thesis explores the development of a multimodality imaging strategy to monitor the fate of orthotopically implanted breast cancer cells in a mouse model. Specifically, we are exploring the combination of bioluminescence imaging (BLI) with a highly sensitive and relatively new BLI reporter gene called Akaluc, with magnetic particle imaging (MPI) which images iron oxide nanoparticles that can be loaded into cancer cells prior to implantation.

### 1.1.1 Breast Cancer

Breast cancer is one of the most common cancer diagnoses for women, accounting for a quarter of all new female cancer cases (1). Due in part to the high prevalence, breast cancer has proven to be one of the deadliest diseases facing Canadian women. The Canadian Cancer Society estimates that for Canadian Women, an incredible 1 in every 33 deaths can be attributed to breast cancer (2,3). This makes it the second leading cause of death for this population. The mortality rate associated with breast cancer is highly dependent on which stage the cancer is detected at. Breast cancer diagnosed in stage one or two has a 5-year survival rate of 100%, however if the cancer is not detected until stage 4, the 5-year survival rate drops to only 22% (2). This large discrepancy in survival is due to the dangers associated with breast cancer metastasis. It is estimated that at least 2/3 of breast cancer deaths are associated with cell metastasis (4). This is the process where cells migrate from a primary tumor site and form secondary lesions in disperse tissues such as bone, lung, brain, liver, and lymph nodes (5). Cancer in these locations poses a great risk to patient health, with metastatic breast cancer being generally classified as an “incurable disease” at this time (6).

While there are many variations in breast cancer treatment, depending on the staging, and the presented biomarkers, the most common approach involves surgery possibly in combination with radiation and/or drug therapies (7). Invasive surgeries are used to excise the primary tumor while systemic approaches such as radiation and drug therapies treat possible micrometastases (7). Breast cancer, however, is a heterogenous disease (8). The same treatment may not have the same efficacy in different patients. As it stands, the death rate for late-stage breast cancer patients remains staggeringly

high (2). Combining this with the invasiveness of both surgery and radiation, leaves a need for new and more effective treatment methods, better suited to treat breast cancer patients as a whole. Efforts have been made to develop new cell-based treatments such as CAR-T cell therapy (9-13), and NK cell therapy (14,15). To properly assess the efficacy of these treatments preclinical models must be implemented.

### *1.1.2 Preclinical Models of Breast Cancer*

Preclinical models have long been implemented in the field of cancer research, providing unique tools that would be otherwise inaccessible to researchers and health care professionals (16). Preclinical models for cancer can date their origin back to Clarence Cook Little's inbred mice strains in the early 1900s (17), as well as the HeLa cancer cell line taken from the cervix of Henrietta Lacks in 1951 (18). Today, there are several preclinical models which can and have been used for breast cancer research, including zebrafish (19,20), drosophila (21,22), and pigs (23,24), however, cell lines and mouse models remain the most widespread (16,25).

Preclinical animal models have seen extensive use in research, especially within the last few decades, as they provide invaluable information to the researchers using them. The use of preclinical models reduces the risk to patients while allowing researchers to alter variables that they otherwise wouldn't be able to control. Animal models for breast cancer provide insight into (i) the biological mechanisms of disease progression, including primary tumor development, molecular markers, and metastasis (26-31), (ii) the development of novel treatments and therapeutic agents (32-36), (iii) the efficacy of combined treatment regimens (37-41), (iv) the development of new diagnostic imaging modalities, tracers, and methods (42-46), and (v) the role of natural protection and the immune system in cancer prevention (47-51). To better evaluate these animals over time, it would be valuable to track cancer cells noninvasively with imaging.

## **1.2 Cellular Imaging**

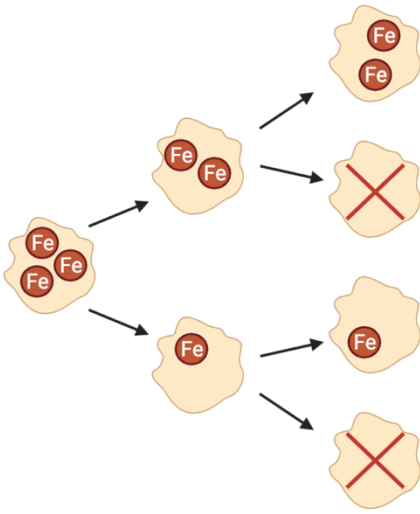
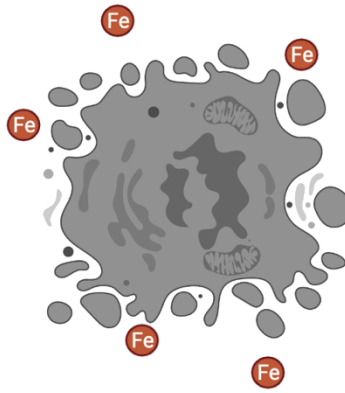
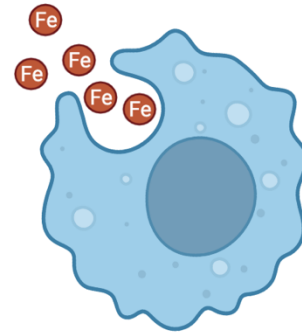
Being able to visualize, localize, and quantify cells noninvasively is critical for gaining a better understanding of cellular processes such as cancer progression and metastasis. By improving cell tracking for cancer cells, researchers hope to gain a better understanding of the underlying mechanisms of cancer, and to evaluate the effectiveness of new treatments, which may expedite their translation into the clinic. In addition, with the clinical adaptation and continued development of cellular therapies, sensitive methods for tracking therapeutic cells to better understand treatment efficacy in

real time are needed. Researchers have implemented various imaging modalities for cell tracking over the years. These include optical imaging such as fluorescence imaging (FLI) and BLI, as well as modalities highly used in the clinic such as ultrasound, positron-emission tomography (PET), single photon-emission computed tomography (SPECT), and magnetic resonance imaging (MRI). Two main strategies for tracking cells with these modalities are probe-based cell tracking through direct labelling, and reporter gene imaging, via indirect labelling (52-54). Below, we define these tracking and labelling methods, as well as highlight the strengths and limitations for each strategy. Additionally, cells can be labelled *in situ*, which while not used in this thesis, is described in section 2.3.

### 1.2.1 Probe-Based Cell Tracking (Direct Labeling)

A common way to track cells is to *ex vivo* label the cells in culture with imaging probes prior to injection into the subject of interest and imaging (55,56). Probe based imaging is a fairly simple method, as it doesn't involve genetic modifications. When comparing labelling methods for the same imaging modality, direct labelling is typically more sensitive than indirect labelling. Probe-based MRI has repeatedly shown the ability to track single cells *in vivo* (57-62), while MRI using reporter genes has consistently reported sensitivity as one of the primary limitations (63-67). It is important to note however, that some reporter gene imaging modalities, such as BLI, have shown incredible sensitivity. This will be further described in section 1.2.2.

While highly sensitive, there are a few limitations common to all probe-based imaging techniques. First, the label may be diluted, or passed asymmetrically to daughter cells during cell division. This prevents the indefinite imaging of dividing cell populations; however non-proliferative cells can be imaged over longer durations. (59-60,68,69). Additionally, the tracer may be expelled when cells die, continuing to produce an imaging signal outside the cell, which may give false positive results of where the cells are located (70). If scavenger cells, such as macrophages, engulf these, a false positive signal may also be observed in distal clearance organs (70). These limitations can be seen in Figure 1.1. below.

**Figure 1.1:****A.****B.****C.**

**Figure 1.1. Common limitations of probe-based imaging.** While highly sensitive, probe-based imaging techniques share some common limitations based on their labelling method. (A) The concentration of tracer (represented by “Fe” within red circles) in cells is diluted upon cell division, and daughter cells may receive unequal amounts of said tracer. This makes quantification of cells for proliferative populations difficult. (B) As cells die, iron remains in the vicinity, causing false positive signals. This prevents the visualization of viability. (C) This remaining iron may be engulfed by bystander cells such as macrophages. This results in signal clearance and may cause erroneous signal in distant locations. Figure made in BioRender.

## *Iron-Based Cell Tracking with MRI*

MRI has quickly established itself as one of the most popular cell tracking modalities due to its high spatial resolution and soft-tissue contrast, making it easy to discern transplanted cells from background tissue (71,72). Additionally, due to its prevalence, cell tracking methods using MRI have been refined and improved over the last few decades. Standard protocols have been thoroughly developed making MRI easy to use. The most common way MRI is used to track cells is to label them with either paramagnetic, or superparamagnetic <sup>1</sup>H-MRI contrast agents, sometimes with the help of transfection agents, as first described by Tzu-Chen et al, and Bulte & Brooks in the 90s (73,74).

Paramagnetic agents are typically composed of either Gadolinium, or Manganese (75-77). These agents shorten the longitudinal relaxation rate, T<sub>1</sub>, by increasing the relaxivity of water protons (77-79). This creates a positive contrast, which has been used previously by researchers to detect and track early lung metastasis in a mouse breast cancer model (80), as well as characterizing the early growth of prostate tumors (81). Paramagnetic contrast agents, while useful given their positive contrast, are limited by their relatively low sensitivity, limiting the number of cells that can be detected (82-84).

Superparamagnetic contrast agents, by definition, offer higher sensitivity than paramagnetic agents (82-84). These agents consist of iron oxide particles coated in a biologically inert material such as dextran or carboxydextran (Superparamagnetic iron oxide particles: SPIOs) (85,86). Iron based contrast agents are the main agents used in T<sub>2</sub>/T<sub>2</sub>\* weighted MRI sequences (87,88). Iron particles effect T<sub>2</sub>\* relaxation, causing local disturbances in the magnetic field (87,88). This results in a dark signal void, surrounding the areas where the iron is present. The large void associated with iron-based MRI is what's known as a 'blooming artifact' (89). An illustration of this can be seen in Figure 1.2. As the signal void created is large in comparison to the iron tracer, this imaging method has characteristically high sensitivity, but lower spatial resolution (90).

**Figure 1.2:**

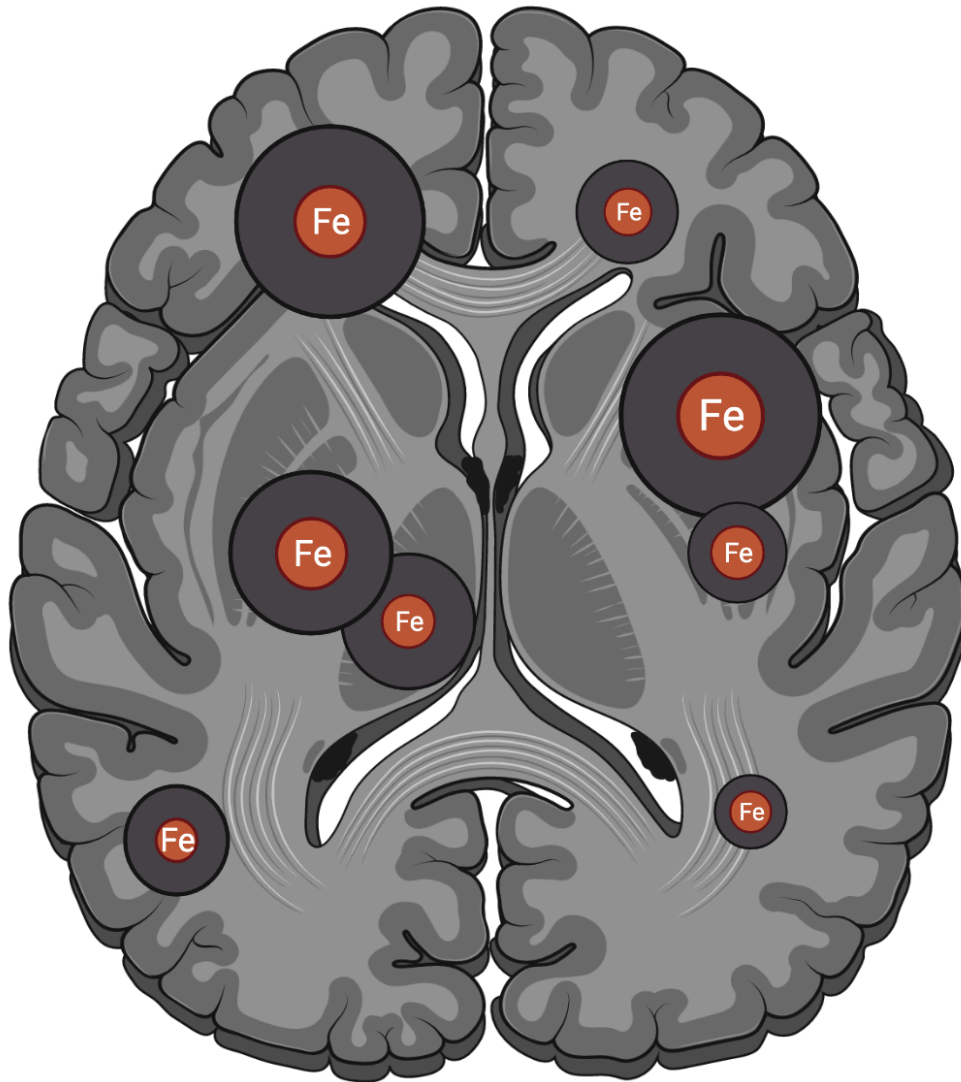


**Figure 1.2 Schematic of signal voids associated with T2 MRI of superparamagnetic contrast agents.** MRI of superparamagnetic iron oxide (SPIO) contrast agents, denoted as “Fe” in this image, results in a blooming artifact (grey circles). These blooming artifacts far exceed the diameter of the SPIO tracer resulting in higher sensitivity but severely reduced resolution. Figure made in BioRender.

There are two main strategies for labelling cells with iron oxide particles. The first method involves intravenous injection of the iron nanoparticle where it is taken up by cells within the animal model *in situ* (91,92). This method is often done to study clearance and biodistribution of a nanoparticle (93-95), to load scavenger cells such as macrophages (91,92,96-98), or in experiments reliant on the enhanced permeability and retention effect (EPR) for tracer accumulation in cancerous tissues (99-101). The second method involves loading cells with the iron tracer prior to injection. This can be accomplished by incubating the cells with the tracer, which takes up the iron through endocytosis. Iron loading can be aided by transfection agents such as protamine sulphate and heparin (102-104), as was done in this project.

SPIOs have quickly emerged as the preferred probe for cell tracking. Bulte and Kraitchman believe this preference is due to a multitude of factors including (i) having higher signal change per iron content, (ii) containing biocompatible iron which can be metabolized by the cell, and (iii) coating on their surface can be easily functionalized (105). Cells can be labelled with superparamagnetic contrast agents such as SPIOs through coincubation resulting in endocytosis. These iron containing cells can be indirectly detected with MRI via the blooming artifact (89). Various cell types have been tracked with iron-based MRI thus far including stem cells (57,106-108), immune cells (62,109-113), and most importantly for this thesis cancer cells (59,60,69,114-116).

While stem and immune cells remain popular cell types for tracking, due to their emergence in various clinical therapies, iron-based cancer cell tracking remains less common. This scarcity is driven by the difficulties imaging cancer cells over long periods (68). Cancer cells are highly proliferative, resulting in dilution of the iron tracer for each cell passage. Several groups have examined this quality *in vitro*. Foster et al., reported in 2008 that intracellular iron loaded into B16F10 proliferative melanoma cells was absent 5 days, or 6 generations post loading (60). Similarly, Econopolous et al., noticed that by day 4, over half of their iron-loaded MDA-MB-231 cells had undetectable levels of iron. By day 10, this percent dropped to only 1%. These findings indicate that signal would not be detectable using MRI, limiting MRI cell tracking to short durations for cancer cell tracking (69). This finding only holds true for proliferative cancer cell populations. Heyn et al., demonstrated that subpopulations of “non-proliferative” quiescent MDA-MB-231 breast cancer cells retained the iron oxide tracer for



upwards of a month *in vivo* (59). Similar findings were also found for SPIO labelled melanoma cells (115) and in metastatic lymph nodes (69).

One use for cancer cell tracking which has been exploited by researchers is the study of cell migration and metastasis. Econompoulos et al., were the first group to visualize cancer regions outside of the primary tumor using iron-based imaging. Iron loaded MDA-MB-231 cells, originally injected into the mammary fat pad of mice, were found on day 14 in the axillary and inguinal lymph nodes (69). Recently, researchers in our lab have applied the effects of superparamagnetic contrast agents on the T2 relaxation to visualize breast cancer metastasis to the brain of nude mice (117). Additionally, micron sized superparamagnetic iron particles (MPIO) have been used to monitor the fate of transplanted gastric cancer cells and track the migration of metastatic cells through the lymphatic system, by the Guo lab (118). Utilizing the blooming effect associated with iron based-MRI cell tracking, Heyn et al., were able to determine the fate of single breast cancer cells which had metastasized to the brain (58,59). Single cancer cells were also detected by Foster et al., and Shapiro et al., This finding demonstrates the incredible sensitivity possible with probe-based cell tracking methods such as MRI (60-62).

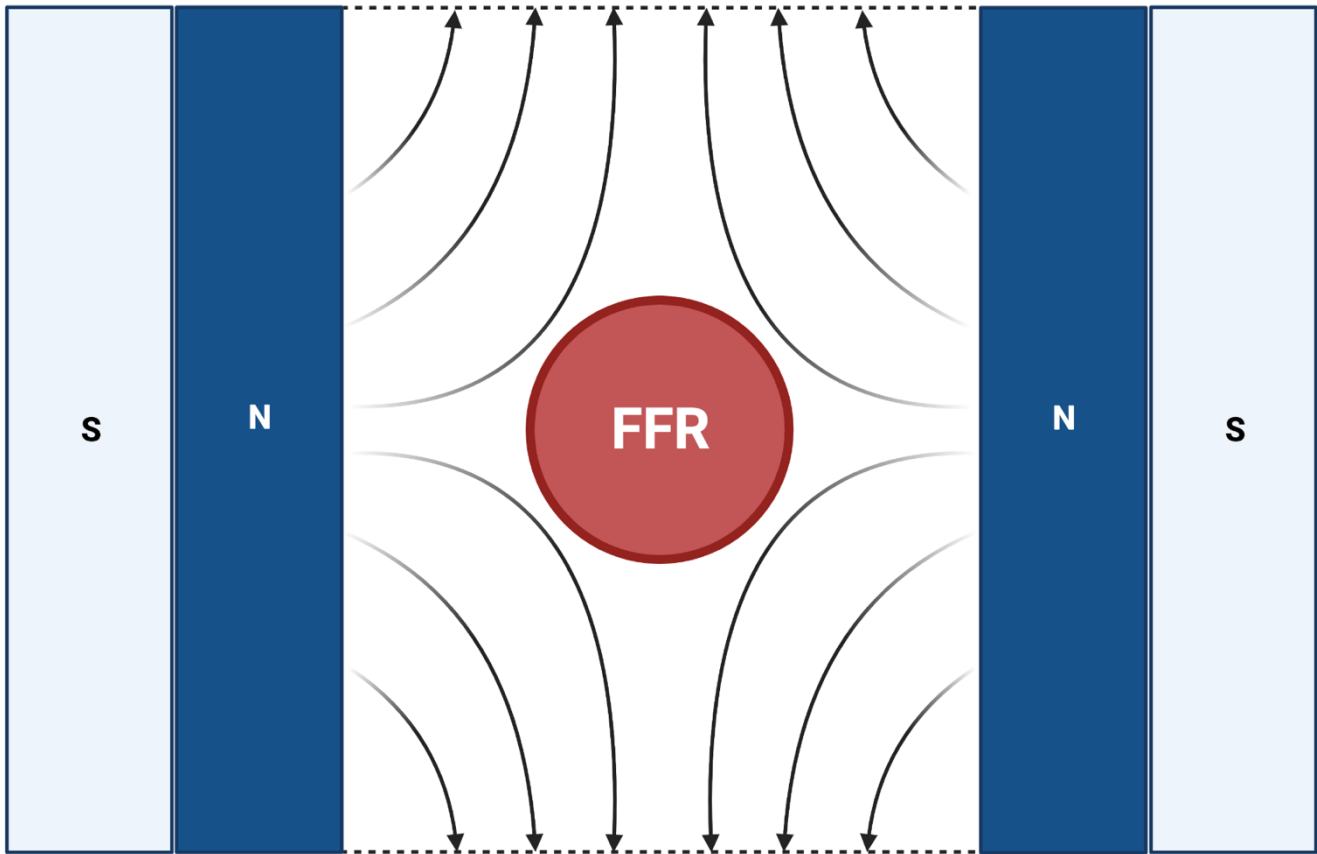
With both paramagnetic and superparamagnetic contrast agents, researchers have often questioned the deleterious effects of these particles on cell function, viability, and protein expression. Although most studies have shown little significant effect on loaded cells (119), one study published in *Neuroimage* showed Gadolinium having a non-zero effect on cellular repair mechanisms in a transplanted neural stem cells over a 1-year period (120). Other studies have linked SPIO loading to cellular stress (121-125), decreased gene expression and gene silencing (126-128), and cell proliferation (122,129,130).

While MRI using SPIO continues to be one of the most widely utilized modalities for cell tracking, major drawbacks limit the applications of this modality. Although, the SNR between dark signal voids and lighter background tissue may be high, dark regions are harder to visually discern making it suboptimal. Additionally, air filled tissues such as lungs appear black in T2 weighted MRI. As this is one of the most common locations for breast cancer metastasis (5), it makes tracking the full scope of metastasis difficult. Since these iron particles are indirectly detected, quantification of cells becomes difficult, as the signal intensity will not change linearly with iron content (86,131-133). Although efforts have been made to quantify MRI signal (134-137), cell numbers are often estimated by comparing the size of the signal void to cell number. Magnetic particle imaging (MPI) is a new modality that can help overcome some of these issues with MRI based cell tracking with SPIO agents.

## *Magnetic Particle Imaging (MPI)*

Magnetic Particle Imaging (MPI) is a novel imaging modality first conceptualized by Bernhard Gleich in 2001 (138). The concept was further expanded upon in the ground-breaking 2005 Nature paper by Gleich and Jurgen Weizenecker, a colleague with the Phillips Research team in Hamburg Germany (139). Within this paper, the first ever images were generated using the principles of MPI. These images consisted of undiluted samples of Vivotrax (which also goes by the names Resovist and Ferucarbotran), a commercially available MRI contrast agent (140). While limited to preliminary *in vitro* data, this work effectively demonstrated the feasibility of MPI as an imaging modality, welcoming researchers from around the world to improve upon the technology and its applications (139).

While the name shares striking similarities to Magnetic Resonance Imaging, MPI and MRI are not the same thing. The physics underlying MPI sets it apart from other imaging modalities, leading to its unique imaging characteristics. MPI utilizes two strong electromagnets, set up opposite one another. Similar to when bar magnets are placed in opposition, the generated magnetic field is cancelled out in the middle creating a “Field Free Region” (FFR) (42,133,139, 141-144). The schematic for this hardware setup can be seen in Figure 1.3.

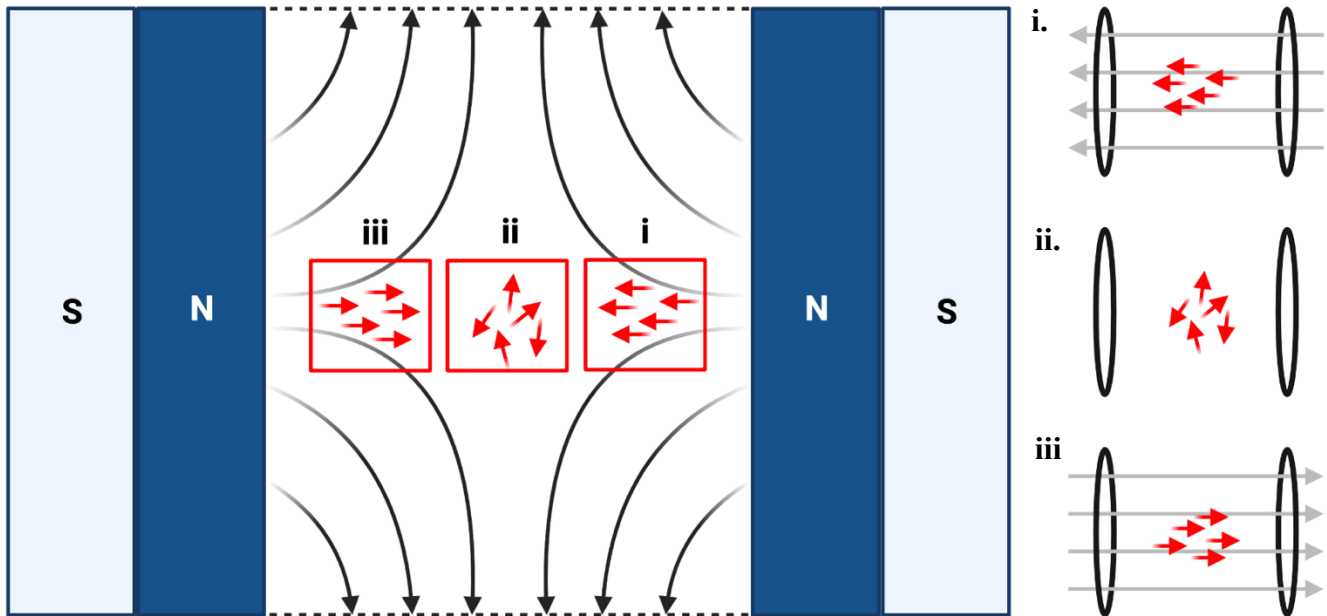
**Figure 1.3:**

**Figure 1.3. Schematic of MPI magnetic fields.** MPI uses two electromagnets opposite one another, in inverse orientation. The magnets generate electromagnetic fields, as represented by the arrows. Where these fields cancel out in the middle, a field free region is formed (FFR), as highlighted by the red circle. Figure made in BioRender.

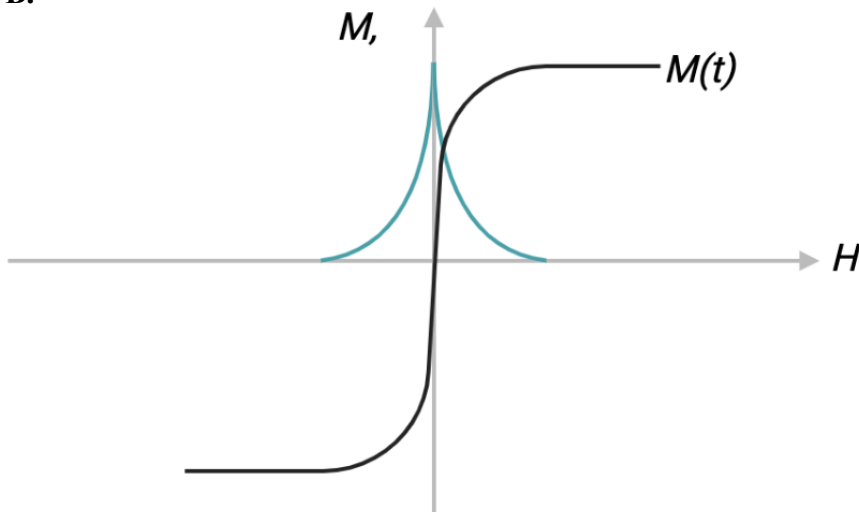
The FFR can be moved in three dimensions over the entire image view. Mechanical changes such as moving the bed in and out of the bore, and rotating the gantry are responsible for two of the dimensions. Additionally, by changing the current, the strength of each main magnet can be altered, shifting the field free region in the third dimension (145). The location of this FFR plays a critical role in generating signal from the MPI tracer. When the FFR passes over superparamagnetic iron, the magnetization of the iron flips resulting in a Voltage drop and corresponding signal. This drop in voltage in the receiver coil is turned into signal. (133,141-145). As described above in section 2.1.1, the use of SPIOs, such as Vivotrax in medical imaging is not a new development, however, MPI acts as the first system to use nanoparticles as the core tracer (146,147). SPIO were previously used as MRI contrast agents but repurposed to serve as tracers for MPI taking advantage of their unique behaviours in oscillating magnetic fields (146,147).

Figure 1.4:

A.



B.



**Figure 1.4. Schematic for the Behaviour of SPIO in Magnetic Fields for MPI.** When in the presence of a magnetic field, SPIO (red arrows) will align with the field. Depending on the position of the SPIO with respect to the magnetic fields, this can result in negative saturation (i), or positive saturation (iii). When in the field free region, SPIO are randomly aligned, and have no net magnetization (ii). As the FFR passes over SPIO, their saturation will flip from negative to positive, as plotted by the Langevin function in (B), where  $M$  is magnetization and  $H$  is the applied magnetic field. The derivative of this curve gives a point spread function (PSF) shown in cyan. This PSF is the generated signal in MPI. Figure made in BioRender.

The specific choice in SPIO has a great effect on the sensitivity and resolution of an image (148). SPIOs consist of a  $\text{Fe}_3\text{O}_4$  and/or  $\text{Fe}_2\text{O}_3$  magnetic core, coated in a biocompatible layer such as dextran. Characteristics such as the magnitude of magnetization, labelling efficiency, and relaxation rate will all influence the sensitivity of tracer detection. The relaxation rate will also, along with the particle core size, affect the spatial resolution (148). Superparamagnetic Iron has a magnetization  $10^8$  times larger than a proton with a relaxation  $10^4$  larger (149). These factors give MPI the potential to have a much higher sensitivity than standard proton MRI, however, MRI using superparamagnetic contrast agents continues to outperform MPI in terms of sensitivity due to blooming artifacts. This was described in the “Iron-Based Cell Tracking with MRI” section. Additionally, as all iron naturally found in the body is paramagnetic rather than the superparamagnetic iron needed for MPI, tissues will give no signal in MPI, giving MPI an inherently high CNR (42,133,141-144).

During the early stages of MPI use, researchers relied on SPIO such as Vivotrax (150) or Feridex (151) which were common MRI contrast agents. While these particles did generate images in MPI, they were not designed specifically for MPI and thus the sensitivity and resolution suffered. Over the decade and a half since MPI was first created, companies such as Micromod Partikeltechnologie GMBH (Synomag-D) have developed MPI tailored nanoparticles (152,153). This was done by altering the composition, size, and shape of the magnetic core to optimize their detectability with MPI (152). Synomag-D was used in this thesis and its characteristics for cell tracking are outlined below. Synomag-D was developed and characterized by researchers at the University of Wuzburg, Germany, and Micromod Partikeltechnologie GmbH (152). In comparison to Vivotrax, the SNR of Synomag-D was 4x as high, when normalizing to iron content. Additionally, the full width half max of the generated point spread function was slightly narrower for Synomag-D than Vivotrax, indicating superior resolution, although the exact measurements were not given (153). It has been demonstrated that Synomag-D could be used to efficiently label erythrocytes (154), dendritic cells (155), and cancer cells (156). When developing nanoparticles for the purposes of cell tracking it is important to determine biodistribution and clearance of the particle (157). IV injections of Synomag-D and Vivotrax revealed that both tracers accumulate in the liver and spleen over the first 24 hours of injection. The blood half-life of 0.62 hours for Synomag-D was slightly longer than the 0.59 hours

observed for Vivotrax (158) This results in less signal clearance over time. While promising Synomag-D has not been fully explored yet for cell tracking.

Incubation of cells with SPIO can result in their uptake by natural processes such as endocytosis, or uptake can be aided by the use of transfection agents (103). Injection of these cells into animal models allows for *in vivo* cell tracking. As the SPIO within cells is detected directly, the number of cells in an area can be quantified by relating the intensity of the signal to the amount of iron loaded into the cells (42,133,141-144). This characteristic can only be accurately applied to short-term tracking of dividing cell populations as the tracer is diluted upon cell division (58-60, 68,69).

MPI has incredible promise for cell tracking due to the unique characteristics associated with it, including its high specificity, positive contrast, and ease of quantification. However, relatively low sensitivity and resolution compared to other more established imaging systems has been a limiting factor in the application of MPI for *in vivo* applications. Over the last few years, advancements in MPI hardware, and tracer technology have greatly improved both sensitivity and resolution of this modality. Sensitivity for MPI is defined as the lowest cell number (cellular sensitivity), or volume of iron (tracer sensitivity), required to produce a detectable signal. Song et al., in 2018 were able to detect as few as 250 cells (7.5 ng of iron; 30 pg iron/cell) *in vivo* using a custom MPI tailored SPIO (159), while Zheng et al., estimated that they could detect 200 cells based off the SNR of an image of a 1000 cell (5.36 ng of iron;  $26.8 \pm 0.3$  pg/cell) sample (157).

The highest reported resolution over a three-dimensional area for MPI is around 1mm using a commercially available SPIO (143,148,153), and 200  $\mu\text{m}$  using MPI optimized nanoparticles (160). Pushing the limits of MPI even further, the Rinaldi and Conolly groups demonstrated in 2021 the capabilities of superferromagnetic nanoparticle chains as an MPI tracer. This new development resulted in sensitivities 40-fold greater than SPIO, with a 10-fold increase in resolution, although exact resolution and sensitivity limits were not calculated (161). These improved qualities make MPI an excellent modality for fields such as vascular perfusion (143,162,163), inflammation (164,165), and most importantly for this thesis cell tracking (133,146)

### ***MPI Cell Tracking***

Compared to cell tracking with MRI, MPI cell tracking remains an underdeveloped field. Limited cell types having been tracked *in vivo*, and few papers have quantified iron content, or the corresponding cell numbers (166). Stem cells remain the most widely used cell type for MPI cell

tracking (132,142,164,167-169), however other cell types including pancreatic islets (170,171), T cells (172), tumor-associated macrophages (173), neural progenitor cells (157), dendritic cells (155), patient derived xenografts (174) and breast cancer cells (42,175,176) have been tracked *in vivo*.

Human embryonic stem cells (hESC) provided a relatively simple model for the earliest of cell tracking experiments. Tracking stem cells have high relevance for clinical therapeutics. Additionally, the relatively low levels of proliferation make tracking with MPI easier. In 2013, Saritas et al., were the first to demonstrate the ability of MPI to track hESC in a subcutaneous model using the MRI contrast agent Vivotrax. This paper established that MPI could detect iron oxide loaded cells with high contrast, no depth attenuation, and no background mouse signal. Additionally, this was the first paper to show the linearly quantitative nature of MPI. Injection sites containing  $2 \times 10^5$  cells, showed double the amount of signal as injection sites containing  $1 \times 10^5$  cells when quantified (141).

While the ability to detect locally administered cells has its uses, such as for stem cell engraftment, or primary tumor growth, it is important to evaluate MPI's ability to track cells systemically. This will provide a useful framework for applications such as cancer metastasis and therapeutics. A common method for stem cell therapy is the intravenous injection of MSCs, however an imaging method for this treatment is underdeveloped. Motivated by this, Zheng et al., in 2016 provided the first application for tracking the biodistribution, engraftment, and clearance of systemically administered cells with MPI. MSC were labelled *in vivo* and injected intravenously into healthy rats. Cells were immediately observed in the lungs, supporting earlier findings that systemically administered MSC could become trapped in the lungs of patients. Within 24 hours, cells the majority of signal shifted to the liver and spleen indicating clearance. Clearance continued over the 12 days post injection, with a blood half-life of 4.6 days. *Ex vivo* histology and plasma spectrometry confirmed the anatomical localization of the SPIO tracer. This was the first experiment to show the clearance pattern of SPIO labelled cells. This is important when considering background signal in an image and whether it is a result of clearance (167). Zheng et al., also demonstrated in a 2015 paper that Vivotrax labelled neural progenitor cells could be implanted directly into the brain of mice and imaged for up to 87 days. This was accompanied by ventricular clearance (157).



Another example of tracking cells systemically with Vivotrax came from Makela et al., in 2020. This group successfully labelled tumour associated macrophages via intravenous injection of Vivotrax. MPI was able to detect signal in the lungs of mice, a feat not accomplished by MRI (173). This could only be done *ex vivo*, however, due to gastrointestinal signal.

The majority of early MPI papers have used Vivotrax as their tracer, however, later studies have shown significant limitations in using these repurposed nanoparticles. Vivotrax has a bimodal distribution of iron cores. Only 30% of the core particles are the right size for MPI (24 nm), with the remaining 70% being only 5 nm. This means that only a small fraction of the iron within Vivotrax contributes to the MPI signal (177). Bulte et al., in 2015 were the first group to use MPI tailored nanoparticles for stem cell tracking. This research was motivated by the loss of availability of two commonly used SPIO in Vivotrax and Feridex, which spurred the development and characterization of new nanoparticles. An MPI tailored nanoparticle, denoted “UW”, was compared against both Vivotrax and Feridex for tracking of stem cells labelled *in vivo*. The new particle, specifically designed with MPI in mind, had a monomodal distribution of cores (19 nm), compared to the bimodal distribution of Vivotrax. This allowed for a larger fraction of the iron to contribute to the MPI signal. However, Ferguson et al., have shown that MPI signal will increase with magnetic core size from 14 to 27 nm for monodispersed iron particles, meaning this particle could be optimized further. Nonetheless, the UW had a slightly higher MPI signal per unit of iron than Vivotrax, allowing for detection of  $5 \times 10^4$  cells. Bulte et al., also showed that there was a strong relationship between the MRI and MPI signal locations. This helped cement the idea that MPI could be used to accurately track cells *in vivo* (132).

Since 2015, several new nanoparticles have been developed with MPI in mind. These include LS-008 from Lodespin Labs LLC , Janus nanoparticles from the Rao lab at Stanford, and Synomag-D from Micromod. As mentioned before, Vivotrax has a bimodal distribution of core sizes, with only a small fraction being of an optimal size for MPI. In contrast, these MPI tailored nanoparticles have cores of uniform size, all of which are in the optimal size range for MPI. This results in superior signal output per iron and sensitivity compared to Vivotrax. Yu et al., intravenously administered LS-008 where it was taken up by subcutaneously implanted breast cancer cells *in situ*, in part due to the EPR effect. This was the first paper to image cancer cells with MPI using systemically administered nanoparticles. (42).

The Rao Lab at Stanford., were another earlier group to utilize MPI for cancer cell tracking using MPI tailored nanoparticles. HeLa cells were labelled with Janus SPIO developed in house and imaged on

MPI, MRI, and fluorescence imaging. They found that MPI could detect as few as 250 cells, with superior SNR to that of MRI and fluorescent imaging (32). Additionally, this group was able to detect cancer cells 20 days post injection, with only a 20% reduction in signal. This indicates the potential for long term tracking of some cancer cells (32).

Additionally, Makela et al., demonstrated that cancer cells could be tracked with MPI following labelling with micron sized paramagnetic iron oxide particles (MPIO) (Bang's Beads) (176). While not specifically tailored for MPI, MPIO do offer some unique advantages over standard MRI contrast agents. MPIO are far larger than nanoparticles which means that cells labelled with these particles typically contain around 3-fold more iron than those labelled with SPIO, increasing the signal output and sensitivity (178) The use of MPIO MPI offered high specificity and quantification in cancer cell imaging which was combined with BLI and CT to longitudinally monitor cancer cell implantation, tumor growth, and metastasis (176). The multimodal approach to this research will be expanded upon in section 2.3.

A focus in our lab over the last few years has been the tracking of various cell types *in vivo* using MPI. Sehl et al., were the first group to combine MPI with  $^1\text{H}$  MRI and  $^{19}\text{F}$  MRI for cell tracking. Feraheme (Feramoxytol) labelled MSC implanted into the hindlimb of mice were tracked with MPI and  $^1\text{H}$  MRI while Macrophages labelled intravenously with perfluorocarbon were tracked with  $^{19}\text{F}$  MRI. This unique multimodal approach allowed for quantitative monitoring two distinct cell populations. MSC delivery, and number over time was tracked with MPI, while inflammation could be quantified with  $^{19}\text{F}$  MRI. This highlights one benefit of multimodal imaging with MPI. A reoccurring limitation of MPI was brought up in this paper, however. An undesired gut signal was observed in all mice imaged caused by iron in the mouse feed. This can cause problems when trying to image signal close to the gut region (Sehl et al., 2019). In a follow up paper by Sehl and Foster, the *in vitro* sensitivity for MPI and  $^{19}\text{F}$  MRI were compared for both MSC populations They found that MPI had the potential to be more sensitive than  $^{19}\text{F}$  MRI for cell detection. MPI was able to detect 4000 Vivotrax labeled MSC cells (76 ng iron) compared to the 256000-cell limit ( $9.01 \times 10^{16}$   $^{19}\text{F}$  atoms) found for  $^{19}\text{F}$  MRI. The implementation of longer scan times allowed for detection limits of 2000 MSC (38 ng of iron), and 4000 4T1 breast cancer cells (37 ng of iron) *in vitro* (175).

In 2020, Parkins et al., demonstrated for the first time the ability to track systemically administered circulating tumor cells (labelled with the MPIO Bang's Flash Red) homing to mammary fat pad tumors. Iron content in the primary tumor ( $0.789 \pm 0.184\mu\text{g}$ ), and contralateral mammary fat pad ( $0.318 \pm 0.044\mu\text{g}$ ) could be quantified with MPI; an important step in developing this clinically relevant model for cancer therapeutics (179). Later in 2020, Melo et al., tracked, and quantified metastatic cancer cells with MPI. This research successfully detected as few as  $5 \times 10^4$  MPIO labelled breast cancer cells in the brain of mice. The linear relationship of MPI signal to iron content in MPI allowed for quantification which was not possible with MRI (180). In 2021 Gevaert et al., for the first time tracked Synomag-D labelled dendritic cells implanted in the footpad of mice with a sensitivity of approximately 4000 cells. It is estimated that only a small fraction of dendritic cells (10%) reaches their desired destination, prompting the need for a sensitive and quantitative imaging modality. MPI was used in this study as it overcomes the sensitivity issue of  $^{19}\text{F}$  MRI, and the quantification difficulties of  $^1\text{H}$  MRI. Additionally, this paper demonstrated a technique for minimizing gut signal which was modified for this thesis. Mice were fasted for 12 hours prior to imaging and given laxatives. Bedding was replaced with a corn based alternative. This successfully reduced gastrointestinal signal to a point where it was not visible in the dynamic range of tumor signal (155). Knier et al., were the first group to successfully label patient derived metastatic breast cancer cells with Synomag-D and detect them in the brains of mice *in vivo* (174). This paper will be expanded upon in section 2.3.

While MPI is an exciting new modality for cell tracking, it is not without its flaws, however. Firstly, as mentioned before, researchers have observed a characteristic background gut signal as a result of the clearance pathway, and contaminations in food and bedding. Secondly, no anatomical information is given for MPI, requiring the co-registration of CT or a bright field (BF) photograph. Additionally, spatial resolution is currently low for MPI, making it difficult to differentiate between closely situated regions. Finally, MPI signal will decrease over time due to cell proliferation, cell dispersion, and clearance preventing the indefinite tracking of dividing cell populations, as outlined in section 2.1.1. To minimize the impact these limitations, have for cell tracking, as well as to add new unique advantages, our lab has turned towards combing MPI with optical imaging modalities such as BLI.

### ***1.2.2 Reporter Gene Imaging (Indirect Labelling)***

The second category of cell labelling is reporter gene imaging, what has also been called indirect labelling (52,181,182). This is a more complicated technique as it involves genetic modification of a cell's genome. This method takes advantage of the host cell machinery to produce a reporter protein,

such as a luciferase or fluorescence protein (52,181,182). As the label is genetically encoded, each daughter cell will receive their own copy of the reporter gene upon cell division. This allows for long term tracking of proliferation and cell migration. Additionally, most protein reporters are quickly denatured upon cell death, allowing for tracking viability as no exogenous signal is produced (52,181,182). Due to these reasons, reporter gene imaging can be used to track cells indefinitely.

Due to the required genetic modification, researchers using indirect labelling run the risk of altering cell phenotype and causing unforeseen genetic effects (183-185). Expression of transduced proteins may be regulated, and silencing may halt expression (183-185). For these reasons, it is harder to translate indirect labelling to a clinical setting compared to direct labeling, but recent successes of reporter gene imaging in patients have paved the path to using this technique in more studies interested in tracking cell-based therapies and other applications (186-189).

### *Bioluminescence Imaging (BLI)*

Bioluminescence imaging (BLI) is an optical imaging modality that takes advantage of the natural process of bioluminescence to locate cells in preclinical models (190-193). If you have ever seen a firefly light up the sky, or pictures of angler fish luring in prey, you are familiar with bioluminescence. This is a natural phenomenon exhibited by roughly 75% of marine animals (194,195) as well as many terrestrial insects (196) as a method to attract mates, mark territory, communicate, or lure prey (196-199). Different animals produce light at different wavelengths, resulting in a full spectrum of colours (200).

Fascinated by this process, scientists have isolated many of the genes responsible for bioluminescence and transduced them as reporter genes for imaging. Over time, modifications have been made to existing bioluminescence reporter genes or their substrates to increase signal intensity or change the resulting wavelength of the emitted light (201-203). Luciferases are a generic term for an enzyme capable of catalyzing the oxidation of luciferin protein to an oxyluciferin. This is often done in the presence of ATP and oxygen; however, this is not required for all luciferases. This reaction, known as the bioluminescence reaction, produces light as a by-product. The produced light is what gives signal in BLI. BLI is based on the transduction of a luciferase reporter gene into your cells of interest. After this, cells can transcribe and translate the luciferase gene into protein using their own host machinery.

The produced light is detected by a cooled charged-coupled detector (CCD) camera that is in attached to a light-tight box that the animal is placed in. CCD cameras are devices capable of converting light into electrical potential. This produces the spatially localized signal and the resultant images in BLI (190-193).

The first, and by far most common luciferase used for BLI is firefly luciferase (Fluc) and its substrate D-Luciferin (D-luc). First cloned in 1985 (204) from the North American Firefly (*Photinus pyralis*) and used as a reporter for assays three years later (205). Since then, a variety of luciferases have become commercially available including those from sea pansy (*Renilla*; Rluc) (206-208), click beetle (*Pyrophorus plagiophthalmus*) (209-211), jellyfish (*Aequorea*; Aequorin) (212-214), and several bacterial species (*Vibrio fischeri*, *Vibrio harveyi*) (213-217). Each luciferase/luciferin pair offers unique characteristics, including the colour produced, the cofactors required, and the sensitivity of imaging (190,200)

Unlike with fluorescence imaging, there is little endogenous BLI signal in mice and thus BLI offers high specificity for visualization of cells models (190-193). Due to this, BLI has seen heavy use for tracking stem cell (218,219) and immune cell therapies (220,221) *in vivo*. Tracking stem cells is an important step in determining the efficacy of stem cell therapy for conditions such as cardiac (222,223) and brain injuries (224,225). BLI allows for visualization of stem cell migration, proliferation, and implantation (218,219,223). BLI makes it easier to determine that systematically injected stem cells are localizing to the area of interest and proliferating to fill their need (218,219). Additionally, BLI has been used to track various immune cells including T cells (227,228), Natural Killer cells (229-31), and dendritic cells (232,233). Immune cell development, migration to infection sites, and interactions with other immune cells can all effectively be studied with BLI (220,221). Tracking immune cells can go a long way in helping understand disease states, developing and optimizing therapeutics, and guiding cancer immunotherapy.

In addition to tracking stem cells and immune cells, BLI excels at tracking cancer cells, due to its unique ability to track cancer proliferation sensitively and specifically over long durations; a hallmark of cancer (234-236). BLI has been used extensively in literature to track cancer progression, examining cancer metabolism (237-242), apoptosis (243-245), tumor hypoxia (246-248), angiogenesis (249,250), and most importantly for the purposes of this thesis, tumorigenesis, and metastasis (251-255).

The growth and proliferation of cancer cells is something often studied using BLI in preference over other imaging modalities, where cells can be detected in as little as a few minutes post injection and

will show a logarithmic increase over the lifetime of the cell line (190,251). BLI has characteristically high sensitivity, especially for superficial regions. Sensitivity in BLI is the minimum number of cells required to produce a detectable number of photons at a specific depth. BLI allows for single cell detection (256), although the sensitivity of standard BLI drops drastically with depth (190-193). The high sensitivity of BLI for superficial regions has been used for detecting small tumor lesions and the early stages of cancer metastasis (257-259). This quality was expanded upon by Momcilovic and Shackelford in 2018, who showed that BLI could detect superficial tumours at earlier stages than MRI, CT, and PET, due to the ability to detect fewer cell numbers (242). Although in a different study conducted by Puaux et al., in 2011 showed PET had a 22% higher sensitivity than BLI when detecting deeper gastric cancer cell lesions. This was explained by the light attenuation and scattering observed at depth in BLI. Puaux et al., found that BLI was best for detecting well defined superficial tumors. BLI as with FLI proved to be the two most practical techniques for measuring tumor burden. Both BLI and FDG-PET could identify nonpalatable tumors in mice, a feat not accomplished by MRI or FLI (260).

### *Akaluc and Akalumine*

A significant limitation of BLI is that light is attenuated by biological tissue. As light travels through an animal, a significant portion of the energy is absorbed or scattered by the surrounding tissue. This greatly reduces the possible signal as well as introduces depth effects (190-193,234). Signal generated from deeply situated tissues such as the brain will show a lower signal compared to superficial signal due to the increased attenuation, resulting in low three-dimensional resolution. The sensitivity of BLI is greatly dependent on the depth of imaging (190-193, 234). 3D BLI exists to counteract some of these depth issues, but its use is not that widespread right now as it takes more time to image one mouse and thus is not as high throughput as 2D BLI (261).

The improvement of matched BLI reporters and their substrates is the focus of many academic and industrial scientists. Numerous Luciferin, and Luciferase analogues have been developed in recent years to improve one or more aspects of BLI. To combat the depth effects prevalent in BLI, researchers have turned towards luciferin analogues which produce light in the far red, or near infrared range ( $\lambda_{\text{max}}$  of 650-900nm) (262). Red shifted light, especially light with wavelengths in the near

infrared range, have lower attenuation in biological tissue. Hemoglobin, myoglobin, and melanin all have a lower excitation coefficient (absorption coefficient) for light in the near infrared range (263). This can be visualized in Figure 1.5, using Akalumine-HCl as an example (264).

Figure 1.5:

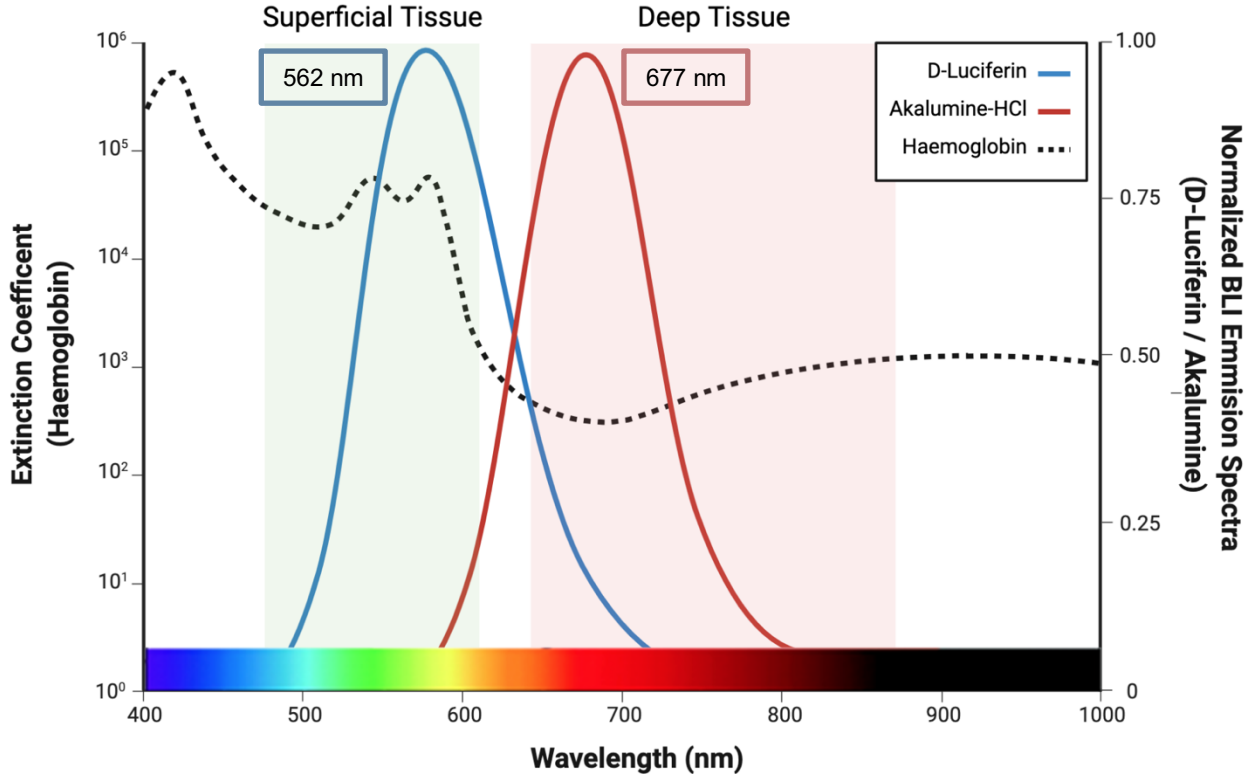


**Figure 1.5. Schematic of haemoglobin light absorbance in relation to the emission spectra of BLI reporters.** The extinction coefficient of oxygenated haemoglobin (black dashed line) is dependent on the wavelength of light. Based on this coefficient, blue light is more readily absorbed than red light. D-luciferin oxidized by Fluc (blue line) has a peak emission wavelength of 562 nm, corresponding to green light. This restricts Fluc to imaging superficial tissue as it is readily absorbed by haemoglobin. Akalumine-HCl oxidized by Akaluc has a peak wavelength of 677 nm, falling in the red-light range. Haemoglobin has a lower extinction coefficient at this range allowing for deep tissue imaging. Haemoglobin extinction data taken from the American Chemical Society, 2010 (263). D-Luciferin and Akalumine-HCl emission spectra data taken from Kuchimaru et al., 2016 (264).



Having a lower absorption coefficient means less light is absorbed or scattered by the biological tissue (265,266). This results in a few key advantages when looking at BLI signal. Firstly, signal produced in deeply situated tissues can now be detected by the CCD camera. This is especially important when studying tumours or metastases located in deeper tissues such as bone marrow, and the brain; two of the more difficult organs to image with BLI. Being able to generate signal from these locations leads to a more complete picture of where metastases are located, and how they are progressing. Additionally, as less signal is attenuated, BLI reporters that utilize near infrared wavelengths will have a higher sensitivity to lower cell numbers than those with shorter wavelengths. Fewer cell numbers can be accurately detected, which can be beneficial when looking at the early stages of tumor formation (262).

Several luciferin analogues that produce red shifted light have been developed, including the naphthyl-luciferin NH<sub>2</sub>-NpLH<sub>2</sub> (201,267), seMpai (268,269), Furizamine (Nanoluc & Antares substrate) (270-272), and Akalumine (273,274) among others. Akalumine in particular has shown single cell sensitivity at depth *in vivo*, making it a promising option for cell tracking. In 2016, Japanese researchers led by Takahiro Kuchimaru and Satoshi Iwano synthesized the NIR luciferin Akalumine-HCl from the common D-luciferin substrate. D-luciferin was converted into Akalumine by replacing the aromatic structure to that of a benzothiazole moiety. This change resulted in a maximum emission wavelength of 675nm, which is red-shifted from the maximum emission wavelength of 562nm observed in D-Luciferin (264,273). While this new product showed a markable improvement from D-Luciferin, Akalumine showed poor water solubility due to the hydrophobicity. This results in poor *in vivo* application. To address this concern, Kuchimaru et al., made the water soluble derivative Akalumine-HCl which emitted light at 677 nm (274).

Kuchimaru and Iwano went on to test their new BLI reporter system against the standard pair of D-Luciferin and FLuc (FLuc BLI). In a tissue phantom, Akalumine-HCl had 8.3 times higher depth penetration than D-Luciferin at a depth of 8mm, indicating the potential for imaging deeply situated tissues. The *in vivo* BLI performance was tested using two deep tissue *in vivo* models: lung cancer and brain striatum of mice. Akaluc BLI produced signal 52 times greater than FLuc BLI when detecting small metastases in the lungs of mice. This is significant as lungs are one of the most common sites of metastases, and the early detection of these could greatly improve therapeutics. Further, cells injected into the striatum of living mice produced signal an incredible 1408-fold greater for Akaluc BLI than FLuc BLI (274). This can be attributed to (i) D-Luciferin does not readily cross the blood brain barrier as described by Mofford & Miller (275) while Akalumine-HCl crosses in much higher concentrations (274) (ii) Akaluc has a catalytic activity 7-13 times that of FLuc. (iii) The brain is one of the deepest

situated organs, resulting in more attenuation for Fluc BLI compared to Akaluc BLI. To further demonstrate the incredible sensitivity Akaluc BLI offered, Kuchimaru and Iwano went on to detect single cells implanted 4.8mm deep in the brains of marmosets (274). Until this point, BLI was limited to small animal imaging.

Since the development of Akaluc BLI by Kuchimaru and Iwano, several groups have utilized this system to track various cell types *in vivo*. In a 2020 paper, Su et al., tracked the migration of CAR-T cells for osteosarcoma treatment (276). As reported by Iwano et al, Akaluc BLI offers 13-fold greater signal output per reporter molecule for intrapulmonary locations (274). This increased signal allowed Su et al., to detect cells in the deeply situated lung tissues (276). Liu et al. used this system to track metastasizing breast cancer cells in a novel model of synchronous bilateral breast cancer (277). The sensitivity of Akaluc allowed for visualization of metastases in the lungs of mice 13 days sooner than when using a different high sensitivity BLI reporter Antares2. Researchers from the University of Tokyo tracked the engraftment of MDS-L cells (for the hematological malignancy Myelodysplastic syndrome) in the brain of mice using a xenograft model. The brain is historically a very difficult region to image with BLI due to its depth, shielding by the skull, and the inability for substrates to cross the blood brain barrier (BBB), however the high sensitivity of Akaluc BLI and the increased tissue permanence of Akalumine-Hcl compared to D-luciferin (264) allows for visualization of brain cells. (278). Bozec et al., successfully tracked patient derived glioma stem cells transplanted intracranially in mice. In a comparison to Fluc BLI, Akaluc BLI produced a 100-fold greater signal *in vivo* allowing for detection of as few as 5000 deeply situated brain glioma cells (279).

While the literature regarding Akaluc BLI's use in tracking cancer cells over long durations is sparse, the papers presented by Iwano et al., Kuchimaru et al., Su et al., Liu et al., Zhong et al., and Bozec et al., highlight the potential for BLI with the Akaluc and Akalumine. Akaluc BLI promises higher sensitivity tracking of cancer cells due to the increased production of light using Akalumine-HCL, as well as the decreased light attenuation. Akaluc BLI allows for tracking early stages of metastases in previously inaccessible organs such as the lungs and brain, giving a more complete picture of metastasis, as well as treatment outcomes (264,274,276-279).

Although the implementation of NIR, Akaluc BLI overcomes many of the limitations prevalent in standard FLuc BLI, it is still not a perfect system. Francesco Amadeo et al., noted that Akalumine-HCl saturates Akaluc at a far lower concentration than observed in FLuc BLI. For substrate concentrations far exceeding the standard dose, this may result in FLuc BLI actually having a higher sensitivity than Akaluc BLI when substrates are administered subcutaneously (280). Additionally, a background liver signal has been reported by multiple groups after intraperitoneal of Akalumine-HCL, without the presence of Akaluc (268,276,280). Multiple papers have also noted that in comparison to other BLI reporters, Akalumine-HCl was more acidic, resulting in increased cytotoxicity (268,281). Lesions may also form surrounding the injection site (280). Further, the stronger signal produced by Akaluc BLI may actually hinder the examination of secondary signal locations. If the signal originating from the primary tumor is too large, it will saturate the CCD camera, preventing visualization of regions with low cell numbers such as metastases. A common practice to minimize camera saturation in BLI is to cover the primary signal location with a dark opaque shield. While useful, this technique may also block secondary regions close to the primary tumor. Lastly, BLI is still limited by substrate availability and genetic modification, reducing its potential for clinical translation. To date, Akaluc BLI has not been combined with a medical imaging system for multimodal cell tracking, the application of which should minimize the limitations of this modality.

### *1.2.3 Multimodal Optical and MPI Studies*

No imaging modality is perfect and is associated with its own limitations. For the best results when tracking any cell type, it may be beneficial to combine multiple modalities together, combining the strengths of each modality while minimizing their unwanted limitations. MPI relies on directly loading cells with a SPIO and can provide excellent cell detectability but can be limited to short-term tracking of highly proliferative cancer cells due to dilution of label over time. Combining MPI with an optical imaging modality such as BLI can allow for highly sensitive short-term tracking with MPI and longer-term tracking of viable cancer cells with BLI.

Several groups have combined MPI and optical imaging together. In 2017, Yu et al., became the first group to image tumors with MPI after systemic injection of nanoparticles. BLI was used on day 1 of this proof-of-concept study to confirm the MPI findings. High concordance was found between MPI and BLI signals at this early time-point (42). Using optical imaging as a positive control for signal location is a common practice for MRI. Another application for multimodal imaging is the industrial development of functionalized tracers. In 2015, Arami et al., systemically administered MPI tailored

nanoparticles with fluorescent moieties, and tracked their biodistribution and clearance with MPI and fluorescent imaging (282). This was followed by their 2017 paper which detected brain cancer cells labelled with PET and FLI functionalized MPI nanoparticles in both xenograft and murine models (283). In 2019, Song et al., developed their own multimodal nanoparticles capable of producing contrast in MPI, MRI, photoacoustic imaging, and fluorescent imaging. This nanoparticle was used to track brain and breast xenografts in both subcutaneous and orthotopic models with both optical and medical imaging systems. Additionally, the biodistribution and clearance was assessed with MPI over an 85-day period, marking one of the longest MPI experiments to date (284).

Jung et al., in 2018, developed a novel theragnostic technique for treating and imaging the hypoxic region of tumors. Exosomes, isolated from human MDA-MB-231 breast cancer cells were modified to carry the therapeutic Olaparib, along with Vivotrax, and a probe based fluorescent agent in DiO. The uptake of these exosomes by tumors, and the simultaneous treatment, was imaged using MPI and fluorescence microscopy, marking the first time MPI has been used to track exosome biodistribution. The use of fluorescence probe allowed for visualization and quantification using fluorescence microscopy, and a measure of exosome uptake, and apoptosis using flow cytometry (285).

The papers highlighted so far have either used functionalized nanoparticles (42,282-284), or fluorescent probes (285). While these methods have their advantages, such as the ability to add targeting moieties, and ensuring that MPI and optical imaging signals are originating from the exact same location, they are also inherently limited in their application. By utilizing fluorescent moieties or probes rather than transduced reporter gene constructs, optical imaging is subject to the same limitations of probe-based imaging described in section 1.2.1. and cannot be used to track viability and proliferation in dividing populations indefinitely.

Few researchers have combined MPI with reporter gene-based optical imaging for long term tracking of cells. The use of reporter genes rather than fluorescent moieties provides a measure of long-term visualization of viability and proliferation. Early in 2021, Knier et al., from the Foster lab, tracked patient derived xenograft (PDX) cells using MPI and Fluc BLI. Human breast cancer cells, derived from patient brain metastases were engineered to express firefly luciferase, and labelled with SPIO and injected into the fourth mammary fat pad of 5 mice. 2 mice were imaged on BLI for up to 49 days,

while the other 3 mice were imaged on MPI until day 28. It was found that MPI signal decreased over time, while BLI signal increased. While promising, this paper was not a direct comparison between the two modalities. Separate mice were imaged on BLI and MPI. Secondly this paper used Fluc as its BLI reporter rather than the more sensitive Akaluc (174).

Additionally, Makela et al., tracked the fate of breast cancer cells with MPI, BLI and CT *in vivo*. 4T1 cells transduced to express *Luciola Italica* luciferase (Red-FLuc), and labelled with Bang's Beads (MPIO), were injected into the mammary fat pad of mice. This paper successfully demonstrated the ability to track cancer progression and potential metastasis with BLI and MPI, however BLI signal was not quantified, and therefore could not give a complete picture of cell numbers over time (176). The BLI reporter Red-FLuc has a red-shifted emission spectra (peak wavelength = 617 nm) compared to standard Fluc BLI. Although no direct comparison of Red-FLuc and Akaluc BLI has been done, based on the absorption spectra of biological tissues (265,266), Akaluc BLI (peak wavelength = 677 nm) should have far superior depth penetration and therefore sensitivity. No one has yet combined MPI with Akaluc BLI for tracking of any cell type *in vivo*. This work explores the combined modality strategy to image spontaneous metastasizing cancer cells in a preclinical mouse model.

### 1.3 References

1. Brenner, D. R., Weir, H. K., Demers, A. A., Ellison, L. F., Louzado, C., Shaw, A., Turner, D., Woods, R. R., & Smith, L. M. (2020). *Projected estimates of cancer in Canada in 2020*. *Canadian Medical Association Journal*, *192*(9), E199–E205. <https://doi.org/10.1503/cmaj.191292>
2. Canadian Cancer Statistics Advisory Committee. (2019). *Canadian Cancer Statistics 2019*. Canadian Cancer Society, Statistics Canada, the Public Health agency of Canada.
3. Gaudette, L. A., Illing, E. M., & Hill, G. B. (1991). Canadian Cancer Statistics 1991. *Health Reports / Statistics Canada, Canadian Centre for Health Information = Rapports Sur La Santé / Statistique Canada, Centre Canadien d'information Sur La Santé*, *3*(2), 107–135.
4. Dillekås, H., Rogers, M. S., & Straume, O. (2019). Are 90% of deaths from cancer caused by metastases? *Cancer Medicine*, *8*(12), 5574–5576. <https://doi.org/https://doi.org/10.1002/cam4.2474>
5. Patanaphan, V., Salazar, O. M., & Risco, R. (1988). *Breast cancer: metastatic patterns and their prognosis*. *Southern medical journal*, *81*(9), 1109–1112.
6. Ruiterkamp, J., Ernst, M. F., de Munck, L., van der Heiden-van der Loo, M., Bastiaannet, E., van de Poll-Franse, L. V., Bosscha, K., Tjan-Heijnen, V. C., & Voogd, A. C. (2011). *Improved survival of patients with primary distant metastatic breast cancer in the period of 1995-2008. A nationwide population-based study in the Netherlands*. *Breast cancer research and treatment*, *128*(2), 495–503. <https://doi.org/10.1007/s10549-011-1349-x>
7. Maughan, K. L., Lutterbie, M. A., & Ham, P. S. (2010). *Treatment of breast cancer*. *American family physician*, *81*(11), 1339–1346.
8. Barzaman, K., Karami, J., Zarei, Z., Hosseinzadeh, A., Kazemi, M. H., Moradi-Kalbolandi, S., Safari, E., & Farahmand, L. (2020). *Breast cancer: Biology, biomarkers, and treatments*. *International immunopharmacology*, *84*, 106535. <https://doi.org/10.1016/j.intimp.2020.106535>
9. Dees, S., Ganesan, R., Singh, S., & Grewal, I. S. (2020). Emerging CAR-T Cell Therapy for the Treatment of Triple-Negative Breast Cancer. *Molecular Cancer Therapeutics*, *19*(12), 2409 LP – 2421. <https://doi.org/10.1158/1535-7163.MCT-20-0385>
10. Shah, P. D., Huang, A. C. C., Xu, X., Zhang, P. J., Orłowski, R., Matlawski, T., Shea, J., Cervini, A., Amaravadi, R. K., Tchou, J. C., Schuchter, L. M., Wherry, E. J., Linette, G. P., Mick, R., Kulikovskaya, I., Lacey, S. F., Plesa, G., June, C. H., Vonderheide, R. H., & Mitchell, T. C. (2020). Phase I trial of autologous cMET-directed CAR-t cells administered intravenously in patients with melanoma & breast carcinoma. *Journal of Clinical Oncology*, *38*(15\_suppl), 10035. [https://doi.org/10.1200/JCO.2020.38.15\\_suppl.10035](https://doi.org/10.1200/JCO.2020.38.15_suppl.10035)

11. Bajgain, P., Tawinwung, S., D'Elia, L., Sukumaran, S., Watanabe, N., Hoyos, V., Lulla, P., Brenner, M. K., Leen, A. M., & Vera, J. F. (2018). CAR T cell therapy for breast cancer: harnessing the tumor milieu to drive T cell activation. *Journal for immunotherapy of cancer*, 6(1), 34.
12. Byrd, T. T., Fousek, K., Pignata, A., Szot, C., Samaha, H., Seaman, S., Dobrolecki, L., Salsman, V. S., Oo, H. Z., Bielamowicz, K., Landi, D., Rainusso, N., Hicks, J., Powell, S., Baker, M. L., Wels, W. S., Koch, J., Sorensen, P. H., Deneen, B., Ellis, M. J., ... Ahmed, N. (2018). TEM8/ANTXR1-Specific CAR T Cells as a Targeted Therapy for Triple-Negative Breast Cancer. *Cancer research*, 78(2), 489–500. <https://doi.org/10.1158/0008-5472.CAN-16-1911>
13. Zhou, R., Yazdanifar, M., Roy, L. D., Whilding, L. M., Gavrill, A., Maher, J., & Mukherjee, P. (2019). CAR T Cells Targeting the Tumor MUC1 Glycoprotein Reduce Triple-Negative Breast Cancer Growth. *Frontiers in immunology*, 10, 1149. <https://doi.org/10.3389/fimmu.2019.01149>
14. Kim, K. W., Jeong, J. U., Lee, K. H., Uong, T., Rhee, J. H., Ahn, S. J., Kim, S. K., Cho, D., Quang Nguyen, H. P., Pham, C. T., & Yoon, M. S. (2020). Combined NK Cell Therapy and Radiation Therapy Exhibit Long-Term Therapeutic and Antimetastatic Effects in a Human Triple Negative Breast Cancer Model. *International journal of radiation oncology, biology, physics*, 108(1), 115–125. <https://doi.org/10.1016/j.ijrobp.2019.09.041>
15. Hu, Z. (2020). Tissue factor as a new target for CAR-NK cell immunotherapy of triple-negative breast cancer. *Scientific Reports*, 10(1), 1–13. <https://doi.org/10.1038/s41598-020-59736-3>
16. Li, Z., Zheng, W., Wang, H., Cheng, Y., Fang, Y., Wu, F., Sun, G., Sun, G., Lv, C., & Hui, B. (2021). Application of animal models in cancer research: Recent progress and future prospects. *Cancer Management and Research*, 13, 2455–2475. <https://doi.org/10.2147/CMAR.S302565>
17. Little, C. C., & Tyzzer, E.E. (1916). Further experimental studies on the inheritance of susceptibility to a transplantable carcinoma (JA) of the Japanese waltzing mouse. *Journal of Medical Research*. 33: 393–427.
18. Sherer, W.F., Syverton, J.T., Gey, G.O., Studies on the propagation *in vitro* of Poliomyelitis viruses. IV. Viral multiplication in a stable strain of human malignanat epithelial cells (strain HeLa) derived from an epidermoid carcinoma of the cervix. (1953). *Journal of Experimental Medicine*. (5):695-710. doi: 10.1084/jem.97.5.695.
19. Ren, J., Smid, M., Iaria, J., Salvatori, D. C. F., van Dam, H., Zhu, H. J., Martens, J. W. M., & ten Dijke, P. (2019). Cancer-associated fibroblast-derived Gremlin 1 promotes breast cancer progression. *Breast Cancer Research*, 21(1), 109. <https://doi.org/10.1186/s13058-019-1194-0>
20. Zhu, X. Y., Guo, D. W., Lao, Q. C., Xu, Y. Q., Meng, Z. K., Xia, B., Yang, H., Li, C. Q., & Li, P. (2019). Sensitization and synergistic anti-cancer effects of Furanodiene identified in zebrafish models. *Scientific Reports*, 9(1), 1–12. <https://doi.org/10.1038/s41598-019-40866-2>
21. Sentürk, M., Ercan, F., & Yalcin, S. (2020). The secondary metabolites produced by *Lactobacillus plantarum* downregulate BCL-2 and BUFFY genes on breast cancer cell line and model organism *Drosophila melanogaster*: molecular docking approach. *Cancer chemotherapy and pharmacology*, 85(1), 33–45. <https://doi.org/10.1007/s00280-019-03978-0>

22. Tang, M., Zu, C., He, A., Wang, W., Chen, B., & Zheng, X. (2015). Synergistic antitumor effect of adenovirus armed with *Drosophila melanogaster* deoxyribonucleoside kinase and nucleoside analogs for human breast carcinoma in vitro and in vivo. *Drug design, development and therapy*, 9, 3301–3312. <https://doi.org/10.2147/DDDT.S81717>
23. Yamakawa, H., Nagai, T., Harasawa, R., Yamagami, T., Takahashi, J., Ishikawa, K., Nomura, N., & Nagashima, H. (1999). Production of Transgenic Pig Carrying MMTV/v-Ha-ras. *Journal of Reproduction and Development*, 45(2), 111–118. <https://doi.org/10.1262/jrd.45.111>
24. Luo, Y., Li, J., Liu, Y., Lin, L., Du, Y., Li, S., Yang, H., Vajta, G., Callesen, H., Bolund, L., & Sørensen, C. B. (2011). High efficiency of BRCA1 knockout using rAAV-mediated gene targeting: Developing a pig model for breast cancer. *Transgenic Research*, 20(5), 975–988. <https://doi.org/10.1007/s11248-010-9472-8>
25. Walsh, N. C., Kenney, L. L., Jangalwe, S., Aryee, K. E., Greiner, D. L., Brehm, M. A., & Shultz, L. D. (2017). Humanized Mouse Models of Clinical Disease. *Annual review of pathology*, 12, 187–215. <https://doi.org/10.1146/annurev-pathol-052016-100332>
26. Lin, E. Y., Jones, J. G., Li, P., Zhu, L., Whitney, K. D., Muller, W. J., & Pollard, J. W. (2003). Progression to malignancy in the polyoma middle T oncoprotein mouse breast cancer model provides a reliable model for human diseases. *The American journal of pathology*, 163(5), 2113–2126. [https://doi.org/10.1016/S0002-9440\(10\)63568-7](https://doi.org/10.1016/S0002-9440(10)63568-7)
27. Aceto, N., Bardia, A., Miyamoto, D. T., Donaldson, M. C., Wittner, B. S., Spencer, J. A., Yu, M., Pely, A., Engstrom, A., Zhu, H., Brannigan, B. W., Kapur, R., Stott, S. L., Shioda, T., Ramaswamy, S., Ting, D. T., Lin, C. P., Toner, M., Haber, D. A., & Maheswaran, S. (2014). Circulating tumor cell clusters are oligoclonal precursors of breast cancer metastasis. *Cell*, 158(5), 1110–1122. <https://doi.org/10.1016/j.cell.2014.07.013>
28. Gu, Y., Liu, Y., Fu, L., Zhai, L., Zhu, J., Han, Y., Jiang, Y., Zhang, Y., Zhang, P., Jiang, Z., Zhang, X., & Cao, X. (2019). Tumor-educated B cells selectively promote breast cancer lymph node metastasis by HSPA4-targeting IgG. *Nature medicine*, 25(2), 312–322. <https://doi.org/10.1038/s41591-018-0309-y>
29. Olkhanud, P. B., Damdinsuren, B., Bodogai, M., Gress, R. E., Sen, R., Wejksza, K., Malchinkhuu, E., Wersto, R. P., & Biragyn, A. (2011). Tumor-evoked regulatory B cells promote breast cancer metastasis by converting resting CD4<sup>+</sup> T cells to T-regulatory cells. *Cancer research*, 71(10), 3505–3515. <https://doi.org/10.1158/0008-5472.CAN-10-4316>
30. Atlante, S., Visintin, A., Marini, E., Savoia, M., Dianzani, C., Giorgis, M., Sürün, D., Maione, F., Schnütgen, F., Farsetti, A., Zeiher, A. M., Bertinaria, M., Giraudo, E., Spallotta, F., Cencioni, C., & Gaetano, C. (2018).  $\alpha$ -ketoglutarate dehydrogenase inhibition counteracts breast cancer-associated lung metastasis. *Cell death & disease*, 9(7), 756. <https://doi.org/10.1038/s41419-018-0802-8>



31. Arroyo-Crespo, J. J., Armiñán, A., Charbonnier, D., Deladriere, C., Palomino-Schätzlein, M., Lamas-Domingo, R., Forteza, J., Pineda-Lucena, A., & Vicent, M. J. (2019). Characterization of triple-negative breast cancer preclinical models provides functional evidence of metastatic progression. *International journal of cancer*, *145*(8), 2267–2281. <https://doi.org/10.1002/ijc.32270>
32. Jeong, H. Y., Kim, H., Lee, M., Hong, J., Lee, J. H., Kim, J., Choi, M. J., Park, Y. S., & Kim, S. C. (2020). Development of HER2-Specific Aptamer-Drug Conjugate for Breast Cancer Therapy. *International journal of molecular sciences*, *21*(24), 9764. <https://doi.org/10.3390/ijms21249764>
33. Li, F., Miao, L., Xue, T., Qin, H., Mondal, S., Thompson, P. R., Coonrod, S. A., Liu, X., & Zhang, X. (2019). Inhibiting PAD2 enhances the anti-tumor effect of docetaxel in tamoxifen-resistant breast cancer cells. *Journal of experimental & clinical cancer research : CR*, *38*(1), 414. <https://doi.org/10.1186/s13046-019-1404-8>
34. Mohabati Mobarez, A., Soleimani, N., Esmacili, S. A., & Farhangi, B. (2020). Nanoparticle-based immunotherapy of breast cancer using recombinant *Helicobacter pylori* proteins. *European journal of pharmaceuticals and biopharmaceutics : official journal of Arbeitsgemeinschaft fur Pharmazeutische Verfahrenstechnik e.V*, *155*, 69–76. <https://doi.org/10.1016/j.ejpb.2020.08.013>
35. Sagara, M., Miyamoto, S., Itoh, S., Soda, Y., & Tani, K. (2021). Development of New Oncolytic Virotherapy Targeting Breast Cancer Using Coxsackievirus B3. *Anticancer research*, *41*(1), 81–89. <https://doi.org/10.21873/anticancer.14753>
36. Caner, A., Sadiqova, A., Erdoğan, A., Namlises, D., Nalbantsoy, A., Oltulu, F., Toz, S., Yiğittürk, G., Ozkök, E., Gunduz, C., Ozbel, Y., & Haydaroglu, A. (2020). Targeting of antitumor immune responses with live-attenuated *Leishmania* strains in breast cancer model. *Breast cancer (Tokyo, Japan)*, *27*(6), 1082–1095. <https://doi.org/10.1007/s12282-020-01112-0>
37. Ashkbar, A., Rezaei, F., Attari, F., & Ashkevarian, S. (2020). Treatment of breast cancer in vivo by dual photodynamic and photothermal approaches with the aid of curcumin photosensitizer and magnetic nanoparticles. *Scientific reports*, *10*(1), 21206. <https://doi.org/10.1038/s41598-020-78241-1>
38. Lee, J., Park, H. Y., Kim, W. W., Jeong, J. Y., Lee, Y. D., Choi, M. H., Kim, S., Park, J. Y., & Jung, J. H. (2017). Combination Treatment with Photodynamic Therapy and Laser Ablation in Breast Cancer: An Animal Model Study. *Photomedicine and laser surgery*, *35*(9), 505–512. <https://doi.org/10.1089/pho.2017.4291>
39. Silva, C. R., de Almeida Salvego, C., Rostelato, M. E., Zeituni, C. A., & Ribeiro, M. S. (2021). Photobiomodulation therapy combined with radiotherapy in the treatment of triple-negative breast cancer-bearing mice. *Journal of photochemistry and photobiology. B, Biology*, *220*, 112215. <https://doi.org/10.1016/j.jphotobiol.2021.112215>
40. Couillard, S., Gutman, M., Labrie, F., Candas, B., & Labrie, C. (1999). Effect of combined treatment with the pure antiestrogen EM-800 and radiotherapy on the growth of human ZR-75-1 breast cancer xenografts in nude mice. *Cancer research*, *59*(19), 4857–4863.

41. Lopes de Menezes, D. E., Hu, Y., & Mayer, L. D. (2003). Combined treatment of Bcl-2 antisense oligodeoxynucleotides (G3139), p-glycoprotein inhibitor (PSC833), and sterically stabilized liposomal doxorubicin suppresses growth of drug-resistant growth of drug-resistant breast cancer in severely combined immunodeficient mice. *Journal of experimental therapeutics & oncology*, 3(2), 72–82. <https://doi.org/10.1046/j.1359-4117.2003.01075.x>
42. Yu, E. Y., Bishop, M., Zheng, B., Ferguson, R. M., Khandhar, A. P., Kemp, S. J., Krishnan, K. M., Goodwill, P. W., & Conolly, S. M. (2017). Magnetic Particle Imaging: A Novel in Vivo Imaging Platform for Cancer Detection. *Nano Letters*, 17(3), 1648–1654. <https://doi.org/10.1021/acs.nanolett.6b04865>
43. Altine, B., Gai, Y., Han, N., Jiang, Y., Ji, H., Fang, H., Niyonkuru, A., Bakari, K. H., Rajab Arnous, M. M., Liu, Q., Zhang, Y., & Lan, X. (2019). Preclinical Evaluation of a Fluorine-18 (<sup>18</sup>F)-Labeled Phosphatidylinositol 3-Kinase Inhibitor for Breast Cancer Imaging. *Molecular pharmaceutics*, 16(11), 4563–4571. <https://doi.org/10.1021/acs.molpharmaceut.9b00690>
44. Paquette, M., Phoenix, S., Lawson, C., Guérin, B., Lecomte, R., Tai, L. H., Turcotte, É. E., & Leyton, J. V. (2020). A preclinical PET dual-tracer imaging protocol for ER and HER2 phenotyping in breast cancer xenografts. *European Journal of Nuclear Medicine and Molecular Imaging research*, 10(1), 69. <https://doi.org/10.1186/s13550-020-00656-8>
45. Savolainen, H., Volpe, A., Phinikaridou, A., Douek, M., Fruhwirth, G., & de Rosales, R. (2019). <sup>68</sup>Ga-Sienna+ for PET-MRI Guided Sentinel Lymph Node Biopsy: Synthesis and Preclinical Evaluation in a Metastatic Breast Cancer Model. *Nanotheranostics*, 3(3), 255–265. <https://doi.org/10.7150/ntno.34727>
46. Fiordelisi, M. F., Auletta, L., Meomartino, L., Basso, L., Fatone, G., Salvatore, M., Mancini, M., & Greco, A. (2019). Preclinical Molecular Imaging for Precision Medicine in Breast Cancer Mouse Models. *Contrast media & molecular imaging*, 2019, 8946729. <https://doi.org/10.1155/2019/8946729>
47. Ciampricotti, M., Vrijland, K., Hau, C.-S., Pemovska, T., Doornebal, C.W., Speksnijder, E.N., Wartha, K., Jonkers, J. and de Visser, K.E. (2011), Development of metastatic HER2<sup>+</sup> breast cancer is independent of the adaptive immune system. *Journal of Pathology*, 224: 56-66. <https://doi.org/10.1002/path.2837>
48. Knutson, K. L., Dang, Y., Lu, H., Lukas, J., Almand, B., Gad, E., Azeke, E., & Disis, M. L. (2006). IL-2 immunotoxin therapy modulates tumor-associated regulatory T cells and leads to lasting immune-mediated rejection of breast cancers in neu-transgenic mice. *Journal of immunology (Baltimore, Md. : 1950)*, 177(1), 84–91. <https://doi.org/10.4049/jimmunol.177.1.84>
49. Calogero, R. A., Cordero, F., Forni, G., & Cavallo, F. (2007). Inflammation and breast cancer. Inflammatory component of mammary carcinogenesis in ErbB2 transgenic mice. *Breast cancer research : BCR*, 9(4), 211. <https://doi.org/10.1186/bcr1745>

50. Dewan, M. Z., Terunuma, H., Ahmed, S., Ohba, K., Takada, M., Tanaka, Y., Toi, M., & Yamamoto, N. (2005). Natural killer cells in breast cancer cell growth and metastasis in SCID mice. *Biomedicine & Pharmacotherapy*, *59*, S375–S379. [https://doi.org/https://doi.org/10.1016/S0753-3322\(05\)80082-4](https://doi.org/https://doi.org/10.1016/S0753-3322(05)80082-4)
51. Dadi, S., Chhangawala, S., Whitlock, B. M., Franklin, R. A., Luo, C. T., Oh, S. A., Toure, A., Pritykin, Y., Huse, M., Leslie, C. S., & Li, M. O. (2016). Cancer Immunosurveillance by Tissue-Resident Innate Lymphoid Cells and Innate-like T Cells. *Cell*, *164*(3), 365–377. <https://doi.org/https://doi.org/10.1016/j.cell.2016.01.002>
52. Kircher, M. F., Gambhir, S. S., & Grimm, J. (2011). Noninvasive cell-tracking methods. *Nature Reviews Clinical Oncology*, *8*(11), 677–688. <https://doi.org/10.1038/nrclinonc.2011.141>
53. James, M. L., & Gambhir, S. S. (2012). A molecular imaging primer: Modalities, imaging agents, and applications. *Physiological Reviews*, *92*(2), 897–965. <https://doi.org/10.1152/physrev.00049.2010>
54. Modo, M. (2008). Noninvasive imaging of transplanted cells. *Current Opinion in Organ Transplantation*, *13*(6), 654–658. <https://doi.org/10.1097/MOT.0b013e328317a43c>
55. Wang, Y-XJ. (2011). Superparamagnetic iron oxide based MRI contrast agents: Current status of clinical application. *Quantitative Imaging and Medical Surgery*, *1*(1), 35-40. doi:10.3978/j.issn.2223-4292.2011.08.03
56. Gustafson, H.H., Holt-Casper, D., Grainger, D.W., Ghandehari, H. (2015). Nanoparticle Uptake: The Phagocyte Problem Graphical Abstract. *Nano Today*, *10*(4):487-510. doi: 10.1016/j.nantod.2015.06.006.Nanoparticle
57. Hinds, K. A., Hill, J. M., Shapiro, E. M., Laukkanen, M. O., Silva, A. C., Combs, C. A., Varney, T. R., Balaban, R. S., Koretsky, A. P., & Dunbar, C. E. (2003). Highly efficient endosomal labeling of progenitor and stem cells with large magnetic particles allows magnetic resonance imaging of single cells. *Blood*, *102*(3), 867–872. <https://doi.org/10.1182/blood-2002-12-3669>
58. Heyn, C., Ronald, J. A., Mackenzie, L. T., MacDonald, I. C., Chambers, A. F., Rutt, B. K., & Foster, P. J. (2006). In vivo magnetic resonance imaging of single cells in mouse brain with optical validation. *Magnetic resonance in medicine*, *55*(1), 23–29. <https://doi.org/10.1002/mrm.20747>
59. Heyn, C., Ronald, J. A., Ramadan, S. S., Snir, J. A., Barry, A. M., MacKenzie, L. T., Mikulis, D. J., Palmieri, D., Bronder, J. L., Steeg, P. S., Yoneda, T., MacDonald, I. C., Chambers, A. F., Rutt, B. K., & Foster, P. J. (2006). In vivo MRI of cancer cell fate at the single-cell level in a mouse model of breast cancer metastasis to the brain. *Magnetic resonance in medicine*, *56*(5), 1001–1010. <https://doi.org/10.1002/mrm.21029>
60. Foster, P. J., Dunn, E. A., Karl, K. E., Snir, J. A., Nycz, C. M., Harvey, A. J., & Pettis, R. J. (2008). Cellular magnetic resonance imaging: in vivo imaging of melanoma cells in lymph nodes of mice. *Neoplasia (New York, N.Y.)*, *10*(3), 207–216. <https://doi.org/10.1593/neo.07937>
61. Shapiro, E.M., Sharer, K., Skrtic, S. and Koretsky, A.P. (2006), In vivo detection of single cells by MRI. *Magnetic Resonance in Medicine*, *55*: 242-249. <https://doi.org/10.1002/mrm.20718>

62. Shapiro, E. M., Medford-Davis, L. N., Fahmy, T. M., Dunbar, C. E., & Koretsky, A. P. (2007). Antibody-mediated cell labeling of peripheral T cells with micron-sized iron oxide particles (MPIOs) allows single cell detection by MRI. *Contrast media & molecular imaging*, 2(3), 147–153. <https://doi.org/10.1002/cmml.134>
63. Cohen, B., Dafni, H., Meir, G., Harmelin, A., & Neeman, M. (2005). Ferritin as an Endogenous MRI Reporter for Noninvasive Imaging of Gene Expression in C6 Glioma Tumors. *Neoplasia*, 7(2), 109–117. <https://doi.org/https://doi.org/10.1593/neo.04436>
64. Genove, G., DeMarco, U., Xu, H., Goins, W. F., & Ahrens, E. T. (2005). A new transgene reporter for in vivo magnetic resonance imaging. *Nature Medicine*, 11(4), 450–454. <https://doi.org/10.1038/nm1208>
65. Liu, J., Cheng, E. C. H., Long, R. C., Yang, S.-H., Wang, L., Cheng, P.-H., Yang, J., Wu, D., Mao, H., & Chan, A. W. S. (2009). Noninvasive Monitoring of Embryonic Stem Cells In Vivo with MRI Transgene Reporter. *Tissue Engineering Part C: Methods*, 15(4), 739–747. <https://doi.org/10.1089/ten.tec.2008.0678>
66. Cohen, B., Ziv, K., Plaks, V., Israely, T., Kalchenko, V., Harmelin, A., Benjamin, L. E., & Neeman, M. (2007). MRI detection of transcriptional regulation of gene expression in transgenic mice. *Nature Medicine*, 13(4), 498–503. <https://doi.org/10.1038/nm1497>
67. Vande Velde, G., Rangarajan, J. R., Toelen, J., Dresselaers, T., Ibrahimi, A., Krylychkina, O., Vreys, R., Van der Linden, A., Maes, F., Debyser, Z., Himmelreich, U., & Baekelandt, V. (2011). Evaluation of the specificity and sensitivity of ferritin as an MRI reporter gene in the mouse brain using lentiviral and adeno-associated viral vectors. *Gene Therapy*, 18(6), 594–605. <https://doi.org/10.1038/gt.2011.2>
68. Makela, A. V., Murrell, D. H., Parkins, K. M., Kara, J., Gaudet, J. M., & Foster, P. J. (2016). Cellular imaging with MRI. *Topics in Magnetic Resonance Imaging*, 25(5), 177–186. <https://doi.org/10.1097/RMR.000000000000101>
69. Economopoulos, V., Chen, Y., McFadden, C., & Foster, P. J. (2013). MRI detection of nonproliferative tumor cells in lymph node metastases using iron oxide particles in a mouse model of breast cancer. *Translational oncology*, 6(3), 347–354. <https://doi.org/10.1593/tlo.13121>
70. Amsalem, Y., Mardor, Y., Feinberg, M. S., Landa, N., Miller, L., Daniels, D., Ocherashvilli, A., Holbova, R., Yosef, O., Barbash, I. M., & Leor, J. (2007). Iron-oxide labeling and outcome of transplanted mesenchymal stem cells in the infarcted myocardium. *Circulation*, 116(11 Suppl), I38–I45. <https://doi.org/10.1161/CIRCULATIONAHA.106.680231>
71. Kedziorek, D. A., & Kraitchman, D. L. (2010). Superparamagnetic iron oxide labeling of stem cells for MRI tracking and delivery in cardiovascular disease. *Methods in molecular biology (Clifton, N.J.)*, 660, 171–183. [https://doi.org/10.1007/978-1-60761-705-1\\_11](https://doi.org/10.1007/978-1-60761-705-1_11)

72. Hedlund, A., Ahrén, M., Gustafsson, H., Abrikossova, N., Warntjes, M., Jönsson, J. I., Uvdal, K., & Engström, M. (2011). Gd<sub>2</sub>O<sub>3</sub> nanoparticles in hematopoietic cells for MRI contrast enhancement. *International journal of nanomedicine*, 6, 3233–3240. <https://doi.org/10.2147/IJN.S23940>
73. Tzu-Chen, Y., Weiguo Zhang, S. T., Ildstad Chien, H. (1993). Intracellular labelling of T-cells with superparamagnetic contrast agents. *Magnetic Resonance in Medicine*, 30(5):617–625
74. Bulte, J.W.M., Brooks, R. A. (1997). Magnetic Nanoparticles as Contrast Agents for MR Imaging. *Sci Clin Appl Magn Carriers*, 527–543
75. Boros, E., Gale, E. M., & Caravan, P. (2015). MR imaging probes: design and applications. *Dalton transactions (Cambridge, England : 2003)*, 44(11), 4804–4818. <https://doi.org/10.1039/c4dt02958e>
76. Gale, E. M., Atanasova, I. P., Blasi, F., Ay, I., & Caravan, P. (2015). A Manganese Alternative to Gadolinium for MRI Contrast. *Journal of the American Chemical Society*, 137(49), 15548–15557. <https://doi.org/10.1021/jacs.5b10748>
77. Pellico, J., Ellis, C. M., & Davis, J. J. (2019). Nanoparticle-Based Paramagnetic Contrast Agents for Magnetic Resonance Imaging. *Contrast media & molecular imaging*, 2019, 1845637. <https://doi.org/10.1155/2019/1845637>
78. Mitchell D. G. (1996). Liver I: Currently available gadolinium chelates. *Magnetic resonance imaging clinics of North America*, 4(1), 37–51.
79. Wood, M. L., & Hardy, P. A. (1993). Proton relaxation enhancement. *Journal of magnetic resonance imaging*, 3(1), 149–156. <https://doi.org/10.1002/jmri.1880030127>
80. Goldman, E., Zinger, A., Da Silva, D., Yaari, Z., Kajal, A., Vardi-Okinin, D., Goldfeder, M., Schroeder, J. E., Shainsky-Roitman, J., Hershkovitz, D., & Schroeder, A. (2017). Nanoparticles target early-stage breast cancer metastasis in vivo. *Nanotechnology*, 28(43). <https://doi.org/10.1088/1361-6528/aa8a3d>
81. Sterenczak, K. A., Meier, M., Glage, S., Meyer, M., Willenbrock, S., Wefstaedt, P., Dorsch, M., Bullerdiek, J., Murua Escobar, H., Hedrich, H., & Nolte, I. (2012). Longitudinal MRI contrast enhanced monitoring of early tumour development with manganese chloride (MnCl<sub>2</sub>) and superparamagnetic iron oxide nanoparticles (SPIOs) in a CT1258 based in vivo model of prostate cancer. *BMC cancer*, 12, 284. <https://doi.org/10.1186/1471-2407-12-284>
82. Burtea, C., Laurent, S., Vander Elst, L., & Muller, R. N. (2008). Contrast Agents: Magnetic Resonance. In W. Semmler & M. Schwaiger (Eds.), *Molecular Imaging I* (pp. 135–165). Springer Berlin Heidelberg. [https://doi.org/10.1007/978-3-540-72718-7\\_7](https://doi.org/10.1007/978-3-540-72718-7_7)
83. Alford, R., Ogawa, M., Choyke, P. L., & Kobayashi, H. (2009). Molecular probes for the in vivo imaging of cancer. *Molecular BioSystems*, 5(11), 1279–1291. <https://doi.org/10.1039/b911307j>
84. Hoehn, M., Himmelreich, U., Kruttwig, K., & Wiedermann, D. (2008). Molecular and cellular MR imaging: Potentials and challenges for neurological applications. *Journal of Magnetic Resonance Imaging*, 27(5), 941–954. <https://doi.org/https://doi.org/10.1002/jmri.21280>

85. Jasmin, Torres, A. L. M., Nunes, H. M. P., Passipieri, J. A., Jelicks, L. A., Gasparetto, E. L., Spray, D. C., Campos de Carvalho, A. C., & Mendez-Otero, R. (2011). Optimized labeling of bone marrow mesenchymal cells with superparamagnetic iron oxide nanoparticles and in vivo visualization by magnetic resonance imaging. *Journal of Nanobiotechnology*, 9(1), 4. <https://doi.org/10.1186/1477-3155-9-4>
86. Cromer Berman, S. M., Walczak, P., & Bulte, J. W. M. (2011). Tracking stem cells using magnetic nanoparticles. *WIREs Nanomedicine and Nanobiotechnology*, 3(4), 343–355. <https://doi.org/https://doi.org/10.1002/wnan.140>
87. Yurt, A., & Kazancı, N. (2008). Investigation of magnetic properties of various complexes prepared as contrast agents for MRI. *Journal of Molecular Structure*, 892(1), 392–397. <https://doi.org/https://doi.org/10.1016/j.molstruc.2008.06.024>
88. Shokrollahi, H. (2013). Contrast agents for MRI. *Materials Science and Engineering: C*, 33(8), 4485–4497. <https://doi.org/https://doi.org/10.1016/j.msec.2013.07.012>
89. Shetty, A. S., Sipe, A. L., Zulfiqar, M., Tsai, R., Raptis, D. A., Raptis, C. A., & Bhalla, S. (2019). In-phase and opposed-phase imaging: Applications of chemical shift and magnetic susceptibility in the chest and abdomen. *Radiographics*, 39(1), 115–135. <https://doi.org/10.1148/rg.2019180043>
90. Liu, W., Dahnke, H., Jordan, E. K., Schaeffter, T., & Frank, J. A. (2008). In vivo MRI using positive-contrast techniques in detection of cells labeled with superparamagnetic iron oxide nanoparticles. *NMR in Biomedicine*, 21(3), 242–250. <https://doi.org/https://doi.org/10.1002/nbm.1187>
91. Daldrup-Link, H. E., Golovko, D., Ruffell, B., Denardo, D. G., Castaneda, R., Ansari, C., Rao, J., Tikhomirov, G. A., Wendland, M. F., Corot, C., & Coussens, L. M. (2011). MRI of tumor-associated macrophages with clinically applicable iron oxide nanoparticles. *Clinical cancer research : an official journal of the American Association for Cancer Research*, 17(17), 5695–5704. <https://doi.org/10.1158/1078-0432.CCR-10-3420>
92. Shih, Y. Y., Hsu, Y. H., Duong, T. Q., Lin, S. S., Chow, K. P., & Chang, C. (2011). Longitudinal study of tumor-associated macrophages during tumor expansion using MRI. *NMR in biomedicine*, 24(10), 1353–1360. <https://doi.org/10.1002/nbm.1698>
93. Keselman, P., Yu, E. Y., Zhou, X. Y., Goodwill, P. W., Chandrasekharan, P., Ferguson, R. M., Khandhar, A. P., Kemp, S. J., Krishnan, K. M., Zheng, B., & Conolly, S. M. (2017). Tracking short-term biodistribution and long-term clearance of SPIO tracers in magnetic particle imaging. *Physics in Medicine and Biology*, 62(9), 3440–3453. <https://doi.org/10.1088/1361-6560/aa5f48>

94. Jain, T. K., Reddy, M. K., Morales, M. A., Leslie-Pelecky, D. L., & Labhasetwar, V. (2008). Biodistribution, Clearance, and Biocompatibility of Iron Oxide Magnetic Nanoparticles in Rats. *Molecular Pharmaceutics*, 5(2), 316–327. <https://doi.org/10.1021/mp7001285>
95. Bulte, J. W., Douglas, T., Mann, S., Vymazal, J., Laughlin, P. G., & Frank, J. A. (1995). Initial assessment of magnetoferritin biokinetics and proton relaxation enhancement in rats. *Academic radiology*, 2(10), 871–878. [https://doi.org/10.1016/s1076-6332\(05\)80064-9](https://doi.org/10.1016/s1076-6332(05)80064-9)
96. Shi, Q., Pisani, L. J., Lee, Y. K., Messing, S., Ansari, C., Bhaumik, S., Lowery, L., Lee, B. D., Meyer, D. E., & Daldrup-Link, H. E. (2013). Evaluation of the novel USPIO GEH121333 for MR imaging of cancer immune responses. *Contrast Media and Molecular Imaging*, 8(3), 281–288. <https://doi.org/10.1002/cmml.1526>
97. Leimgruber, A., Berger, C., Cortez-Retamozo, V., Etzrodt, M., Newton, A. P., Waterman, P., Figueiredo, J. L., Kohler, R. H., Elpek, N., Mempel, T. R., Swirski, F. K., Nahrendorf, M., Weissleder, R., & Pittet, M. J. (2009). Behavior of endogenous tumor-associated macrophages assessed in vivo using a functionalized nanoparticle. *Neoplasia (New York, N.Y.)*, 11(5), 459–468. <https://doi.org/10.1593/neo.09356>
98. Seyfer, P., Pagenstecher, A., Mandic, R., Klose, K. J., & Heverhagen, J. T. (2014). Cancer and inflammation: differentiation by USPIO-enhanced MR imaging. *Journal of magnetic resonance imaging*, 39(3), 665–672. <https://doi.org/10.1002/jmri.24200>
99. Lauridsen, H., Foldager, C. B., Hansen, L., & Pedersen, M. (2018). Non-invasive cell tracking of SPIO labeled cells in an intrinsic regenerative environment: The axolotl limb. *Experimental and therapeutic medicine*, 15(4), 3311–3319. <https://doi.org/10.3892/etm.2018.5865>
100. Chen, L., Zang, F., Wu, H., Li, J., Xie, J., Ma, M., Gu, N., & Zhang, Y. (2018). Using PEGylated magnetic nanoparticles to describe the EPR effect in tumor for predicting therapeutic efficacy of micelle drugs. *Nanoscale*, 10(4), 1788–1797. <https://doi.org/10.1039/c7nr08319j>
101. Kokuryo, D., Anraku, Y., Kishimura, A., Tanaka, S., Kano, M. R., Kershaw, J., Nishiyama, N., Saga, T., Aoki, I., & Kataoka, K. (2013). SPIO-PICsome: Development of a highly sensitive and stealth-capable MRI nano-agent for tumor detection using SPIO-loaded unilamellar polyion complex vesicles (PICsomes). *Journal of Controlled Release*, 169(3), 220–227. <https://doi.org/https://doi.org/10.1016/j.jconrel.2013.03.016>
102. Arbab, A. S., Yocum, G. T., Kalish, H., Jordan, E. K., Anderson, S. A., Khakoo, A. Y., Read, E. J., & Frank, J. A. (2004). Efficient magnetic cell labeling with protamine sulfate complexed to ferumoxides for cellular MRI. *Blood*, 104(4), 1217–1223. <https://doi.org/10.1182/blood-2004-02-0655>
103. Frank, J. A., Zywicke, H., Jordan, E. K., Mitchell, J., Lewis, B. K., Miller, B., Bryant, L. H., Jr, & Bulte, J. W. (2002). Magnetic intracellular labeling of mammalian cells by combining (FDA-approved) superparamagnetic iron oxide MR contrast agents and commonly used transfection agents. *Academic radiology*, 9 Suppl 2, S484–S487. [https://doi.org/10.1016/s1076-6332\(03\)80271-4](https://doi.org/10.1016/s1076-6332(03)80271-4)
104. Frank, J. A., Miller, B. R., Arbab, A. S., Zywicke, H. A., Jordan, E. K., Lewis, B. K., Bryant, L. H., Jr, & Bulte, J. W. (2003). Clinically applicable labeling of mammalian and stem cells by

combining superparamagnetic iron oxides and transfection agents. *Radiology*, 228(2), 480–487. <https://doi.org/10.1148/radiol.2281020638>

105. Bulte, J. W., & Kraitchman, D. L. (2004). Iron oxide MR contrast agents for molecular and cellular imaging. *NMR in biomedicine*, 17(7), 484–499. <https://doi.org/10.1002/nbm.924>
106. Gonzalez-Lara, L. E., Xu, X., Hofstetrova, K., Pniak, A., Chen, Y., McFadden, C. D., Martinez-Santesteban, F. M., Rutt, B. K., Brown, A., & Foster, P. J. (2011). The use of cellular magnetic resonance imaging to track the fate of iron-labeled multipotent stromal cells after direct transplantation in a mouse model of spinal cord injury. *Molecular imaging and biology*, 13(4), 702–711. <https://doi.org/10.1007/s11307-010-0393-y>
107. Walczak, P., Kedziorek, D. A., Gilad, A. A., Lin, S., & Bulte, J. W. (2005). Instant MR labeling of stem cells using magnetoelectroporation. *Magnetic resonance in medicine*, 54(4), 769–774. <https://doi.org/10.1002/mrm.20701>
108. Kedziorek, D. A., & Kraitchman, D. L. (2010). Superparamagnetic iron oxide labeling of stem cells for MRI tracking and delivery in cardiovascular disease. *Methods in molecular biology (Clifton, N.J.)*, 660, 171–183. [https://doi.org/10.1007/978-1-60761-705-1\\_11](https://doi.org/10.1007/978-1-60761-705-1_11)
109. Ahrens, E. T., Feili-Hariri, M., Xu, H., Genove, G., & Morel, P. A. (2003). Receptor-mediated endocytosis of iron-oxide particles provides efficient labeling of dendritic cells for in vivo MR imaging. *Magnetic resonance in medicine*, 49(6), 1006–1013. <https://doi.org/10.1002/mrm.10465>
110. Dekaban, G. A., Snir, J., Shrum, B., de Chickera, S., Willert, C., Merrill, M., Said, E. A., Sekaly, R. P., Foster, P. J., & O'Connell, P. J. (2009). Semiquantitation of mouse dendritic cell migration in vivo using cellular MRI. *Journal of immunotherapy (Hagerstown, Md. : 1997)*, 32(3), 240–251. <https://doi.org/10.1097/CJI.0b013e318197b2a0>
111. Zhang, X., de Chickera, S. N., Willert, C., Economopoulos, V., Noad, J., Rohani, R., Wang, A. Y., Levings, M. K., Scheid, E., Foley, R., Foster, P. J., & Dekaban, G. A. (2011). Cellular magnetic resonance imaging of monocyte-derived dendritic cell migration from healthy donors and cancer patients as assessed in a scid mouse model. *Cytotherapy*, 13(10), 1234–1248. <https://doi.org/10.3109/14653249.2011.605349>
112. Rohani, R., de Chickera, S. N., Willert, C., Chen, Y., Dekaban, G. A., & Foster, P. J. (2011). In vivo cellular MRI of dendritic cell migration using micrometer-sized iron oxide (MPIO) particles. *Molecular imaging and biology*, 13(4), 679–694. <https://doi.org/10.1007/s11307-010-0403-0>
113. de Chickera, S., Willert, C., Mallet, C., Foley, R., Foster, P., & Dekaban, G. A. (2012). Cellular MRI as a suitable, sensitive non-invasive modality for correlating in vivo migratory efficiencies of different dendritic cell populations with subsequent immunological outcomes. *International immunology*, 24(1), 29–41. <https://doi.org/10.1093/intimm/dxr095>



114. Bernas, L. M., Foster, P. J., & Rutt, B. K. (2010). Imaging iron-loaded mouse glioma tumors with bSSFP at 3 T. *Magnetic resonance in medicine*, *64*(1), 23–31. <https://doi.org/10.1002/mrm.22210>
115. Magnitsky, S., Roesch, A., Herlyn, M., & Glickson, J. D. (2011). In vivo and ex vivo MR imaging of slowly cycling melanoma cells. *Magnetic resonance in medicine*, *66*(5), 1362–1373. <https://doi.org/10.1002/mrm.22917>
116. Ribot, E. J., Martinez-Santesteban, F. M., Simeanea, C., Steeg, P. S., Chambers, A. F., Rutt, B. K., & Foster, P. J. (2011). In vivo single scan detection of both iron-labeled cells and breast cancer metastases in the mouse brain using balanced steady-state free precession imaging at 1.5 T. *Journal of magnetic resonance imaging*, *34*(1), 231–238. <https://doi.org/10.1002/jmri.22593>
117. Parkins, K. M., Hamilton, A. M., Dubois, V. P., Wong, S. M., Foster, P. J., & Ronald, J. A. (2019). Cellular MRI reveals altered brain arrest of genetically engineered metastatic breast cancer cells. *Contrast Media and Molecular Imaging*. <https://doi.org/10.1155/2019/6501231>
118. Chen, J., Ren, G., Cai, R., Wu, X., Gui, T., Zhao, J., Li, H., & Guo, C. (2019). Cellular magnetic resonance imaging: in vivo tracking of gastric cancer cells and detecting of lymph node metastases using microparticles of iron oxide in mice. *Cancer management and research*, *11*, 7317–7326. <https://doi.org/10.2147/CMAR.S206043>
119. Brekke, C., Morgan, S. C., Lowe, A. S., Meade, T. J., Price, J., Williams, S. C., & Modo, M. (2007). The in vitro effects of a bimodal contrast agent on cellular functions and relaxometry. *NMR in biomedicine*, *20*(2), 77–89. <https://doi.org/10.1002/nbm.1077>
120. Modo, M., Beech, J. S., Meade, T. J., Williams, S. C., & Price, J. (2009). A chronic 1 year assessment of MRI contrast agent-labelled neural stem cell transplants in stroke. *NeuroImage*, *47 Suppl 2*(0 2), T133–T142. <https://doi.org/10.1016/j.neuroimage.2008.06.017>
121. Soenen, S. J. H., Illyes, E., Vercauteren, D., Braeckmans, K., Majer, Z., De Smedt, S. C., & De Cuyper, M. (2009). The role of nanoparticle concentration-dependent induction of cellular stress in the internalization of non-toxic cationic magnetoliposomes. *Biomaterials*, *30*(36), 6803–6813. <https://doi.org/https://doi.org/10.1016/j.biomaterials.2009.08.050>
122. Jeng, H. A., & Swanson, J. (2006). Toxicity of metal oxide nanoparticles in mammalian cells. *Journal of environmental science and health. Part A, Toxic/hazardous substances & environmental engineering*, *41*(12), 2699–2711. <https://doi.org/10.1080/10934520600966177>
123. Manke, A., Wang, L., & Rojanasakul, Y. (2013). Mechanisms of nanoparticle-induced oxidative stress and toxicity. *BioMed research international*, *2013*, 942916. <https://doi.org/10.1155/2013/942916>
124. Nel, A., Xia, T., Mädler, L., & Li, N. (2006). Toxic Potential of Materials at the Nanolevel. *Science*, *311*(5761), 622–627. <https://doi.org/10.1126/science.1114397>
125. Li, N., Xia, T., & Nel, A. E. (2008). The role of oxidative stress in ambient particulate matter-induced lung diseases and its implications in the toxicity of engineered nanoparticles. *Free Radical Biology and Medicine*, *44*(9), 1689–1699. <https://doi.org/https://doi.org/10.1016/j.freeradbiomed.2008.01.028>

126. Singh, N., Jenkins, G. J., Asadi, R., & Doak, S. H. (2010). Potential toxicity of superparamagnetic iron oxide nanoparticles (SPION). *Nano reviews*, *1*, 10.3402/nano.v1i0.5358. <https://doi.org/10.3402/nano.v1i0.5358>
127. Doak, S. H., Manshian, B., Jenkins, G. J., & Singh, N. (2012). In vitro genotoxicity testing strategy for nanomaterials and the adaptation of current OECD guidelines. *Mutation research*, *745*(1-2), 104–111. <https://doi.org/10.1016/j.mrgentox.2011.09.013>
128. Sharifi, S., Daghighi, s, Motazacker, M., Badlou, B., Sanjabi, B., Akbarkhanzadeh, A., Rowshani, A., Laurent, S., Peppelenbosch, M., & Rezaee, F. (2013). Superparamagnetic iron oxide nanoparticles alter expression of obesity and T2D-associated risk genes in human adipocytes. *Scientific Reports*, *3*, 2173. <https://doi.org/10.1038/srep02173>
129. Yildirimer, L., Thanh, N. T. K., Loizidou, M., & Seifalian, A. M. (2011). Toxicology and clinical potential of nanoparticles. *Nano Today*, *6*(6), 585–607. <https://doi.org/https://doi.org/10.1016/j.nantod.2011.10.001>
130. Saha, S., Yang, X., Tanner, S., Curran, S., Wood, D., & Kirkham, J. (2013). The effects of iron oxide incorporation on the chondrogenic potential of three human cell types. *Journal of Tissue Engineering and Regenerative Medicine*, *7*. <https://doi.org/10.1002/term.544>
131. Liu, W., & Frank, J. A. (2009). Detection and quantification of magnetically labeled cells by cellular MRI. *European journal of radiology*, *70*(2), 258–264. <https://doi.org/10.1016/j.ejrad.2008.09.021>
132. Bulte, J. W., Walczak, P., Janowski, M., Krishnan, K. M., Arami, H., Halkola, A., Gleich, B., & Rahmer, J. (2015). Quantitative "Hot Spot" Imaging of Transplanted Stem Cells using Superparamagnetic Tracers and Magnetic Particle Imaging (MPI). *Tomography (Ann Arbor, Mich.)*, *1*(2), 91–97. <https://doi.org/10.18383/j.tom.2015.00172>
133. Sehl, O. C., Gevaert, J. J., Melo, K. P., Knier, N. N., & Foster, P. J. (2020). A perspective on cell tracking with magnetic particle imaging. *Tomography*, *6*(4), 315–324. <https://doi.org/10.18383/j.tom.2020.00043>
134. Curtis, W. A., Fraum, T. J., An, H., Chen, Y., Shetty, A. S., & Fowler, K. J. (2019). Quantitative MRI of Diffuse Liver Disease: Current Applications and Future Directions. *Radiology*, *290*(1), 23–30. <https://doi.org/10.1148/radiol.2018172765>
135. Madhuranthakam, A. J., Yuan, Q., & Pedrosa, I. (2017). Quantitative Methods in Abdominal MRI: Perfusion Imaging. *Topics in magnetic resonance imaging*, *26*(6), 251–258. <https://doi.org/10.1097/RMR.000000000000145>
136. Eckstein, F., Burstein, D., & Link, T. M. (2006). Quantitative MRI of cartilage and bone: degenerative changes in osteoarthritis. *NMR in biomedicine*, *19*(7), 822–854. <https://doi.org/10.1002/nbm.1063>

137. Cai, K., Tain, R., Das, S., Damen, F. C., Sui, Y., Valyi-Nagy, T., Elliott, M. A., & Zhou, X. J. (2015). The feasibility of quantitative MRI of perivascular spaces at 7T. *Journal of neuroscience methods*, 256, 151–156. <https://doi.org/10.1016/j.jneumeth.2015.09.001>
138. Gleich, B. (2001). Verfahren zur Ermittlung der räumlichen Verteilung magnetischer Partikel. *German Patent DE-10151778-A1*.
139. Gleich, B., & Weizenecker, J. (2005). Tomographic imaging using the nonlinear response of magnetic particles. *Nature*, 435(7046), 1214–1217. <https://doi.org/10.1038/nature03808>
140. Reimer, P., & Balzer, T. (2003). Ferucarbotran (Resovist): a new clinically approved RES-specific contrast agent for contrast-enhanced MRI of the liver: properties, clinical development, and applications. *European radiology*, 13(6), 1266–1276. <https://doi.org/10.1007/s00330-002-1721-7>
141. Saritas, E. U., Goodwill, P. W., Croft, L. R., Konkle, J. J., Lu, K., Zheng, B., & Conolly, S. M. (2013). Magnetic particle imaging (MPI) for NMR and MRI researchers. *Journal of magnetic resonance (San Diego, Calif. : 1997)*, 229, 116–126. <https://doi.org/10.1016/j.jmr.2012.11.029>
142. Zheng, B., Yu, E., Orendorff, R., Lu, K., Konkle, J. J., Tay, Z. W., Hensley, D., Zhou, X. Y., Chandrasekharan, P., Saritas, E. U., Goodwill, P. W., Hazle, J. D., & Conolly, S. M. (2017). Seeing SPIOs Directly In Vivo with Magnetic Particle Imaging. *Molecular imaging and biology*, 19(3), 385–390. <https://doi.org/10.1007/s11307-017-1081-y>
143. Wu, L. C., Zhang, Y., Steinberg, G., Qu, H., Huang, S., Cheng, M., Bliss, T., Du, F., Rao, J., Song, G., Pisani, L., Doyle, T., Conolly, S., Krishnan, K., Grant, G., & Wintermark, M. (2019). A Review of Magnetic Particle Imaging and Perspectives on Neuroimaging. *AJNR. American journal of neuroradiology*, 40(2), 206–212. <https://doi.org/10.3174/ajnr.A5896>
144. Talebloo, N., Gudi, M., Robertson, N., & Wang, P. (2020). Magnetic Particle Imaging: Current Applications in Biomedical Research. *Journal of magnetic resonance imaging*, 51(6), 1659–1668. <https://doi.org/10.1002/jmri.26875>
145. Lu, K., Goodwill, P. W., Saritas, E. U., Zheng, B., & Conolly, S. M. (2013). Linearity and shift invariance for quantitative magnetic particle imaging. *IEEE transactions on medical imaging*, 32(9), 1565–1575. <https://doi.org/10.1109/TMI.2013.2257177>
146. Bulte, J. W. M., Walczak, P., Gleich, B., Weizenecker, J., Markov, D. E., Aerts, H. C. J., Boeve, H., Borgert, J., & Kuhn, M. (2011). MPI cell tracking: what can we learn from MRI? *Medical Imaging 2011: Biomedical Applications in Molecular, Structural, and Functional Imaging*, 7965(March 2011), 79650Z. <https://doi.org/10.1117/12.879844>
147. Panagiotopoulos, N., Duschka, R. L., Ahlborg, M., Bringout, G., Debbeler, C., Graeser, M., Kaethner, C., Lüdtke-Buzug, K., Medimagh, H., Stelzner, J., Buzug, T. M., Barkhausen, J., Vogt, F. M., & Haegele, J. (2015). Magnetic particle imaging: current developments and future directions. *International journal of nanomedicine*, 10, 3097–3114. <https://doi.org/10.2147/IJN.S70488>
148. Tay, Z. W., Hensley, D. W., Vreeland, E. C., Zheng, B., & Conolly, S. M. (2017). The relaxation wall: experimental limits to improving MPI spatial resolution by increasing nanoparticle core

size. *Biomedical Physics & Engineering Express*, 3(3), 035003. <https://doi.org/10.1088/2057-1976/aa6ab6>

149. Dulińska-Litewka, J., Łazarczyk, A., Hałubiec, P., Szafranski, O., Karnas, K., & Karewicz, A. (2019). Superparamagnetic iron oxide nanoparticles-current and prospective medical applications. *Materials*, 12(4). <https://doi.org/10.3390/ma12040617>
150. Schütz, G., Lohrke, J., & Hütter, J. (2010.). Use of Resovist In Magnetic Particle Imaging. In *Magnetic Nanoparticles*, 32–36. [https://doi.org/10.1142/9789814324687\\_0004](https://doi.org/10.1142/9789814324687_0004)
151. Khandhar, A. P., Ferguson, R. M., Arami, H., & Krishnan, K. M. (2013). Monodisperse magnetite nanoparticle tracers for in vivo magnetic particle imaging. *Biomaterials*, 34(15), 3837–3845. <https://doi.org/10.1016/j.biomaterials.2013.01.087>
152. Grüttner, A., Kowalski, F., Fidler, M., Steinke, F., Westphal, & Teller, H. (2018). Nanoflower particles: A new tracer for mpi, physical characterization and initial in vitro toxicity studies. *International Workshio on Magnetic Particle Imaging*, 17-18.
153. Vogel, P., Kampf, T., Rückert, M. A., Grüttner, C., Kowalski, A., Teller, H., & Behr, V. C. (2021). Synomag®: The new high-performance tracer for magnetic particle imaging. *International Journal on Magnetic Particle Imaging*, 7(1). <https://doi.org/10.18416/IJMPI.2021.2103003>
154. Antonelli, A., Szwargulski, P., Scarpa, E. S., Thieben, F., Cordula, G., Ambrosi, G., Guidi, L., Ludewig, P., Knopp, T., & Magnani, M. (2020). Development of long circulating magnetic particle imaging tracers: use of novel magnetic nanoparticles and entrapment into human erythrocytes. *Nanomedicine (London, England)*, 15(8), 739–753. <https://doi.org/10.2217/nmm-2019-0449>
155. Gevaert, J. J., Fink, C., Dikeakos, J., Dekaban, G. A., Foster, P. J. (2021). Magnetic Particle Imaging is a sensitive *in vivo* imaging modality for the quantification of dendritic cell migration. *BioRxiv*, <https://doi.org/10.1101/2021.09.22.461401>
156. Paysen, H., Loewa, N., Stach, A., Wells, J., Kosch, O., Twamley, S., Makowski, M. R., Schaeffter, T., Ludwig, A., & Wiekhorst, F. (2020). Cellular uptake of magnetic nanoparticles imaged and quantified by magnetic particle imaging. *Scientific reports*, 10(1), 1922. <https://doi.org/10.1038/s41598-020-58853-3>
157. Zheng, B., Vazin, T., Goodwill, P. W., Conway, A., Verma, A., Saritas, E. U., Schaffer, D., & Conolly, S. M. (2015). Magnetic Particle Imaging tracks the long-term fate of in vivo neural cell implants with high image contrast. *Scientific reports*, 5, 14055. <https://doi.org/10.1038/srep14055>
158. Liu, S., Chiu-Lam, A., Rivera-Rodriguez, A., DeGroff, R., Savliwala, S., Sarna, N., & Rinaldi-Ramos, C. M. (2021). Long circulating tracer tailored for magnetic particle imaging. *Nanotheranostics*, 5(3), 348–361. <https://doi.org/10.7150/ntno.58548>

159. Song, G., Chen, M., Zhang, Y., Cui, L., Qu, H., Zheng, X., Wintermark, M., Liu, Z., & Rao, J. (2018). Janus Iron Oxides @ Semiconducting Polymer Nanoparticle Tracer for Cell Tracking by Magnetic Particle Imaging. *Nano letters*, *18*(1), 182–189. <https://doi.org/10.1021/acs.nanolett.7b03829>
160. Tay, Z. M., Conolly, S. M. (2019). Order-of-magnitude resolution and SNR improvement using positive feedback MNP chains in magnetic particle imaging. *World Molecular Imaging Congress*.
161. Tay, Z. W., Savliwala, S., Hensley, D. W., Fung, K. L. B., Colson, C., Fellows, B. D., Zhou, X., Huynh, Q., Lu, Y., Zheng, B., Chandrasekharan, P., Rivera-Jimenez, S. M., Rinaldi-Ramos, C. M., & Conolly, S. M. (2021). Superferromagnetic Nanoparticles Enable Order-of-Magnitude Resolution & Sensitivity Gain in Magnetic Particle Imaging. *Small Methods*, 2100796. <https://doi.org/https://doi.org/10.1002/smt.202100796>
162. Rahmer, J., Gleich, B., Weizenecker, J., & Borgert, J. (2010). 3D real-time magnetic particle imaging of cerebral blood flow in living mice. In *Proceedings of the International Society for Magnetic Resonance in Medicine*, *18*, 714.
163. Ludewig, P., Gdaniec, N., Sedlacik, J., Forkert, N. D., Szwargulski, P., Graeser, M., Adam, G., Kaul, M. G., Krishnan, K. M., Ferguson, R. M., Khandhar, A. P., Walczak, P., Fiehler, J., Thomalla, G., Gerloff, C., Knopp, T., & Magnus, T. (2017). Magnetic Particle Imaging for Real-Time Perfusion Imaging in Acute Stroke. *American Chemical Society Nano*, *11*(10), 10480–10488. <https://doi.org/10.1021/acs.nano.7b05784>
164. Sehl, O. C., Makela, A. V., Hamilton, A. M., & Foster, P. J. (2019). Trimodal Cell Tracking In Vivo: Combining Iron- and Fluorine-Based Magnetic Resonance Imaging with Magnetic Particle Imaging to Monitor the Delivery of Mesenchymal Stem Cells and the Ensuing Inflammation. *Tomography (Ann Arbor, Mich.)*, *5*(4), 367–376. <https://doi.org/10.18383/j.tom.2019.00020>
165. Mangarova, D. B., Brangsch, J., Mohtashamdolatshahi, A., Kosch, O., Paysen, H., Wiekhorst, F., Klopffleisch, R., Buchholz, R., Karst, U., Taupitz, M., Schnorr, J., Hamm, B., & Makowski, M. R. (2020). Ex vivo magnetic particle imaging of vascular inflammation in abdominal aortic aneurysm in a murine model. *Scientific reports*, *10*(1), 12410. <https://doi.org/10.1038/s41598-020-69299-y>
166. Melo, K., P. (2020). Detection and Quantification of Cells using Magnetic Particle Imaging and Magnetic Microspheres. *Electronic Thesis and Dissertation Repository*, 7509. <https://ir.lib.uwo.ca/etd/7509>
167. Zheng, B., von See, M. P., Yu, E., Gunel, B., Lu, K., Vazin, T., Schaffer, D. V., Goodwill, P. W., & Conolly, S. M. (2016). Quantitative Magnetic Particle Imaging Monitors the Transplantation, Biodistribution, and Clearance of Stem Cells In Vivo. *Theranostics*, *6*(3), 291–301. <https://doi.org/10.7150/thno.13728>
168. Nejadnik, H., Pandit, P., Lenkov, O., Lahiji, A. P., Yerneni, K., & Daldrup-Link, H. E. (2019). Ferumoxytol Can Be Used for Quantitative Magnetic Particle Imaging of Transplanted Stem Cells. *Molecular imaging and biology*, *21*(3), 465–472. <https://doi.org/10.1007/s11307-018-1276-x>

169. Lemaster, J. E., Chen, F., Kim, T., Hariri, A., & Jokerst, J. V. (2018). Development of a Trimodal Contrast Agent for Acoustic and Magnetic Particle Imaging of Stem Cells. *American Chemical Society: applied nano materials*, 1(3), 1321–1331. <https://doi.org/10.1021/acsnm.8b00063>
170. Wang, P., Goodwill, P. W., Pandit, P., Gaudet, J., Ross, A., Wang, J., Yu, E., Hensley, D. W., Doyle, T. C., Contag, C. H., Conolly, S., & Moore, A. (2018). Magnetic particle imaging of islet transplantation in the liver and under the kidney capsule in mouse models. *Quantitative imaging in medicine and surgery*, 8(2), 114–122. <https://doi.org/10.21037/qims.2018.02.06>
171. Hayat, H., Sun, A., Hayat, H., Liu, S., Talebloo, N., Pinger, C., Bishop, J. O., Gudi, M., Dwan, B. F., Ma, X., Zhao, Y., Moore, A., & Wang, P. (2021). Artificial Intelligence Analysis of Magnetic Particle Imaging for Islet Transplantation in a Mouse Model. *Molecular imaging and biology*, 23(1), 18–29. <https://doi.org/10.1007/s11307-020-01533-5>
172. Rivera-Rodriguez, A., Hoang-Minh, L. B., Chiu-Lam, A., Sarna, N., Marrero-Morales, L., Mitchell, D. A., & Rinaldi-Ramos, C. M. (2021). Tracking adoptive T cell immunotherapy using magnetic particle imaging. *Nanotheranostics*, 5(4), 431–444. <https://doi.org/10.7150/ntno.55165>
173. Makela, A. V., Gaudet, J. M., Schott, M. A., Sehl, O. C., Contag, C. H., & Foster, P. J. (2020). Magnetic Particle Imaging of Macrophages Associated with Cancer: Filling the Voids Left by Iron-Based Magnetic Resonance Imaging. *Molecular imaging and biology*, 22(4), 958–968. <https://doi.org/10.1007/s11307-020-01473-0>
174. Knier, N. N., & Foster, P. J. (2021). Tracking cancer cells in the mouse brain with magnetic resonance imaging (MRI) and magnetic particle imaging (MPI). (2021). *International Society for Magnetic Resonance in Medicine*. <https://www.ismrm.org/21/program-files/TeaserSlides/TeasersPresentations/1213-Teaser.html>
175. Sehl, O. C., Foster, P. J. (2021). The sensitivity of magnetic particle imaging and fluorine-19 magnetic resonance imaging for cell tracking. *BioRxiv*, <https://doi.org/10.1101/2021.08.31.458286>
176. Makela, A. V., Schott, M. A., Sehl, O. C., Gevaert, J. J., Foster, P. J., Contag, C. H. (2021). Tracking the fates of iron-labeled tumor cells in vivo using Magnetic Particle Imaging. *BioRxiv*. <https://doi.org/10.1101/2021.10.06.463387>.
177. Ferguson, R. M., Khandhar, A. P., Kemp, S. J., Arami, H., Saritas, E. U., Croft, L. R., Konkle, J., Goodwill, P. W., Halkola, A., Rahmer, J., Borgert, J., Conolly, S. M., & Krishnan, K. M. (2015). Magnetic Particle Imaging With Tailored Iron Oxide Nanoparticle Tracers. *IEEE Transactions on Medical Imaging*, 34(5), 1077–1084. <https://doi.org/10.1109/TMI.2014.2375065>

178. Shapiro, E. M., Skrtic, S., & Koretsky, A. P. (2005). Sizing it up: cellular MRI using micron-sized iron oxide particles. *Magnetic resonance in medicine*, 53(2), 329–338. <https://doi.org/10.1002/mrm.20342>
179. Parkins, K. M., Melo, K. P., Ronald, J. A., & Foster, P. J. (2020). Visualizing tumour self-homing with magnetic particle imaging. *BioRxiv*. <https://doi.org/10.1101/2020.02.17.953232>
180. Melo, K. P., Makela, A. V, Hamilton, A. M., & Foster, P. J. (2020). Development of Magnetic Particle Imaging (MPI) for Cell Tracking and Detection. *BioRxiv*. <https://doi.org/10.1101/2020.07.12.197780>
181. Youn, H., & Chung, J.-K. (2013). Reporter Gene Imaging. *American Journal of Roentgenology*, 201(2), W206–W214. <https://doi.org/10.2214/AJR.13.10555>
182. Serganova, I., & Blasberg, R. G. (2019). Molecular Imaging with Reporter Genes: Has Its Promise Been Delivered? *Journal of Nuclear Medicine*, 60(12), 1665 LP – 1681. <https://doi.org/10.2967/jnumed.118.220004>
183. Moriya, T., Yamaoka, T., Wakayama, Y., Ayukawa, S., Zhang, Z., Yamamura, M., Wakao, S., & Kiga, D. (2019). Comparison between Effects of Retroactivity and Resource Competition upon Change in Downstream Reporter Genes of Synthetic Genetic Circuits. *Life (Basel, Switzerland)*, 9(1), 30. <https://doi.org/10.3390/life9010030>
184. Ashmore-Harris, C., Iafrate, M., Saleem, A., & Fruhwirth, G. O. (2020). Non-invasive Reporter Gene Imaging of Cell Therapies, including T Cells and Stem Cells. *Molecular Therapy*, 28(6), 1392–1416. <https://doi.org/10.1016/j.ymthe.2020.03.016>
185. Xia, X., Ayala, M., Thiede, B. R., & Zhang, S. C. (2008). In vitro-and in vivo-induced transgene expression in human embryonic stem cells and derivatives. *Stem Cells*, 26(2), 525-533.
186. Serganova, I., Ponomarev, V., & Blasberg, R. (2007). Human reporter genes: potential use in clinical studies. *Nuclear medicine and biology*, 34(7), 791–807. <https://doi.org/10.1016/j.nucmedbio.2007.05.009>
187. Nyström, N. N., Yip, L. C. M., Carson, J. J. L., Scholl, T. J., & Ronald, J. A. (2019). Development of a Human Photoacoustic Imaging Reporter Gene Using the Clinical Dye Indocyanine Green. *Radiology: Imaging Cancer*, 1(2), e190035. <https://doi.org/10.1148/rycan.2019190035>
188. Jacobs, A., Voges, J., Reszka, R., Lercher, M., Gossmann, A., Kracht, L., Kaestle, C., Wagner, R., Wienhard, K., & Heiss, W. D. (2001). Positron-emission tomography of vector-mediated gene expression in gene therapy for gliomas. *Lancet (London, England)*, 358(9283), 727–729. [https://doi.org/10.1016/s0140-6736\(01\)05904-9](https://doi.org/10.1016/s0140-6736(01)05904-9)
189. Keu, K. V., Witney, T. H., Yaghoubi, S., Rosenberg, J., Kurien, A., Magnusson, R., Williams, J., Habte, F., Wagner, J. R., Forman, S., Brown, C., Allen-Auerbach, M., Czernin, J., Tang, W., Jensen, M. C., Badie, B., & Gambhir, S. S. (2017). Reporter gene imaging of targeted T cell immunotherapy in recurrent glioma. *Science translational medicine*, 9(373), eaag2196. <https://doi.org/10.1126/scitranslmed.aag2196>

190. Sadikot, R. T., & Blackwell, T. S. (2005). Bioluminescence imaging. *Proceedings of the American Thoracic Society*, 2(6), 537–512. <https://doi.org/10.1513/pats.200507-067DS>
191. Welsh, D. K., & Noguchi, T. (2012). Cellular bioluminescence imaging. *Cold Spring Harbor protocols*, 2012(8), pdb.top070607. <https://doi.org/10.1101/pdb.top070607>
192. Yao, Z., Zhang, B. S., & Prescher, J. A. (2018). Advances in bioluminescence imaging: new probes from old recipes. *Current opinion in chemical biology*, 45, 148–156. <https://doi.org/10.1016/j.cbpa.2018.05.009>
193. Close, D. M., Xu, T., Sayler, G. S., & Ripp, S. (2011). In vivo bioluminescent imaging (BLI): noninvasive visualization and interrogation of biological processes in living animals. *Sensors (Basel, Switzerland)*, 11(1), 180–206. <https://doi.org/10.3390/s110100180>
194. Martini, S., & Haddock, S. H. D. (2017). Quantification of bioluminescence from the surface to the deep sea demonstrates its predominance as an ecological trait. *Scientific Reports*, 7(1), 45750. <https://doi.org/10.1038/srep45750>
195. Haddock, S. H. D., Moline, M. A., & Case, J. F. (2010). Bioluminescence in the Sea. *Annual Review of Marine Science*, 2(1), 443–493. <https://doi.org/10.1146/annurev-marine-120308-081028>
196. Widder, E. A. (1999). Bioluminescence. In S. N. Archer, M. B. A. Djamgoz, E. R. Loew, J. C. Partridge, & S. Vallerga (Eds.), *Adaptive Mechanisms in the Ecology of Vision* (pp. 555–581). Springer Netherlands. [https://doi.org/10.1007/978-94-017-0619-3\\_19](https://doi.org/10.1007/978-94-017-0619-3_19)
197. Buck, J. B. (1978) Chapter 13: Functions and evolutions of bioluminescence. In: Herring, P. J. (Ed.) *Bioluminescence in Action*. Academic Press
198. Tett, P. B., & Kelly, M. G. (1973). Marine bioluminescence. *Oceanography and Marine Biology: An Annual Review*, 11, 89-173.
199. Young, R. E. (1983). Oceanic bioluminescence: an overview of general functions. *Bulletin of Marine Science*, 33(4), 829-845.
200. Hastings J. W. (1996). Chemistries and colors of bioluminescent reactions: a review. *Gene*, 173(1 Spec No), 5–11. [https://doi.org/10.1016/0378-1119\(95\)00676-1](https://doi.org/10.1016/0378-1119(95)00676-1)
201. Zambito, G., Chawda, C., & Mezzanotte, L. (2021). Emerging tools for bioluminescence imaging. *Current Opinion in Chemical Biology*, 63, 86–94. <https://doi.org/10.1016/j.cbpa.2021.02.005>
202. Lyons, S. K. (2011). Bioluminescence Imaging. In M. Schwab (Ed.), *Encyclopedia of Cancer* (pp. 405–408). Springer (Berlin Heidelberg). [https://doi.org/10.1007/978-3-642-16483-5\\_640](https://doi.org/10.1007/978-3-642-16483-5_640)



203. Mezzanotte, L., van 't Root, M., Karatas, H., Goun, E. A., & Löwik, C. W. G. M. (2017). In Vivo Molecular Bioluminescence Imaging: New Tools and Applications. *Trends in Biotechnology*, 35(7), 640–652. <https://doi.org/https://doi.org/10.1016/j.tibtech.2017.03.012>
204. de Wet, J. R., Wood, K. V., Helinski, D. R., & DeLuca, M. (1985). Cloning of firefly luciferase cDNA and the expression of active luciferase in *Escherichia coli*. *Proceedings of the National Academy of Sciences of the United States of America*, 82(23), 7870–7873. <https://doi.org/10.1073/pnas.82.23.7870>
205. Nguyen, V. T., Morange, M., & Bensaude, O. (1988). Firefly luciferase luminescence assays using scintillation counters for quantitation in transfected mammalian cells. *Analytical biochemistry*, 171(2), 404–408. [https://doi.org/10.1016/0003-2697\(88\)90505-2](https://doi.org/10.1016/0003-2697(88)90505-2)
206. Matthews, J. C., Hori, K., & Cormier, M. J. (1977). Purification and properties of *Renilla reniformis* luciferase. *Biochemistry*, 16(1), 85–91. <https://doi.org/10.1021/bi00620a014>
207. Kimura, T., Hiraoka, K., Kasahara, N., & Logg, C. R. (2010). Optimization of enzyme-substrate pairing for bioluminescence imaging of gene transfer using *Renilla* and *Gaussia* luciferases. *The journal of gene medicine*, 12(6), 528–537. <https://doi.org/10.1002/jgm.1463>
208. Zhao, H., Doyle, T. C., Wong, R. J., Cao, Y., Stevenson, D. K., Piwnicka-Worms, D., & Contag, C. H. (2004). Characterization of coelenterazine analogs for measurements of *renilla* luciferase activity in live cells and living animals. *Molecular Imaging*, 3(1), 43–54. <https://doi.org/10.1162/153535004773861714>
209. Amaral, D. T., Oliveira, G., Silva, J. R., & Viviani, V. R. (2016). A new orange emitting luciferase from the Southern-Amazon *Pyrophorus angustus* (Coleoptera: Elateridae) click-beetle: structure and bioluminescence color relationship, evolutionary and ecological considerations. *Photochemical & photobiological sciences : Official journal of the European Photochemistry Association and the European Society for Photobiology*, 15(9), 1148–1154. <https://doi.org/10.1039/c6pp00165c>
210. Chang, M., Anttonen, K. P., Cirillo, S. L., Francis, K. P., & Cirillo, J. D. (2014). Real-time bioluminescence imaging of mixed mycobacterial infections. *PloS one*, 9(9), e108341. <https://doi.org/10.1371/journal.pone.0108341>
211. Wood, K. V., Lam, Y. A., & McElroy, W. D. (1989). Introduction to beetle luciferases and their applications. *Journal of bioluminescence and chemiluminescence*, 4(1), 289–301. <https://doi.org/10.1002/bio.1170040141>
212. Kendall, J. M., & Badminton, M. N. (1998). *Aequorea victoria* bioluminescence moves into an exciting new era. *Trends in Biotechnology*, 16(5), 216–224. [https://doi.org/https://doi.org/10.1016/S0167-7799\(98\)01184-6](https://doi.org/https://doi.org/10.1016/S0167-7799(98)01184-6)
213. Grinstead, K. M., Rowe, L., Ensor, C. M., Joel, S., Daftarian, P., Dikici, E., Zingg, J.-M., & Daunert, S. (2016). Red-Shifted *Aequorin* Variants Incorporating Non-Canonical Amino Acids: Applications in In Vivo Imaging. *PLOS ONE*, 11(7), e0158579. <https://doi.org/10.1371/journal.pone.0158579>

214. Roura, S., Gálvez-Montón, C., & Bayes-Genis, A. (2013). Bioluminescence imaging: a shining future for cardiac regeneration. *Journal of cellular and molecular medicine*, 17(6), 693–703. <https://doi.org/10.1111/jcmm.12018>
215. Bourgois, J. J., Sluse, F. E., Baguet, F., & Mallefet, J. (2001). Kinetics of light emission and oxygen consumption by bioluminescent bacteria. *Journal of bioenergetics and biomembranes*, 33(4), 353–363. <https://doi.org/10.1023/a:1010615508916>
216. Esimbekova, E. N., Torgashina, I. G., & Kratasyuk, V. A. (2009). Comparative study of immobilized and soluble NADH:FMN-oxidoreductase-luciferase coupled enzyme system. *Biochemistry. Biokhimiia*, 74(6), 695–700. <https://doi.org/10.1134/s0006297909060157>
217. Foucault, M. L., Thomas, L., Goussard, S., Branchini, B. R., & Grillot-Courvalin, C. (2010). In vivo bioluminescence imaging for the study of intestinal colonization by *Escherichia coli* in mice. *Applied and environmental microbiology*, 76(1), 264–274. <https://doi.org/10.1128/AEM.01686-09>
218. Huang, N. F., Okogbaa, J., Babakhanyan, A., & Cooke, J. P. (2012). Bioluminescence imaging of stem cell-based therapeutics for vascular regeneration. *Theranostics*, 2(4), 346–354. <https://doi.org/10.7150/thno.3694>
219. Duda, J., Karimi, M., Negrin, R. S., & Contag, C. H. (2007). Methods for imaging cell fates in hematopoiesis. *Methods in molecular medicine*, 134, 17–34. [https://doi.org/10.1007/978-1-59745-223-6\\_2](https://doi.org/10.1007/978-1-59745-223-6_2)
220. Contag, C. H., & Ross, B. D. (2002). It's not just about anatomy: in vivo bioluminescence imaging as an eyepiece into biology. *Journal of magnetic resonance imaging*, 16(4), 378–387. <https://doi.org/10.1002/jmri.10178>
221. McCaffrey, A., Kay, M. A., & Contag, C. H. (2003). Advancing molecular therapies through in vivo bioluminescent imaging. *Molecular imaging*, 2(2), 75–86. <https://doi.org/10.1162/153535003322331966>
222. Xie, X., Cao, F., Sheikh, A. Y., Li, Z., Connolly, A. J., Pei, X., Li, R. K., Robbins, R. C., & Wu, J. C. (2007). Genetic modification of embryonic stem cells with VEGF enhances cell survival and improves cardiac function. *Cloning and stem cells*, 9(4), 549–563. <https://doi.org/10.1089/clo.2007.0032>
223. Wang, J., Najjar, A., Zhang, S., Rabinovich, B., Willerson, J. T., Gelovani, J. G., & Yeh, E. T. (2012). Molecular imaging of mesenchymal stem cell: mechanistic insight into cardiac repair after experimental myocardial infarction. *Circulation. Cardiovascular imaging*, 5(1), 94–101. <https://doi.org/10.1161/CIRCIMAGING.111.966424>
224. Vandeputte, C., Reumers, V., Aelvoet, S. A., Thiry, I., De Swaef, S., Van den Haute, C., Pascual-Brazo, J., Farr, T. D., Vande Velde, G., Hoehn, M., Himmelreich, U., Van Laere, K., Debysers, Z., Gijssbers, R., & Baekelandt, V. (2014). Bioluminescence imaging of stroke-induced

endogenous neural stem cell response. *Neurobiology of disease*, *69*, 144–155.  
<https://doi.org/10.1016/j.nbd.2014.05.014>

225. Rogall, R., Rabenstein, M., Vay, S., Bach, A., Pikhovych, A., Baermann, J., Hoehn, M., Couillard-Despres, S., Fink, G. R., Schroeter, M., & Rueger, M. A. (2018). Bioluminescence imaging visualizes osteopontin-induced neurogenesis and neuroblast migration in the mouse brain after stroke. *Stem cell research & therapy*, *9*(1), 182. <https://doi.org/10.1186/s13287-018-0927-9>
226. Wang, H., Cao, F., De, A., Cao, Y., Contag, C., Gambhir, S. S., Wu, J. C., & Chen, X. (2009). Trafficking mesenchymal stem cell engraftment and differentiation in tumor-bearing mice by bioluminescence imaging. *Stem cells (Dayton, Ohio)*, *27*(7), 1548–1558.  
<https://doi.org/10.1002/stem.81>
227. Tanaka, M., Swijnenburg, R. J., Gunawan, F., Cao, Y. A., Yang, Y., Caffarelli, A. D., de Bruin, J. L., Contag, C. H., & Robbins, R. C. (2005). In vivo visualization of cardiac allograft rejection and trafficking passenger leukocytes using bioluminescence imaging. *Circulation*, *112*(9 Suppl), I105–I110. <https://doi.org/10.1161/CIRCULATIONAHA.104.524777>
228. Perez, C., Jukica, A., Listopad, J. J., Anders, K., Köhl, A. A., Loddenkemper, C., Blankenstein, T., & Charo, J. (2015). Permissive expansion and homing of adoptively transferred T cells in tumor-bearing hosts. *International journal of cancer*, *137*(2), 359–371.  
<https://doi.org/10.1002/ijc.29401>
229. Zhu, L., Li, X. J., Kalimuthu, S., Gangadaran, P., Lee, H. W., Oh, J. M., Baek, S. H., Jeong, S. Y., Lee, S. W., Lee, J., & Ahn, B. C. (2017). Natural Killer Cell (NK-92MI)-Based Therapy for Pulmonary Metastasis of Anaplastic Thyroid Cancer in a Nude Mouse Model. *Frontiers in immunology*, *8*, 816. <https://doi.org/10.3389/fimmu.2017.00816>
230. Knorr, D. A., Bock, A., Brentjens, R. J., & Kaufman, D. S. (2013). Engineered human embryonic stem cell-derived lymphocytes to study in vivo trafficking and immunotherapy. *Stem cells and development*, *22*(13), 1861–1869. <https://doi.org/10.1089/scd.2012.0608>
231. Swift, B. E., Williams, B. A., Kosaka, Y., Wang, X. H., Medin, J. A., Viswanathan, S., Martinez-Lopez, J., & Keating, A. (2012). Natural killer cell lines preferentially kill clonogenic multiple myeloma cells and decrease myeloma engraftment in a bioluminescent xenograft mouse model. *Haematologica*, *97*(7), 1020–1028. <https://doi.org/10.3324/haematol.2011.054254>
232. Lee, H. W., Yoon, S. Y., Singh, T. D., Choi, Y. J., Lee, H. J., Park, J. Y., Jeong, S. Y., Lee, S. W., Ha, J. H., Ahn, B. C., Jeon, Y. H., & Lee, J. (2015). Tracking of dendritic cell migration into lymph nodes using molecular imaging with sodium iodide symporter and enhanced firefly luciferase genes. *Scientific reports*, *5*, 9865. <https://doi.org/10.1038/srep09865>
233. Lee, H., Lee, H. W., La Lee, Y., Jeon, Y. H., Jeong, S. Y., Lee, S. W., Lee, J., & Ahn, B. C. (2018). Optimization of Dendritic Cell-Mediated Cytotoxic T-Cell Activation by Tracking of Dendritic Cell Migration Using Reporter Gene Imaging. *Molecular imaging and biology*, *20*(3), 398–406. <https://doi.org/10.1007/s11307-017-1127-1>
234. Alsawaftah, N., Farooq, A., Dhou, S., & Majdalawieh, A. F. (2021). Bioluminescence Imaging Applications in Cancer: A Comprehensive Review. *IEEE reviews in biomedical engineering*, *14*, 307–326. <https://doi.org/10.1109/RBME.2020.2995124>

235. Bu, L., Ma, X., Tu, Y., Shen, B., & Cheng, Z. (2013). Optical image-guided cancer therapy. *Current pharmaceutical biotechnology*, *14*(8), 723–732. <https://doi.org/10.2174/1389201014666131226112507>
236. Söling, A., & Rainov, N. G. (2003). Bioluminescence imaging in vivo - application to cancer research. *Expert opinion on biological therapy*, *3*(7), 1163–1172. <https://doi.org/10.1517/14712598.3.7.1163>
237. Wang, Y., Bai, C., Ruan, Y., Liu, M., Chu, Q., Qiu, L., Yang, C., & Li, B. (2019). Coordinative metabolism of glutamine carbon and nitrogen in proliferating cancer cells under hypoxia. *Nature communications*, *10*(1), 201. <https://doi.org/10.1038/s41467-018-08033-9>
238. Zhou, H., Luby-Phelps, K., Mickey, B. E., Habib, A. A., Mason, R. P., & Zhao, D. (2009). Dynamic near-infrared optical imaging of 2-deoxyglucose uptake by intracranial glioma of athymic mice. *PloS one*, *4*(11), e8051. <https://doi.org/10.1371/journal.pone.0008051>
239. Henkin, A. H., Cohen, A. S., Dubikovskaya, E. A., Park, H. M., Nikitin, G. F., Auzias, M. G., Kazantzis, M., Bertozzi, C. R., & Stahl, A. (2012). Real-time noninvasive imaging of fatty acid uptake in vivo. *American Chemical Society: chemical biology*, *7*(11), 1884–1891. <https://doi.org/10.1021/cb300194b>
240. Jang, C., Oh, S. F., Wada, S., Rowe, G. C., Liu, L., Chan, M. C., Rhee, J., Hoshino, A., Kim, B., Ibrahim, A., Baca, L. G., Kim, E., Ghosh, C. C., Parikh, S. M., Jiang, A., Chu, Q., Forman, D. E., Lecker, S. H., Krishnaiah, S., Rabinowitz, J. D., ... Arany, Z. (2016). A branched-chain amino acid metabolite drives vascular fatty acid transport and causes insulin resistance. *Nature medicine*, *22*(4), 421–426. <https://doi.org/10.1038/nm.4057>
241. Lynes, M. D., Leiria, L. O., Lundh, M., Bartelt, A., Shamsi, F., Huang, T. L., Takahashi, H., Hirshman, M. F., Schlein, C., Lee, A., Baer, L. A., May, F. J., Gao, F., Narain, N. R., Chen, E. Y., Kiebish, M. A., Cypess, A. M., Blüher, M., Goodyear, L. J., Hotamisligil, G. S., ... Tseng, Y. H. (2017). The cold-induced lipokine 12,13-diHOME promotes fatty acid transport into brown adipose tissue. *Nature medicine*, *23*(5), 631–637. <https://doi.org/10.1038/nm.4297>
242. Momcilovic, M., & Shackelford, D. B. (2018). Imaging Cancer Metabolism. *Biomolecules & therapeutics*, *26*(1), 81–92. <https://doi.org/10.4062/biomolther.2017.220>
243. Suchowski, K., Pöschinger, T., Rehemtulla, A., Stürzl, M., & Scheuer, W. (2017). Noninvasive Bioluminescence Imaging of AKT Kinase Activity in Subcutaneous and Orthotopic NSCLC Xenografts: Correlation of AKT Activity with Tumor Growth Kinetics. *Neoplasia (New York, N.Y.)*, *19*(4), 310–320. <https://doi.org/10.1016/j.neo.2017.02.005>
244. Coppola, J. M., Ross, B. D., & Rehemtulla, A. (2008). Noninvasive imaging of apoptosis and its application in cancer therapeutics. *Clinical cancer research : an official journal of the American Association for Cancer Research*, *14*(8), 2492–2501. <https://doi.org/10.1158/1078-0432.CCR-07-0782>

245. Scabini, M., Stellari, F., Cappella, P., Rizzitano, S., Texido, G., & Pesenti, E. (2011). In vivo imaging of early stage apoptosis by measuring real-time caspase-3/7 activation. *Apoptosis*, *16*(2), 198–207. <https://doi.org/10.1007/s10495-010-0553-1>
246. Safran, M., Kim, W. Y., O'Connell, F., Flippin, L., Günzler, V., Horner, J. W., DePinho, R. A., & Kaelin, W. G. (2006). Mouse model for noninvasive imaging of HIF prolyl hydroxylase activity: Assessment of an oral agent that stimulates erythropoietin production. *Proceedings of the National Academy of Sciences*, *103*(1), 105–110. <https://doi.org/10.1073/pnas.0509459103>
247. Iglesias, P., Fraga, M., & Costoya, J. A. (2013). Defining hypoxic microenvironments by non-invasive functional optical imaging. *European Journal of Cancer*, *49*(1), 264–271. <https://doi.org/10.1016/j.ejca.2012.06.001>
248. Van de Bittner, G. C., Dubikovskaya, E. A., Bertozzi, C. R., & Chang, C. J. (2010). In vivo imaging of hydrogen peroxide production in a murine tumor model with a chemoselective bioluminescent reporter. *Proceedings of the National Academy of Sciences*, *107*(50), 21316 LP – 21321. <https://doi.org/10.1073/pnas.1012864107>
249. Edwards, W. B., Akers, W. J., Ye, Y., Cheney, P. P., Bloch, S., Xu, B., Laforest, R., & Achilefu, S. (2009). Multimodal Imaging of Integrin Receptor-Positive Tumors by Bioluminescence, Fluorescence, Gamma Scintigraphy, and Single-Photon Emission Computed Tomography Using a Cyclic RGD Peptide Labeled with a Near-Infrared Fluorescent Dye and a Radionuclide. *Molecular Imaging*. <https://doi.org/10.2310/7290.2009.00014>
250. Zhao, H., Tian, X., He, L., Li, Y., Pu, W., Liu, Q., Tang, J., Wu, J., Cheng, X., Liu, Y., Zhou, Q., Tan, Z., Bai, F., Xu, F., Smart, N., & Zhou, B. (2018). Apj<sup>+</sup> Vessels Drive Tumor Growth and Represent a Tractable Therapeutic Target. *Cell Reports*, *25*(5), 12411254.e5. <https://doi.org/10.1016/j.celrep.2018.10.015>
251. Edinger, M., Sweeney, T. J., Tucker, A. A., Olomu, A. B., Negrin, R. S., & Contag, C. H. (1999). Noninvasive assessment of tumor cell proliferation in animal models. *Neoplasia (New York, N.Y.)*, *1*(4), 303–310. <https://doi.org/10.1038/sj.neo.7900048>
252. Kozlowski, J. M., Fidler, I. J., Campbell, D., Xu, Z. L., Kaighn, M. E., & Hart, I. R. (1984). Metastatic behavior of human tumor cell lines grown in the nude mouse. *Cancer research*, *44*(8), 3522–3529.
253. Sweeney, T. J., Mailänder, V., Tucker, A. A., Olomu, A. B., Zhang, W., Cao, Y. a., Negrin, R. S., & Contag, C. H. (1999). Visualizing the kinetics of tumor-cell clearance in living animals. *Proceedings of the National Academy of Sciences of the United States of America*, *96*(21), 12044–12049. <https://doi.org/10.1073/pnas.96.21.12044>
254. Bhang, H. E., Gabrielson, K. L., Laterra, J., Fisher, P. B., & Pomper, M. G. (2011). Tumor-specific imaging through progression elevated gene-3 promoter-driven gene expression. *Nature medicine*, *17*(1), 123–129. <https://doi.org/10.1038/nm.2269>
255. Stollfuss, J., Landvogt, N., Abenstein, M., Ziegler, S., Schwaiger, M., Senekowitsch-Schmidtke, R., & Wieder, H. (2015). Non-invasive imaging of implanted peritoneal carcinomatosis in mice using PET and bioluminescence imaging. *European Journal of Nuclear Medicine and Molecular Imaging: Research*, *5*(1), 44. <https://doi.org/10.1186/s13550-015-0125-z>

256. Enomoto, T., Kubota, H., Mori, K., Shimogawara, M., Yoshita, M., Ohmiya, Y., & Akiyama, H. (2018). Absolute bioluminescence imaging at the single-cell level with a light signal at the Attowatt level. *BioTechniques*, *64*(6), 270–274. <https://doi.org/10.2144/btn-2018-0043>
257. Kim, J.-B., Urban, K., Cochran, E., Lee, S., Ang, A., Rice, B., Bata, A., Campbell, K., Coffee, R., Gorodinsky, A., Lu, Z., Zhou, H., Kishimoto, T. K., & Lassota, P. (2010). Non-Invasive Detection of a Small Number of Bioluminescent Cancer Cells In Vivo. *PLoS ONE*, *5*(2), e9364. <https://doi.org/10.1371/journal.pone.0009364>
258. Zabala, M., Alzuguren, P., Benavides, C., Crettaz, J., Gonzalez-Aseguinolaza, G., Ortiz de Solorzano, C., Gonzalez-Aparicio, M., Kramer, M. G., Prieto, J., & Hernandez-Alcoceba, R. (2009). Evaluation of bioluminescent imaging for noninvasive monitoring of colorectal cancer progression in the liver and its response to immunogene therapy. *Molecular Cancer*, *8*(1), 2. <https://doi.org/10.1186/1476-4598-8-2>
259. Dickson, P. V., Hamner, B., Ng, C. Y., Hall, M. M., Zhou, J., Hargrove, P. W., McCarville, M. B., & Davidoff, A. M. (2007). In vivo bioluminescence imaging for early detection and monitoring of disease progression in a murine model of neuroblastoma. *Journal of pediatric surgery*, *42*(7), 1172–1179. <https://doi.org/10.1016/j.jpedsurg.2007.02.027>
260. Puaux, A.-L., Ong, L. C., Jin, Y., Teh, I., Hong, M., Chow, P. K. H., Golay, X., & Abastado, J.-P. (2011). A Comparison of Imaging Techniques to Monitor Tumor Growth and Cancer Progression in Living Animals. *International Journal of Molecular Imaging*, *2011*, 1–12. <https://doi.org/10.1155/2011/321538>
261. Wang, G., Cong, W., Shen, H., Qian, X., Henry, M., & Wang, Y. (2008). Overview of bioluminescence tomography--a new molecular imaging modality. *Frontiers in bioscience : a journal and virtual library*, *13*, 1281–1293. <https://doi.org/10.2741/2761>
262. Endo, M., & Ozawa, T. (2020). Advanced Bioluminescence System for In Vivo Imaging with Brighter and Red-Shifted Light Emission. *International Journal of Molecular Sciences*, *21*. <https://doi.org/10.3390/ijms21186538>
263. Kobayashi, H., Ogawa, M., Alford, R., Choyke, P. L., & Urano, Y. (2010). New Strategies for Fluorescent Probe Design in Medical Diagnostic Imaging. *Chemical Reviews*, *110*(5), 2620–2640. <https://doi.org/10.1021/cr900263j>
264. Kuchimaru, T., Iwano, S., Kiyama, M., Mitsumata, S., Kadonosono, T., Niwa, H., Maki, S., & Kizaka-Kondoh, S. (2016). A luciferin analogue generating near-infrared bioluminescence achieves highly sensitive deep-tissue imaging. *Nature Communications*, *7*(1), 11856. <https://doi.org/10.1038/ncomms11856>
265. Weissleder, R., & Ntziachristos, V. (2003). Shedding light onto live molecular targets. *Nature medicine*, *9*(1), 123–128. <https://doi.org/10.1038/nm0103-123>

266. Dawson, J. B., Barker, D. J., Ellis, D. J., Grassam, E., Cotterill, J. A., Fisher, G. W., & Feather, J. W. (1980). A theoretical and experimental study of light absorption and scattering by in vivo skin. *Physics in medicine and biology*, 25(4), 695–709. <https://doi.org/10.1088/0031-9155/25/4/008>
267. Hall, M. P., Woodroffe, C. C., Wood, M. G., Que, I., van't Root, M., Ridwan, Y., Shi, C., Kirkland, T. A., Encell, L. P., Wood, K. V., Löwik, C., & Mezzanotte, L. (2018). Click beetle luciferase mutant and near infrared naphthyl-luciferins for improved bioluminescence imaging. *Nature Communications*, 9(1), 132. <https://doi.org/10.1038/s41467-017-02542-9>
268. Nakayama, J., Saito, R., Hayashi, Y., Kitada, N., Tamaki, S., Han, Y., Semba, K., & Maki, S. A. (2020). High Sensitivity In Vivo Imaging of Cancer Metastasis Using a Near-Infrared Luciferin Analogue seMpai. *International journal of molecular sciences*, 21(21), 7896. <https://doi.org/10.3390/ijms21217896>
269. Saito-Moriya, R., Obata, R., & A. Maki, S. (2021). Near-Infrared Luciferin Analogs for In Vivo Optical Imaging. *Bioluminescence [Working Title]*. <https://doi.org/10.5772/intechopen.96760>
270. Hall, M. P., Unch, J., Binkowski, B. F., Valley, M. P., Butler, B. L., Wood, M. G., Otto, P., Zimmerman, K., Vidugiris, G., Machleidt, T., Robers, M. B., Benink, H. A., Eggers, C. T., Slater, M. R., Meisenheimer, P. L., Klaubert, D. H., Fan, F., Encell, L. P., & Wood, K. V. (2012). Engineered luciferase reporter from a deep sea shrimp utilizing a novel imidazopyrazinone substrate. *American Chemical Society: chemical biology*, 7(11), 1848–1857. <https://doi.org/10.1021/cb3002478>
271. Germain-Genevois, C., Garandeau, O., & Couillaud, F. (2016). Detection of Brain Tumors and Systemic Metastases Using NanoLuc and Fluc for Dual Reporter Imaging. *Molecular imaging and biology*, 18(1), 62–69. <https://doi.org/10.1007/s11307-015-0864-2>
272. Chu, J., Oh, Y., Sens, A., Ataie, N., Dana, H., Macklin, J. J., Laviv, T., Welf, E. S., Dean, K. M., Zhang, F., Kim, B. B., Tang, C. T., Hu, M., Baird, M. A., Davidson, M. W., Kay, M. A., Fiolka, R., Yasuda, R., Kim, D. S., Ng, H. L., ... Lin, M. Z. (2016). A bright cyan-excitable orange fluorescent protein facilitates dual-emission microscopy and enhances bioluminescence imaging in vivo. *Nature biotechnology*, 34(7), 760–767. <https://doi.org/10.1038/nbt.3550>
273. Iwano, S., Obata, R., Miura, C., Kiyama, M., Hama, K., Nakamura, M., ... & Niwa, H. (2013). Development of simple firefly luciferin analogs emitting blue, green, red, and near-infrared biological window light. *Tetrahedron*, 69(19), 3847–3856.
274. Iwano, S., Sugiyama, M., Hama, H., Watakabe, A., Hasegawa, N., Kuchimaru, T., Tanaka, K. Z., Takahashi, M., Ishida, Y., Hata, J., Shimozone, S., Namiki, K., Fukano, T., Kiyama, M., Okano, H., Kizaka-kondoh, S., Mchugh, T. J., Yamamori, T., Hioki, H., ... Miyawaki, A. (2018). *Moving Animals*. 939(February), 935–939.
275. Mofford, D. M., & Miller, S. C. (2015). Luciferins Behave Like Drugs. *American Chemical Society: Chemical Neuroscience*, 6(8), 1273–1275. <https://doi.org/10.1021/acschemneuro.5b00195>
276. Su, Y., Walker, J., Park, Y., Smith, T., Liu, L., Hall, M., Labanieh, L., Hurst, R., Wang, D., Encell, L., Kim, N., Zhang, F., Kay, M., Casey, K., Majzner, R., Cochran, J., Mackall, C., Kirkland, T., & Lin, M. (2020). Novel NanoLuc substrates enable bright two-population

bioluminescence imaging in animals. *Nature Methods*, 17, 1–9. <https://doi.org/10.1038/s41592-020-0889-6>

277. Liu, S., Nyström, N. N., Kelly, J. J., Hamilton, A. M., Fu, Y., & Ronald, J. A. (2021). Molecular Imaging Reveals a High Degree of Cross-Seeding of Spontaneous Metastases in a Novel Mouse Model of Synchronous Bilateral Breast Cancer. *Molecular Imaging and Biology*. <https://doi.org/10.1007/s11307-021-01630-z>
278. Zhong, C., Kayamori, K., Koide, S., Shinoda, D., Oshima, M., Nakajima-Takagi, Y., Nagai, Y., Mimura, N., Sakaida, E., Yamazaki, S., Iwano, S., Miyawaki, A., Ito, R., Tohyama, K., Yamaguchi, K., Furukawa, Y., Lennox, W., Sheedy, J., Weetall, M., & Iwama, A. (2020). Efficacy of the novel tubulin polymerization inhibitor PTC-028 for myelodysplastic syndrome. *Cancer science*, 111(12), 4336–4347. <https://doi.org/10.1111/cas.14684>
279. Bozec, D., Sattiraju, A., Bouras, A., Jesu Raj, J. G., Rivera, D., Huang, Y., Junqueira Alves, C., Tejero, R., Tsankova, N. M., Zou, H., Hadjipanayis, C., & Friedel, R. H. (2020). Akaluc bioluminescence offers superior sensitivity to track in vivo glioma expansion. *Neuro-Oncology Advances*, 2(1), 1–10. <https://doi.org/10.1093/noajnl/vdaa134>
280. Amadeo, F., Plagge, A., Chacko, A., Wilm, B., Hanson, V., Liptrott, N., Murray, P., & Taylor, A. (2021). Firefly luciferase offers superior performance to AkaLuc for tracking the fate of administered cell therapies. *European Journal of Nuclear Medicine and Molecular Imaging*. <https://doi.org/10.1007/s00259-021-05439-4>
281. Yeh, H. W., Wu, T., Chen, M., & Ai, H. W. (2019). Identification of Factors Complicating Bioluminescence Imaging. *Biochemistry*, 58(12), 1689–1697. <https://doi.org/10.1021/acs.biochem.8b01303>
282. Arami, H., Khandhar, A. P., Tomitaka, A., Yu, E., Goodwill, P. W., Conolly, S. M., & Krishnan, K. M. (2015). In vivo multimodal magnetic particle imaging (MPI) with tailored magneto/optical contrast agents. *Biomaterials*, 52(1), 251–261. <https://doi.org/10.1016/j.biomaterials.2015.02.040>
283. Arami, H., Teeman, E., Troksa, A., Bradshaw, H., Saatchi, K., Tomitaka, A., Gambhir, S. S., Hafeli, U., Liggitt, D., & Kannan, M. (2017). Tomographic Magnetic Particle Imaging of Cancer Targeted Nanoparticles. *Nanoscale*. 9(47), 18723–18730. <https://doi.org/10.1039/c7nr05502a>. Tomographic
284. Song, G., Zheng, X., Wang, Y., Xia, X., Chu, S., & Rao, J. (2019). A Magneto-Optical Nanoplatfrom for Multimodality Imaging of Tumors in Mice. *American Chemical Society: Nano*. <https://doi.org/10.1021/acsnano.9b01436>
285. Jung, K. O., Jo, H., Yu, J. H., Gambhir, S. S., & Pratz, G. (2018). Development and MPI tracking of novel hypoxia-targeted theranostic exosomes. *Biomaterials*, 177, 139–148. <https://doi.org/10.1016/j.biomaterials.2018.05.048>



## Chapter 2

This chapter will highlight all experiments conducted for this thesis. The data presented is in the form of an integrated paper.

### Abstract

Magnetic particle imaging (MPI) is an emerging technology used to directly visualize and quantify superparamagnetic iron oxide (SPIO) nanoparticles *in vivo*. Compared to the more conventional iron-based cellular MRI method, MPI provides positive contrast and quantification of cell number at initial implantation. Bioluminescence imaging (BLI) with the highly sensitive reporter gene Akaluc can provide complementary information on cell viability and thus, we explored combining these technologies to provide a more holistic view of cancer cell fate in mice. Murine breast cancer cells stably expressing Akaluc and TdTomato were labeled with an MPI tailored nanoparticle, Synomag-D, and injected into the mammary fat pad (MFP) of nude mice. BLI was performed on days 0, 6 and 13 and MPI was performed on days 1, 8 and 14. BLI signal in the MFP increased significantly from day 0 to day 13 as a result of tumour growth. MPI signal significantly decreased from day 1 to day 14 as a result of probe dilution in proliferating cancer cells. BLI signal significantly increased from day 0 to 13. Secondary metastases were detected with both modalities, although they were visualized in different locations throughout the body. Overall, Akaluc BLI complemented our MPI cell tracking technique, allowing for longitudinal measures of cell viability and highly sensitive detection of distant metastases. We predict this multimodal imaging approach will be useful in evaluating novel therapeutics and gaining a better understanding of the mechanisms contributing to metastasis.

## 2.1 Introduction

At least two thirds of cancer deaths can be attributed to metastasis in vital organs such as the brain, lungs or liver (1,2). Despite these staggering numbers and the significant amount of research devoted to this field, many of the biological mechanisms responsible for cancer metastasis remain unclear. As a result, the development of effective treatments is difficult and patient outcomes are variable (3). Preclinical animal models are valuable in optimizing and evaluating novel treatment strategies *in vivo*. They allow for longitudinal and dynamic studies to be carried out within an intact, living subject rather than at the cell or organ level. To enable monitoring cancer cells over time, imaging technologies have been used extensively in preclinical models to noninvasively visualize and quantify cell proliferation, migration and viability (4).

Cellular MRI is one of the most common techniques for *in vivo* cell tracking due to unrivaled soft tissue contrast and high spatial resolution. MRI cell tracking is typically done by labeling cells with superparamagnetic iron oxide particles (SPIOs) which cause a distortion in the magnetic field, resulting in a loss of signal or signal void (5-9) This signal void appears as a dark region within the image. By employing this technology, our group and others have previously demonstrated the ability to detect down to a single cell or particle in a variety of preclinical animal models (10-15). However, the dark signal voids generated by SPIOs, makes it difficult to discern cells from other naturally dark regions throughout the body such as blood or air. Within the magnetic field, the iron also causes a blooming effect such that the area of signal loss in the image appears larger than the cell itself (16,17). Importantly, this makes the quantification of iron-labeled cells difficult since the relationship between the signal detected *in vivo* and the number of SPIO-labeled cells injected is not linear (18-21). Therefore, an alternative imaging modality that provides positive contrast and can more readily quantify the number of SPIO particles and/or SPIO labeled cells would be highly valuable to the cell tracking field.

Magnetic particle imaging (MPI) is an emerging imaging technology that works by directly detecting iron nanoparticles and thus, may be a valuable tool for *in vivo* tracking and quantifying SPIO-labeled cells (22,23). In MPI, two electromagnets are positioned opposite each other, producing opposing magnetic fields. In the centre of the two magnets is a “field free region” (FFR) where there is a zero-

net magnetization. When this FFR passes over free or loaded SPIO, the magnetization of the particle flips, resulting in a positive signal. Since only SPIO can be detected with MPI and there is no endogenous SPIO in biological tissues, there is no background signal associated with MPI. This results in MPI having a relatively high specificity but reduced cellular resolution when compared to MRI. Furthermore, in MPI, the amount of SPIO present is linearly proportional to the amount of signal detected and allows for calculation of cell number if the concentration of SPIO per cell is known (21,24-28). Recent advancements in tracer development have quickly led to improved *in vivo* cell detection limits. Nanoparticles tailored specifically to MPI such as Synomag-D from Micromod Partikeltechnologie GmbH (29), have shown to have higher sensitivity and resolution than MPI using non-tailored particles (30). The highest reported sensitivity achieved by MPI to date is 200-250 SPIO-loaded cells (31,32). The best resolution reported is 150  $\mu\text{m}$  (33). While MPI overcomes many of the potential issues associated with cellular MRI, some important limitations still need to be considered. First, SPIOs can become diluted through cell division, which can result in a loss of signal over time and difficulties in quantification of cell number, particularly for highly proliferative cells (19) As in cellular MRI, SPIOs can be expelled from dead cells and taken up by non-transplanted cells such as macrophages, leading to false-positives in MPI (34). Finally, MPI will produce the same signal regardless of whether the SPIO-labeled cell is dead or alive, and thus, MPI and MRI are not feasible modalities to assess and visualize cell viability. (34).

Bioluminescence imaging (BLI) has been widely used for preclinical cancer studies, offering a relatively inexpensive tool to evaluate cell migration, proliferation, and viability (35-42). For BLI, a luciferase reporter gene is introduced into the host cell genome through viral or non-viral methods. The luciferase will react with an administered substrate and produce light as a product of oxidation, which gets collected by a cooled CCD camera. Compared to MPI, BLI requires stable reporter gene expression with each daughter cell receiving a copy or copies of the luciferase reporter gene upon division, and thus BLI does not suffer from label dilution over time (43-45). This makes BLI an advantageous imaging tool for longitudinal cancer studies since highly proliferative cells can be monitored over time. Importantly, the majority of luciferases require ATP and oxygen as cofactors in the enzymatic reaction, resulting in signal that is representative of live cells only. Unlike the autofluorescence that is commonly observed in fluorescence imaging, there is little endogenous bioluminescence in the body, giving BLI relatively high CNR (46). However, optical imaging is limited by depth of penetration since light is attenuated by biological tissue resulting in decreased signal at greater depths. As a result, BLI is primarily restricted to small animal imaging (35,47-50).

In recent years, developments in reporter gene systems have addressed some of the limitations of conventional BLI. Akalumine, a new substrate derived from D-Luciferin by replacing the aromatic structure with a benzothiazole moiety, has greatly minimized the depth effects typically associated with tissue attenuation observed in BLI. Akalumine is a BLI substrate that releases light in the Near Infrared Range (NIR) when catalyzed by Akaluc, which is less attenuated by biological tissues (51-53). Utilizing this system, researchers have demonstrated the ability to detect single Akaluc expressing HeLa cells trapped in the lungs of mice (53). Further, through the use of Akaluc BLI, Iwano et al., were even capable of detecting BLI signal in the brains of marmosets, providing evidence of greatly improved sensitivity (52). Even with these advancements however, BLI remains a pre-clinical imaging modality due to the high concentrations of substrate which would need to be administered in patients.

The combination of using two or more imaging systems, commonly referred to as multimodal imaging, provides a more complete picture of cancer cell fate *in vivo*. Multiple modalities can provide complementary information on a given disease state while overcoming some of the existing limitations of using a single imaging modality. The purpose of this study was to combine MPI and Akaluc BLI for high sensitivity cancer cell tracking in a murine model of triple negative breast cancer.

## 2.2 Materials and Methods

### 2.2.1 Cell Line Origins and Culture

4T1Br5 cells were generously provided by Dr. Patricia Steeg's lab. Cells are a derivative of 4T1 murine breast cancer cells, with preferential metastasis to the brain. The 4T1Br5 cells were maintained in T75cm<sup>2</sup> flasks with 10mL of Dulbecco's modified Eagle's medium (DMEM) containing 10% fetal bovine serum (FBS) and 1% antibiotics. Cells were grown under 37°C and 5% CO<sub>2</sub>. Passaging was conducted every 4 days, using 0.25% Trypsin-EDTA to unadhered cells from the flask.

### 2.2.2 Transduction of 4T1Br5 cells with TdTomato-Akaluc

4T1Br5 cells were transduced with lentivirus to express a construct consisting of a pEF1  $\alpha$  constitutive promoter driving both TdTomato and Akaluc. To evaluate whether the construct was successfully introduced into the 4T1Br5 cell line, the expression of tdTomato was measured through flow cytometry using a FACS Canto Cytometer. The expression of TdT was assessed at passage 3, 4, and 10

to evaluate construct stability. Reporter gene expression was further visualized using an epifluorescence microscope using an EVOS FL Auto Imaging System (Thermo Fisher Scientific).

### *2.2.3 Cell Characterization*

The relationship between cell number and BLI signal for transduced cells was evaluated by seeding cells on a 24 well plate in 500 $\mu$ L at the following cell counts:  $1 \times 10^6$ ,  $5 \times 10^5$ ,  $2.5 \times 10^5$ ,  $1.25 \times 10^5$  and  $6 \times 10^4$  cells. Prior to imaging, 5  $\mu$ L of Akalumine-HCl (30 mg/ml; TokeOni) was added directly to each well. Cells were immediately imaged on an IVIS Lumina XRMS In Vivo Imaging System (PerkinElmer) until maximum signal flux (Photons/second) was observed. This was done in 3 technical and biological replicates. Linear regression was used to compare BLI total signal (Photons/Second) vs. plated cell number.

### *2.2.4 Cell Labelling*

Cell labeling was performed with the SPIO, Synomag-D (Micromod Partikeltechnologie, GmbH, Germany). Synomag-D is a dextran coated MPI tailored nanoparticle that has a 30 nm nanoflower core and a 50 nm hydrodynamic diameter (10 mg/ml iron content). No surface functionalities were added. 4T1Br5 cells ( $10^5$ ) were seeded in a T75 flask and grown until 80% confluency was reached. Cells were washed with PBS and then added to a new T75 flask containing 5 mL of serum-free DMEM media (97%), 90  $\mu$ L Synomag-D (1.7%) (Micromod Partikeltechnologie, GmbH, Germany), 60  $\mu$ L of Protamine Sulphate (1.2%) (Thermofisher Scientific), and 20  $\mu$ L of Heparin (0.4%) (Thermofisher Scientific). After a 4hr incubation period at 37°C and 5% CO<sub>2</sub>, an additional 5mL of DMEM was added to the flask. Cells were incubated for a total of 24hrs and then washed with PBS prior to being used for studies.

To determine whether the cells were efficiently labeled with Synomag-D, a Perl's Prussian Blue (PPB) stain for iron was performed. Labeled cells were washed three times with PBS to remove any excess iron. Iron-labeled cells were imaged at 400X magnification on an EVOS FL Auto Imaging System (Thermo Fisher Scientific). To calculate labeling efficiency, the number of cells with visible encapsulated iron particles was divided by the total number of cells in a region. This was sampled at three fields of view for nine different slides.

### *2.2.5 Cell Viability*

To determine the effect of iron labeling on cell viability, labeled and unlabeled cells were stained with a 1/100 dilution of Zombie Violet (Fisher Scientific). The working concentration of this dye was

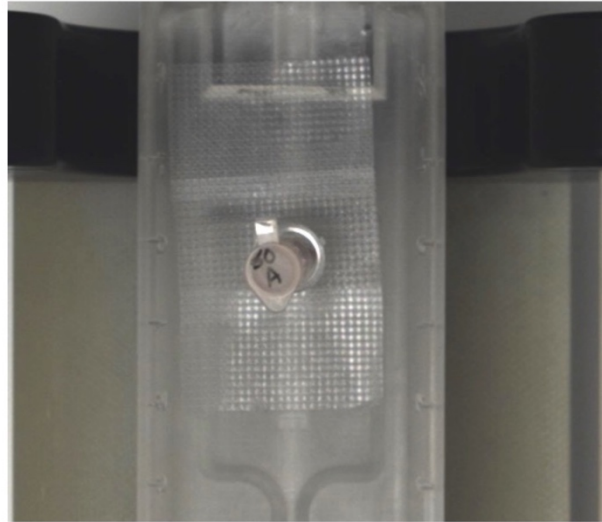
determined through titration. Cells were then evaluated using a FACS CANTO Flow Cytometer to measure fluorescence in the Zombie Violet channel (excitation nm; 450/50 nm bandpass filter). A “Dead Cell” control, was created via incubation at 56°C for 10 minutes prior to staining, killing approximately 20% of cells. Additionally, an unstained control was used to set the gating for the experiment.

### ***2.2.6 In Vitro BLI***

To determine the effect of iron labeling on BLI signal,  $4 \times 10^4$  labeled and unlabeled cells were added to a 24 well plate, along with a naïve untransduced, unlabeled population as a negative control. Next, 5  $\mu$ l of Akalumine-HCL (5 mM) was added to each well prior to imaging an IVIS Lumina XRMS In Vivo Imaging System (PerkinElmer). This was repeated on days 1,3,5 and 7 post iron labeling.

### ***2.2.7 General MPI Scan Setup and Protocol***

For *in vitro* experiments, an empty ELISA well was taped to the bed, in which PCR tubes containing the experimental samples were placed. For *in vivo* experiments, mice were placed in the headfirst prone position within the MPI bed. Legs were extended and taped down to position the primary tumor within the mammary fat pad away from the body. All scans were conducted under 1-2% isoflurane administered from a nose cone. A schematic of this setup can be seen in Figure 2.1 below

**Figure 2.1:****A.****B.****C.**

**Figure 2.1. Schematic of MPI set up.** All MPI experiments were conducted on the Momentum Scanner from Magnetic Insight seen in A. The *in vitro* set up can be seen in B. SPIO, or cell pellets labelled with SPIO were loaded into a PCR tube, and placed into an empty ELISA well. This well was taped onto the bed of the MPI. The *in vivo* set up can be seen in C. Mice were positioned in the prone position. Hind legs were extended backwards and taped to the side of the bed. An additional piece of tape was used around the abdomen to hold the mouse in place. Isoflurane was administered via nose cone by a tube running beneath the bed.

### 2.2.8 Characterization of Synomag-D

The sensitivity and resolution of Synomag-D were characterized using MPI relaxometry, and compared to the commonly used SPIO, Vivotrax (Magnetic Insight Inc). Three technical replicates of 1  $\mu\text{l}$  of Synomag-D were scanned separately with a full field of view (FOV) (12 cm). This was repeated for three technical replicates of Vivotrax. The sensitivity of both Synomag-D and Vivotrax was determined by the amplitude of the point spread function (PSF), while resolution was given by the full width half maximum (FWHM).

To evaluate the relationship between Synomag-D concentration and MPI signal, dilutions of Synomag-D (50  $\mu\text{g}/\mu\text{l}$ , 25  $\mu\text{g}/\mu\text{l}$ , 12.5  $\mu\text{g}/\mu\text{l}$ , 6.25  $\mu\text{g}/\mu\text{l}$ , 3.16  $\mu\text{g}/\mu\text{l}$ , 1.56  $\mu\text{g}/\mu\text{l}$ , 0.78  $\mu\text{g}/\mu\text{l}$ ) were scanned individually on MPI in triplicates using a full field of view (12 cm). ROIs were drawn based on the outline described in the “*Image Analysis*” section. A linear regression was done to correlate iron concentration to signal. This was conducted using a 3D high sensitivity multichannel isotropic scan (35 projections, 12 cm FOV). The slope of this calibration curve was used to quantify iron content from MPI images using the formula:

$$\text{Iron Content } (\mu\text{g}) = \frac{\text{Total MPI Signal (A.U.)}}{\text{Slope of Calibration Line}}$$

To determine the smallest mass of iron that can be reliably detected on MPI Serial dilutions of iron labelled cells were made with titres of  $1.024 \times 10^6$ ,  $5.12 \times 10^5$ ,  $2.56 \times 10^5$ ,  $1.28 \times 10^5$ ,  $6.40 \times 10^4$ ,  $3.20 \times 10^4$ ,  $1.60 \times 10^4$ ,  $8.00 \times 10^3$ ,  $4.00 \times 10^3$ ,  $2.00 \times 10^3$ ,  $1.00 \times 10^3$ ,  $5.00 \times 10^2$  in PCR tubes. Pellets were scanned using the 2D High sensitivity isotropic mode starting from the highest cell count. The positive signal detection threshold was set at an SNR of 5 which can be calculated by dividing the mean signal of the image by the standard deviation of the background signal. This follows the Rose Criterion for visible signal (54). Cell dilutions having a signal above the threshold (SNR >5), can be reliably detected with MPI, while cell dilutions below this signal threshold were considered undetectable. The last cell dilution that exceeded this threshold is said to be the “2D detection limit”. 3D high sensitivity (35 projection) scans were then acquired for dilutions beginning at the 2D detection limit and continuing to the lowest cell count ( $8.00 \times 10^3$ ,  $4.00 \times 10^3$ ,  $2.00 \times 10^3$ ,  $1.00 \times 10^3$ ,  $5.00 \times 10^2$ ). The 3D detection limit was the last iron dilution which produced a signal greater than the threshold (SNR > 5).



### 2.2.9 *In Vivo* BLI and MPI

4T1Br5 cells expressing TdTomato and Akaluc were cultured for one week prior to labeling with Synomag-D. One million cells suspended in 100 ul of PBS were injected into the 4<sup>th</sup> mammary fat pad of each mouse (n=4). BLI was performed on days 0, 6 and 13 following injection. Immediately prior to imaging, an intraperitoneal injection of 100 ul of Akalumine-HCl (5 mM) (Sigma Aldrich) was administered. Mice were anesthetized using 1-2% isoflurane and positioned supine in an IVIS Lumina XRMS In Vivo Imaging System (PerkinElmer). Regions of interest were placed over the primary tumours and images were acquired for up to 30 minutes until peak photon flux (p/s) was reached for each mouse. Once peak signal was reached, additional images were acquired with the lower half of the mouse covered with a black cloth to allow for visualization of secondary lesions.

MPI was performed on days 1, 8 and 14 post injection. A schematic for the *in vivo* experimental outline can be seen in Figure 2.2. Mice were anesthetized using 1-2% isoflurane and imaged for up to 40 minutes. Mouse food and bedding was removed for 12 hours prior to imaging to minimize any unwanted signal from the gut which can be caused by iron present in food or bedding. MPI scans were acquired in 3D mode with 35 projections and a full field of view (12 cm). Mice were placed in the MPI scanner headfirst in the prone position. Legs were extended and taped to the bed. MPI images were analyzed in VivoQuant (InVivo). ROI's were generated automatically for any signal greater than the set threshold (SNR >5). Quantification was done by comparing the MPI signal to the 3D Calibration line made earlier. A more in-depth description of the image analysis for both MPI and BLI is outlined in section 2.2.10.

Figure 2.2:

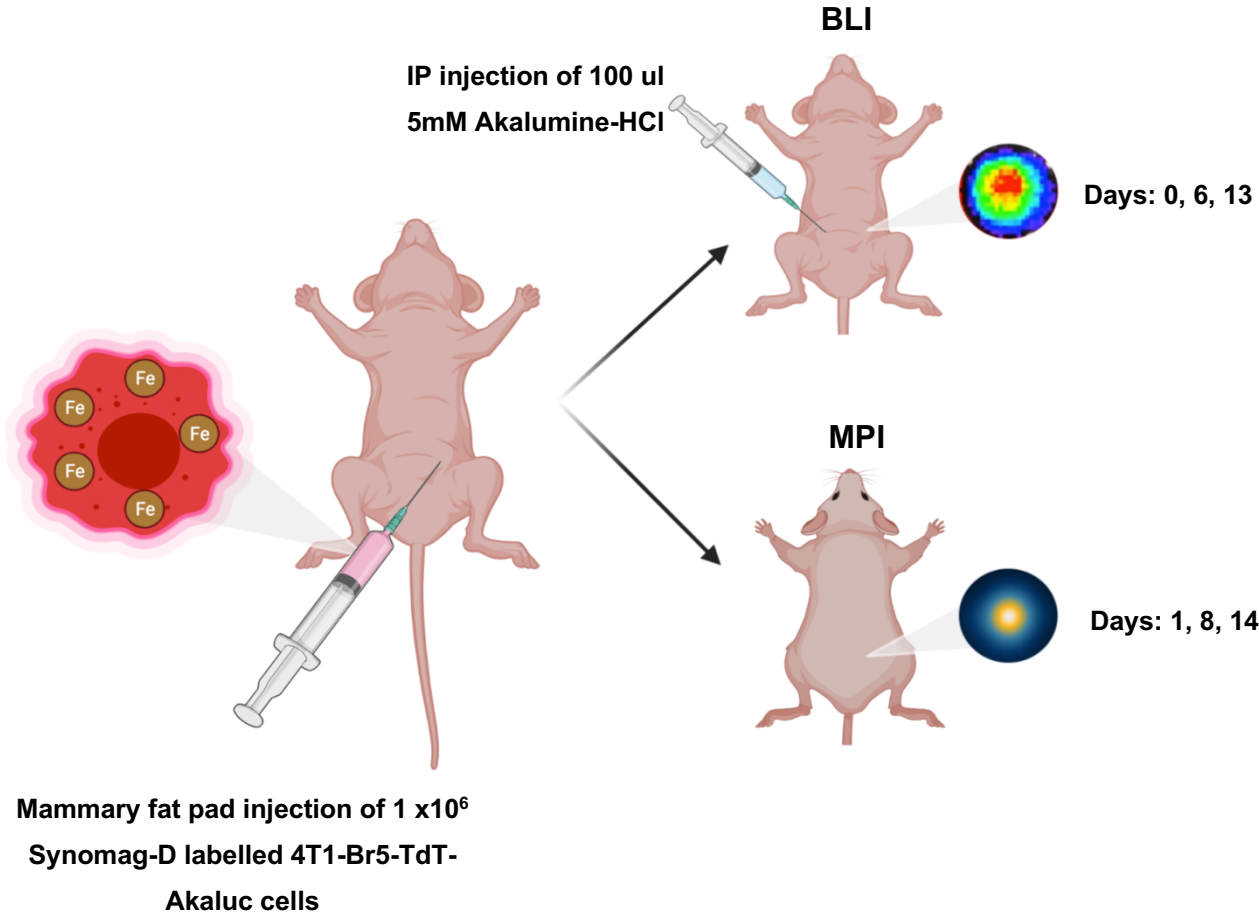


**Figure 2.2. Schematic of *in vivo* MPI and BLI experimental outline.** Mice were injected with One million dual labelled 4T1Br5 cells via the 4<sup>th</sup> mammary fat pad. Mice were imaged on BLI 0-, 6-, and 13-days post cell injection, following the administration of 100  $\mu$ l of 5mM Akalumine-HCl via intraperitoneal injection. Scans were done in supine position. MPI scans were conducted 1-, 8-, and 14-days post cell injection while mice were in the prone position. All scans done under 1-2% isoflurane anaesthesia. Figure made in BioRender.

### 2.2.10 Image analysis

For MPI, A 3D high sensitivity, isotropic (35 projections) scan was done of an empty bed to determine background signal. Using the software Vivoquant (Invicro), a region of interest (ROI) was manually drawn over the entire empty bed. The standard deviation was recorded. Based on the Rose Criterion, true signal was denoted as anything greater than 5x the standard deviation of the empty bed. ROIs of samples were drawn by gating for signal higher than the 5x standard deviation. MPI Pictures are taken in Vivoquant and displaced as a Maximum Projection Images. The total signal present in an MPI scan can be calculated using the following formula:

$$\text{Total MPI Signal} = \text{Mean Signal} \times \text{Volume (mm}^3\text{)}$$

Iron content present in each lesion was calculated using the formula below:

$$\text{Iron Content } (\mu\text{g}) = \frac{\text{Total MPI Signal (A.U.)}}{\text{Slope of Calibration Line}}$$

The mass of iron present in each cell was calculated during the MPI calibrations. The total iron content determined in a scan was divided by the number of cells imaged. This was repeated for cell numbers of  $1.024 \times 10^6$ ,  $5.12 \times 10^5$ ,  $2.56 \times 10^5$ ,  $1.28 \times 10^5$ ,  $6.40 \times 10^4$  and  $3.20 \times 10^4$ . The calculated values were averaged to give the rough iron content per cell. Standard deviation is used to show variance.

$$\text{Iron Content per Cell } (\mu\text{g}) = \frac{\text{Total Iron Content } (\mu\text{g})}{\text{Number of Cells Imaged}}$$

The number of cells in a region can be estimated at early time points by dividing the iron content by the iron content per cell.

For BLI, regions of interest were drawn around the primary signal as well as any secondary locations in the body also displaying signal. The ROI was a consistent size between each of the time points. The average BLI signal in each ROI was recorded.

### 2.2.11 Statistics

All statistics were conducted using the PRISM 9 software.

Linear regressions were used to plot trends for in vitro BLI signal Photons/s) vs cell number (n=3), the 3D MPI calibration curve, and total *in vitro* MPI signal vs cell number (n=3). The goodness of fit is

displayed by  $r^2$ . Significance was determined by P values less than 0.05. Standard Deviation was calculated for the variance between replicates. All error bars shown represent the standard deviation.

One-Way ANOVAs were used to determine whether different conditions were significantly different. This was used for both BLI signal and viability for unlabelled vs. iron-labelled cell populations. For cell detection limit experiments, this was used to compare both the MPI signal (A.U.) and the iron content ( $\mu\text{g}$ ) for different numbers of imaged cells. For *in vivo* experiments, One-Way ANOVAs were used to compare MPI signals (A.U.) for each day, Iron content for each day, and BLI signal for each day. Error bars and  $\pm$  denote standard deviation (n=4). P values are given for each comparison.

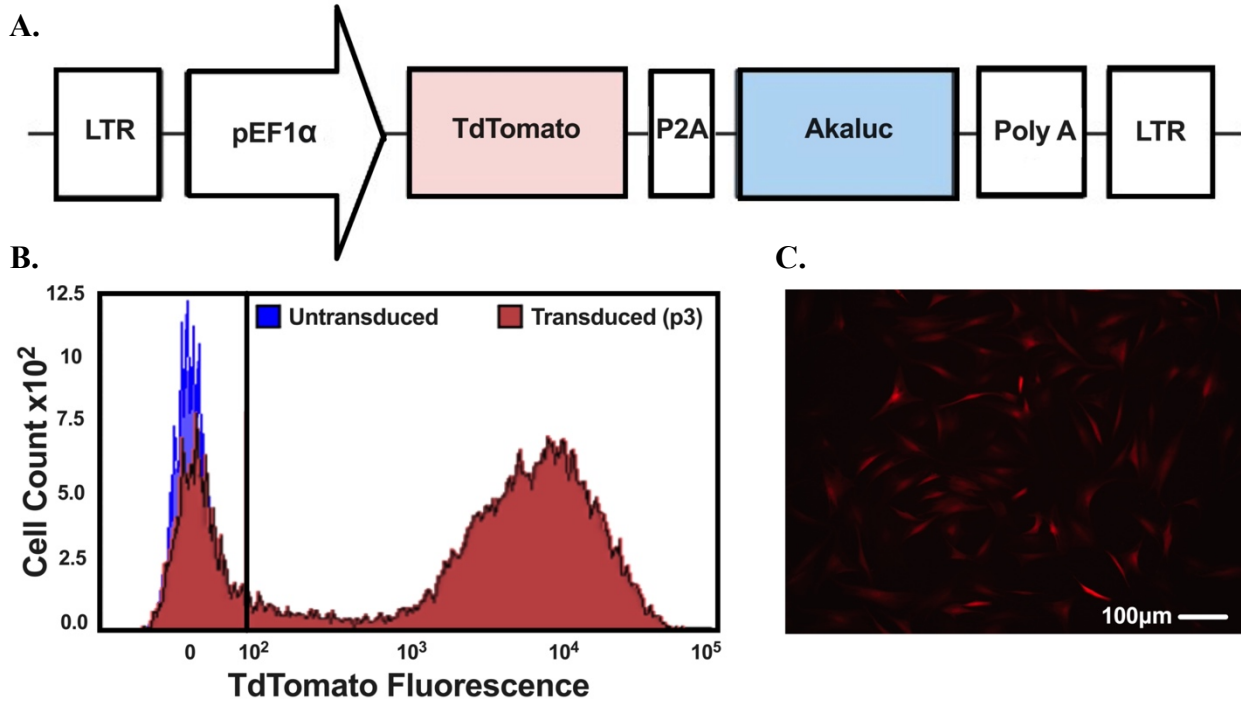
### 2.2.12 Ex Vivo Analysis

Following sacrifice with isoflurane, mice were perfused with 4% paraformaldehyde to fix tissues. The primary tumor and axillary lymph nodes were excised and stored in PBS at 4 °C degrees. A representative mouse was chosen for ex vivo analysis. Tissues were set on a plastic weighing dish, which was placed on the MPI bed. A 2D MPI scan was acquired for each excised tissue sample. The Primary tumour and lymph nodes were then cut in half for two separate sectioning and staining procedures. One half of each tissue were embedded in paraffin, sectioned, and stained with Perl's Prussian Blue, and Nuclear Fast Red counterstain (Refer to section 2.2.4 for more details on stain). This was used to determine whether SPIO was present in the tissue sections. Slides were imaged with brightfield microscopy on a ECHO Resolve microscope at 80 X magnification. The other tissue halves were passed through a sucrose gradient (10%, 20%, 30% sucrose in PBS) and then frozen. Mounting media containing the fluorescent dye 4',6'-diamidino-2-phenylindole (DAPI) was applied prior to imaging frozen sections. DAPI stains the DNA of all cells. Slides were imaged on an ECHO Resolve microscope with a 670 ms exposure time for fluorescence in the TdT channel, and 35 ms exposure time for fluorescence in the DAPI channel. Images were taken at 10 and 80 X magnification.

## 2.3 Results

### *2.3.1 Transduction of 4T1Br5 cells with TdTomato-Akaluc*

Cells were successfully transduced by the pEF1  $\alpha$ -TdTomato-Akaluc construct and were capable of producing both the functional TDT and Akaluc proteins, as demonstrated through Flow Cytometry. Cells successfully transduced with the construct were 77.6% positive for expressing some level of the TDT fluorophore (Figure 2.3 B). This level of expression remained constant through passages 3, 4, and 10, with fluorescence percentages of 76.9%, 76.3%, and 79.6% respectively. Fluorescence microscopy conducted on the same days visually showed similar percentages of cells expressing TdTomato fluorescence (cells appeared red when expressing TdTomato) (Figure 2.3 C).

**Figure 2.3:**

**Figure 2.3. Design and validation of Reporter Construct.** (A) Vector map consisting of pEF1 $\alpha$  promoter, TdTomato and Akaluc. (B) Flow cytometry of untransduced (blue) and transduced (red) cell populations at passage 3. Cell Count vs. TdT fluorescence was plotted in a histogram. TdTomato positive cells within gate. (C) Confocal microscopy further confirms expression of TdT.

### 2.3.2 *In Vitro* BLI

Total photon flux (P/s) measured with BLI was found to be positively and linearly correlated to the number of cells seeded ( $p=0.0034$ ,  $r^2=0.9613$ ) (Figure 2.4A, B). There were no significant differences in BLI signal between any of the replicates. Visually, no discernable differences in BLI signal were observed over 7 days between labeled and unlabeled cells (Figure 2.4C), and there were no significant differences between the two cell populations over all time points (Figure 2.4D).

**Figure 2.4:**

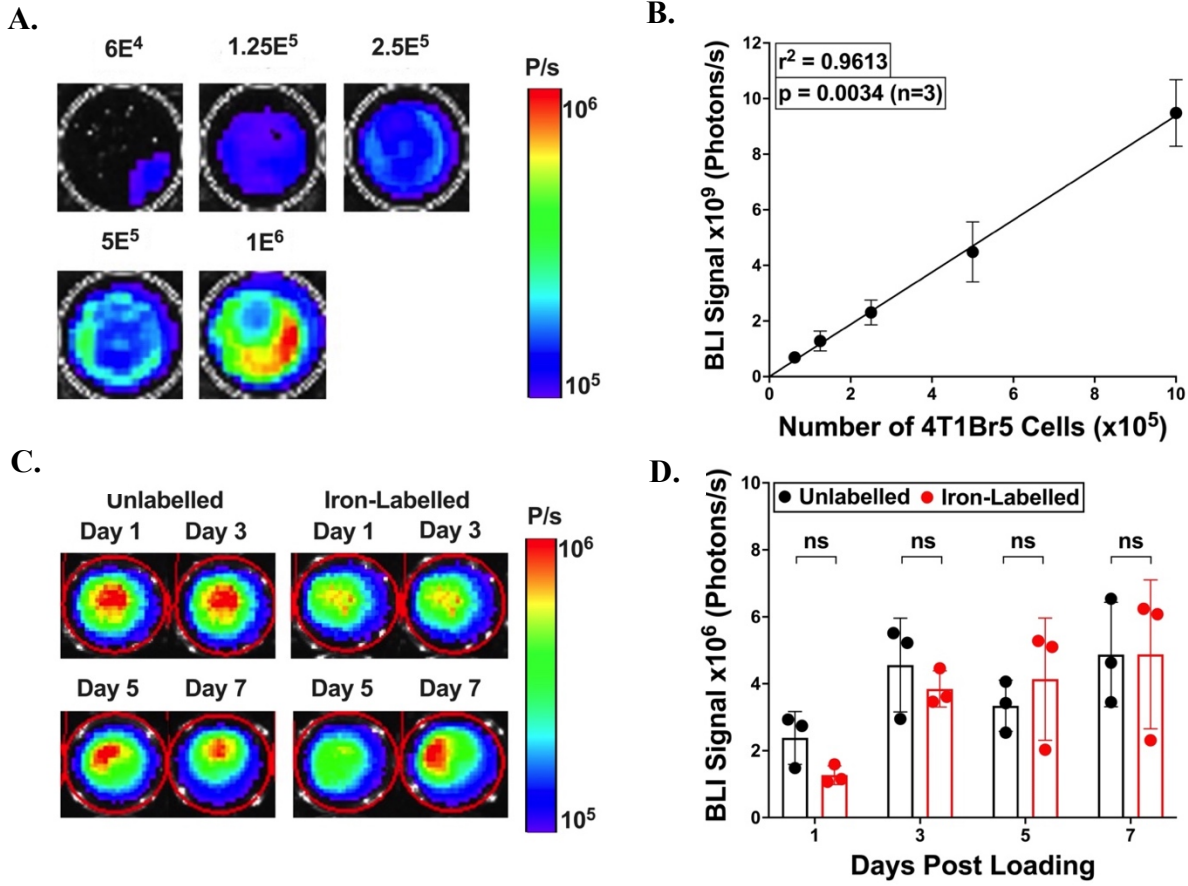


**Figure 2.4. Characterization of Transduced Cells.** Total BLI signal versus cell numbers ranging from  $6 \times 10^4$ -  $1 \times 10^6$  cells (A, B). BLI Signal scale shown in Photons per second (P/s). Unlabelled (Black), and Synomag-D labelled (Red) cells, 1 week post loading (C, D).



### *2.3.3 Characterization of Synomag-D*

The Relaxometer function on the Momentum™ MPI scanner was used to compare the sensitivity and resolution of Synomag-D to the more commonly used SPIO, Vivotrax. The sensitivity of Synomag-D was found to be 141.19 A.U., 3.8 times greater than the 45.10 A.U. measured for Vivotrax (Figure 2.5A), which was significantly different as calculated by an ANOVA ( $p < 0.0001$ ). 2.5B depicts the resolution for Synomag-D and Vivotrax as calculated by the full width half max (FWHM). For a 6.1 T/m gradient, Synomag-D had a resolution of 2.51 mm, which was 1.35 times greater than the 3.4 mm resolution calculated for Vivotrax. We found a significant linear relationship between the concentration of Synomag-D and resulting MPI signal (Figure 2.5C;  $r^2 = 0.9913$ ;  $p < 0.05$ ). Calibration lines were subsequently used to determine the iron content of unknown samples by dividing the MPI signal by the slope of the calibration line. The slope was found to be 214.16 ( $r^2 = 0.9913$ ) for the 3D High Sensitivity Isotropic scan.

### *2.3.4 Iron Labeling of Cells*

A Perl's Prussian Blue stain confirmed efficient cell labeling (98.9%) where iron appears blue within the counterstained 4T1Br5 cells (Figure 2.5D). Due to an extensive washing protocol, nearly all iron appeared to be within the cells, with little extracellular iron observed. Flow cytometry was used to assess the viability of cells labeled with iron (Figure 2.55E/F). The percentage of cells that were negative for Zombie Violet (viable cells) remained constant at 85-90% for labeled and unlabeled cells with no significant differences between the groups detected.

Figure 2.5:

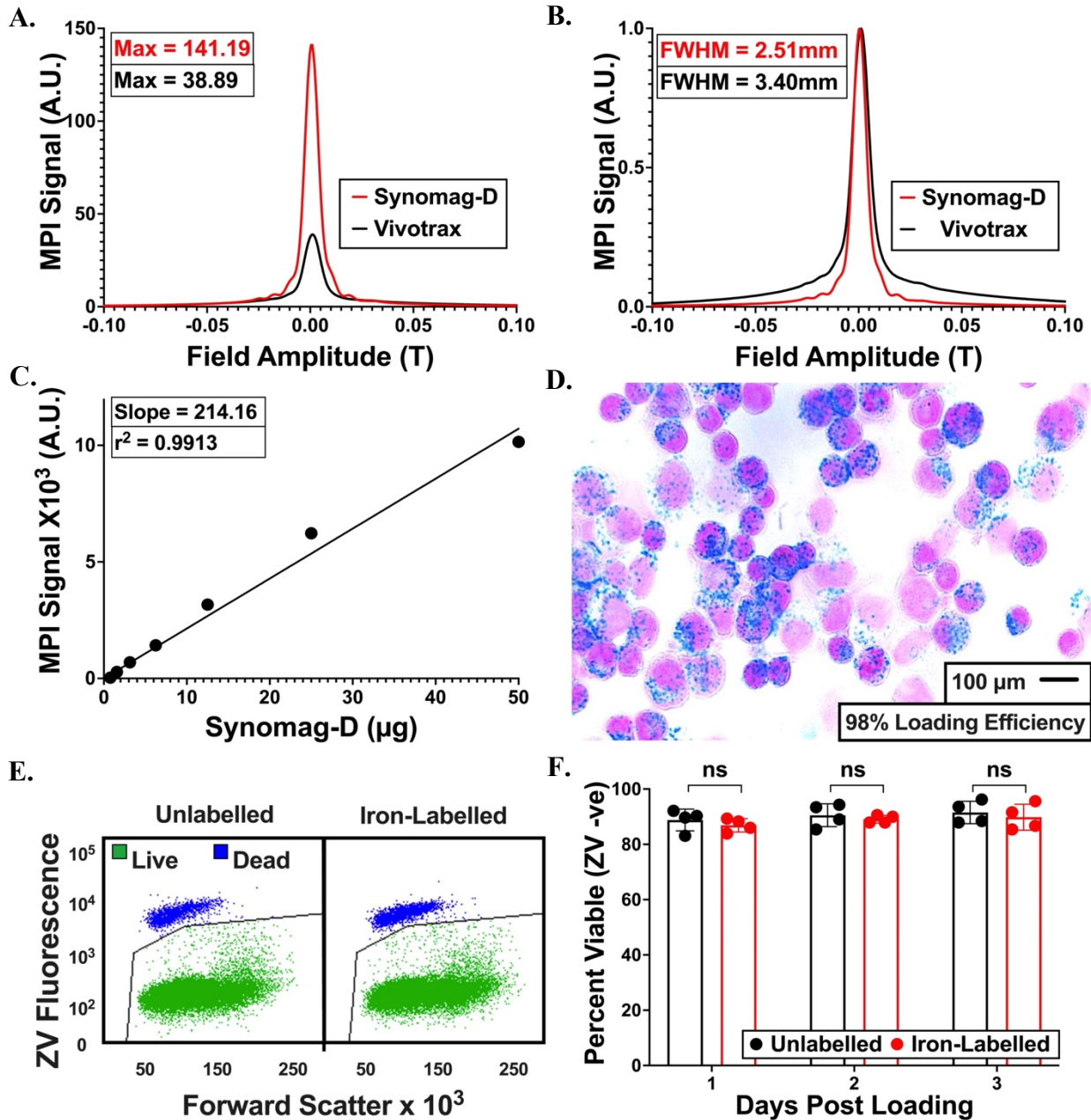


**Figure 2.5. Characterization of Synomag-D.** Relaxometry scans (A, B) were normalized to iron content for Synomag-D (10 µg/ µl) (red), and Vivotrax (5 µg/ µl) (black). Sensitivity (A), denoted by amplitude. Resolution (B) shown by FWHM. Synomag-D was 3.8x more sensitive than Vivotrax per gram of iron. 3D Calibration line (C) was made for a serial dilution of Synomag-D ranging from 50 µg to 0.7 µg. Calibration line later used to calculate unknown iron content from known values. Synomag-D loading of 4T1Br5-TdT-Akaluc cells was validated with Perl's Prussian stain and Nuclear Fast Red counterstain. Loading efficiency calculated by dividing number of cells with Synomag-D present by total number of cells (n=9). Viability assay conducted through Flow Cytometry for unlabelled and Synomag-D labelled cell populations. Viable cells are negative for Zombie Violet, plotted against Forward Scatter (E, F). Live cells shown in green.

### 2.3.5 *In Vitro* MPI

MPI scans were acquired for 12 different samples ranging from 500 to 1.024 million Synomag-D labeled cells (Figure 2.6A). MPI signal could be clearly visualized down to 64 000 cells (0.11  $\mu\text{g}$  of iron), while background noise became apparent at 16 000 cells (0.02  $\mu\text{g}$  of iron). In Figure 2.6, white boxes are drawn around “undetectable signal”, which was defined as signal below an SNR of 5 (the Rose Criterion; Rose, 1984; Bushberg et al., 2002). Cell numbers greater than or equal to 8000 (0.01  $\mu\text{g}$  of iron) were detectable with an SNR of 5 or higher (values above the red dashed line) (Figure 2.6B). Cell numbers greater than or equal to 1000 were detectable with an SNR of 3 or greater (values above the blue dashed line in Figure 2.6B). We found that the total MPI signal increased linearly with cell number ( $r^2 = 0.9863$ ) (Figure 2.6C; cell numbers below 8000 were not included as the signal was deemed “undetectable”). The lowest SNR (above 5) was the sample with 8000 cells (0.01  $\mu\text{g}$  of iron; SNR of 5.56) and the greatest SNR observed came from the sample with 1.024 million cells (3.67  $\mu\text{g}$  of iron; SNR of 36.96) (Table 1). The concentration of iron was calculated for each MPI scan by comparing the amount of signal to the calibration curve shown in Figure 2.5C. The amount of iron was found to be significantly different for a variety of cell numbers ranging from 8000 to 64000 and 64000 to 1.024 million (Figure 2.6 D/E) ( $p < 0.0001$ ). As expected, we found that as cell number increased, the total iron content significantly increased as well.

Figure 2.6:

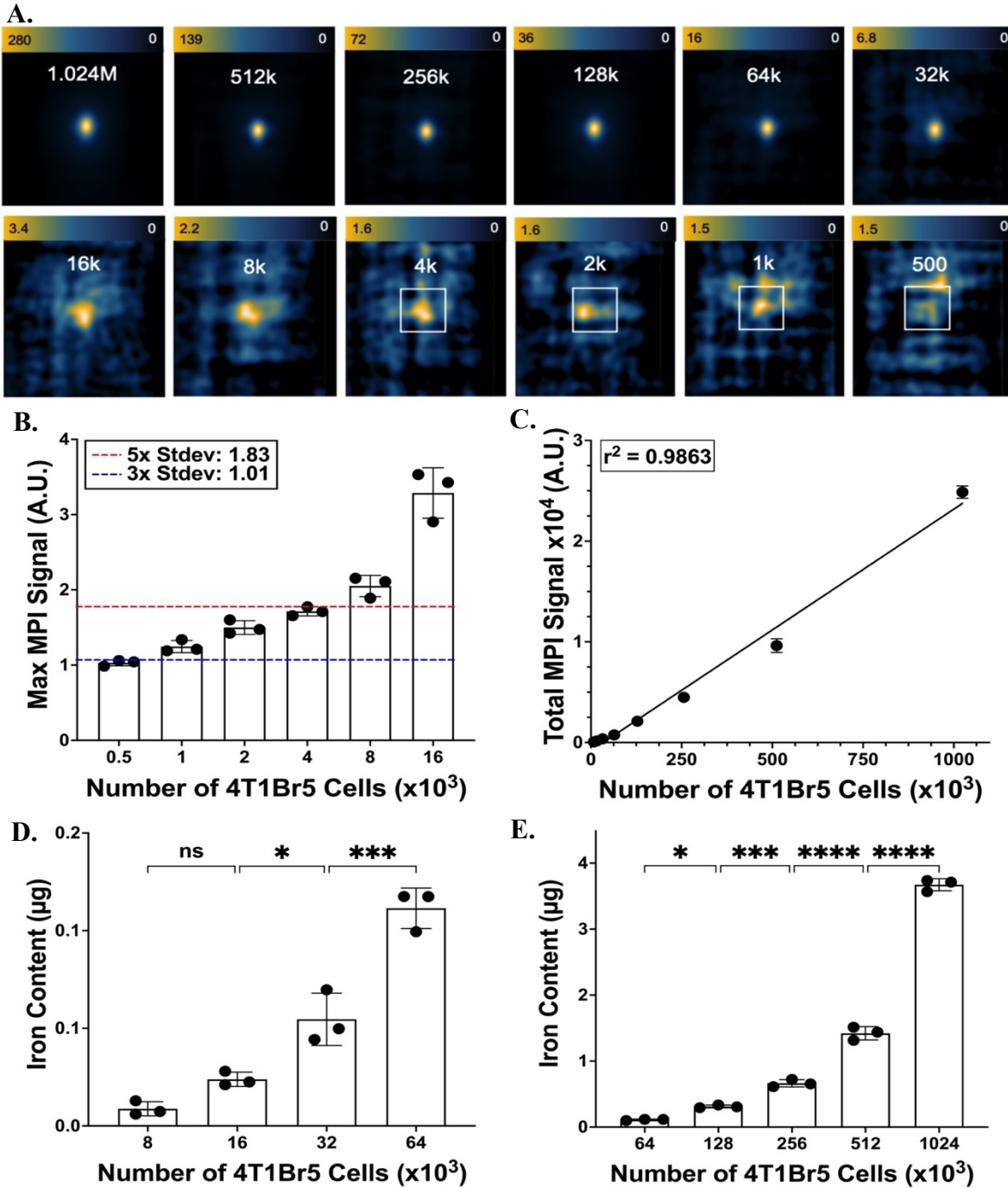


**Figure 2.6. Cell detection limits for Synomag-D labelled 4T1Br5-TdT-Akaluc cells.** (A) Representative MPI Images for respective cell numbers, where “M” denotes million, and “k” denotes thousand. White boxes enclose “undetectable signal” (signal below SNR = 5). (B) Maximum MPI signal for low cell numbers is plotted. Thresholds of 5, and 3 times the standard deviation of the background noise (SNR 5, SNR 3) are shown in red and blue, respectively. (C) Total MPI signal was plotted against the number of cells loaded with Synomag-D to show a positive and linear relationship. (D, E) Iron mass measured by MPI is significantly different for various cell numbers in the range of 8-64  $\times 10^3$  cells (D), and 64-1024  $\times 10^3$  cells (E).

Table 2.1:

<b>Average Cell Sensitivity (n=3)</b>		
<b>Cell Number x1000</b>	<b>Average SNR</b>	<b>Total Iron (<math>\mu\text{g}</math>)</b>
1024	36.96	3.67
512	26.90	1.42
256	18.95	0.66
128	14.74	0.31
64	14.81	0.11
32	10.27	0.05
16	6.80	0.02
8	5.56	0.01
4	<5	n/a

**Table 2.1: Cell detection limits for Synomag-D labelled 4T1Br5-TdT-Akaluc cells.** A dilution of Synomag-D loaded cells ranging from 1.024 million to 500 was done. Average SNR calculated by dividing the average mean signal from 3 replicates by the standard deviation of an empty bed (0.366). SNR below 5 is undetectable based on the Rose Criterion and is not shown. Total Iron Content calculated by dividing the total MPI signal (n=3) by the slope of the calibration curve shown in Figure 2.6C (6772).

### 2.3.6 *In Vivo* Imaging of Primary Tumours

4T1Br5-TdT-Akaluc cells were injected into the MFP of nude mice (n=4) and monitored with *in vivo* MPI and BLI over a period of two weeks. Nude mice were used instead of immunocompetent mice to avoid any potential immunogenicity problems arising from Akaluc expression. Signal appeared to be localized to the left MFP on both imaging modalities, which was the site of primary tumour inoculation. Alignment of images was done by acquiring brightfield images on both modalities, as shown in Figure 2.7A. MPI scans were then flipped horizontally as they were acquired in prone position while BLI was performed in supine position. MPI signal was detected in the left MFP of all mice on days 1 ( $846.24 \pm 210.55$  A.U.), 8 ( $579.35 \pm 134.88$  A.U.) and 14 ( $508.94 \pm 106.23$  A.U.) (Figure 2.7A; left column), with significant decrease in signal and corresponding iron content detected between days 1 and 14 ( $p < 0.05$ ) (Figure 2.7B, C). BLI signal was also detected in the left MFP of all mice on days 0 ( $7.31 \times 10^6 \pm 1.59 \times 10^6$  P/s), 6 ( $9.25 \times 10^7 \pm 5.92 \times 10^7$  P/s) and 13 ( $2.93 \times 10^8 \pm 1.84 \times 10^8$  P/s) (Figure 2.7 A; right column) with a significant increase in BLI signal observed between days 0 and 13 ( $p < 0.05$ ) (Figure 2.7D).

Figure 2.7:

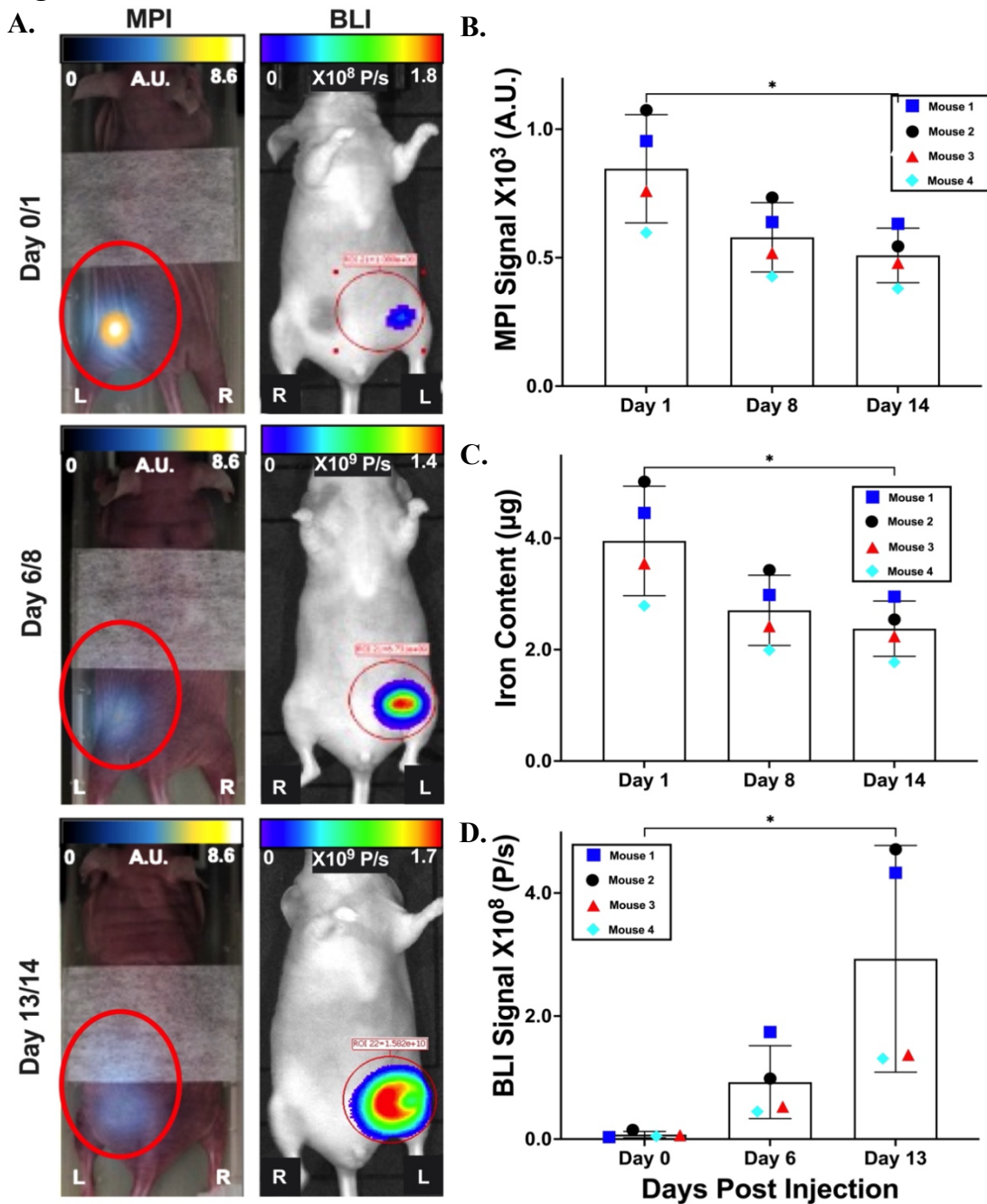


**Figure 2.7. Dual Akaluc BLI and MPI for tracking transplanted Synomag-D labelled 4T1Br5 cells *in vivo*.** Representative *in vivo* BLI and MPI scans (A) are shown for days 0/1, 6/8, and 13/14 post MFP injection of labelled cells. Anatomical left and right are denoted by “L” and “R” Bright field images used to localize MPI signal in respect to BLI signal. MPI signal in Arbitrary units (A.U.) enclosed by red circles. BLI displayed as photon flux (P/s). Total MPI (B), average iron content (calculated by dividing MPI signal by the slope of the 3D calibration line) (C) and Average BLI signal (D) were all plotted with respect to days post initial injection. Individual mice are colour coded to aid trend observation. Pairwise comparisons were done for (B), (C), and (D), showing significant differences in signal over time.

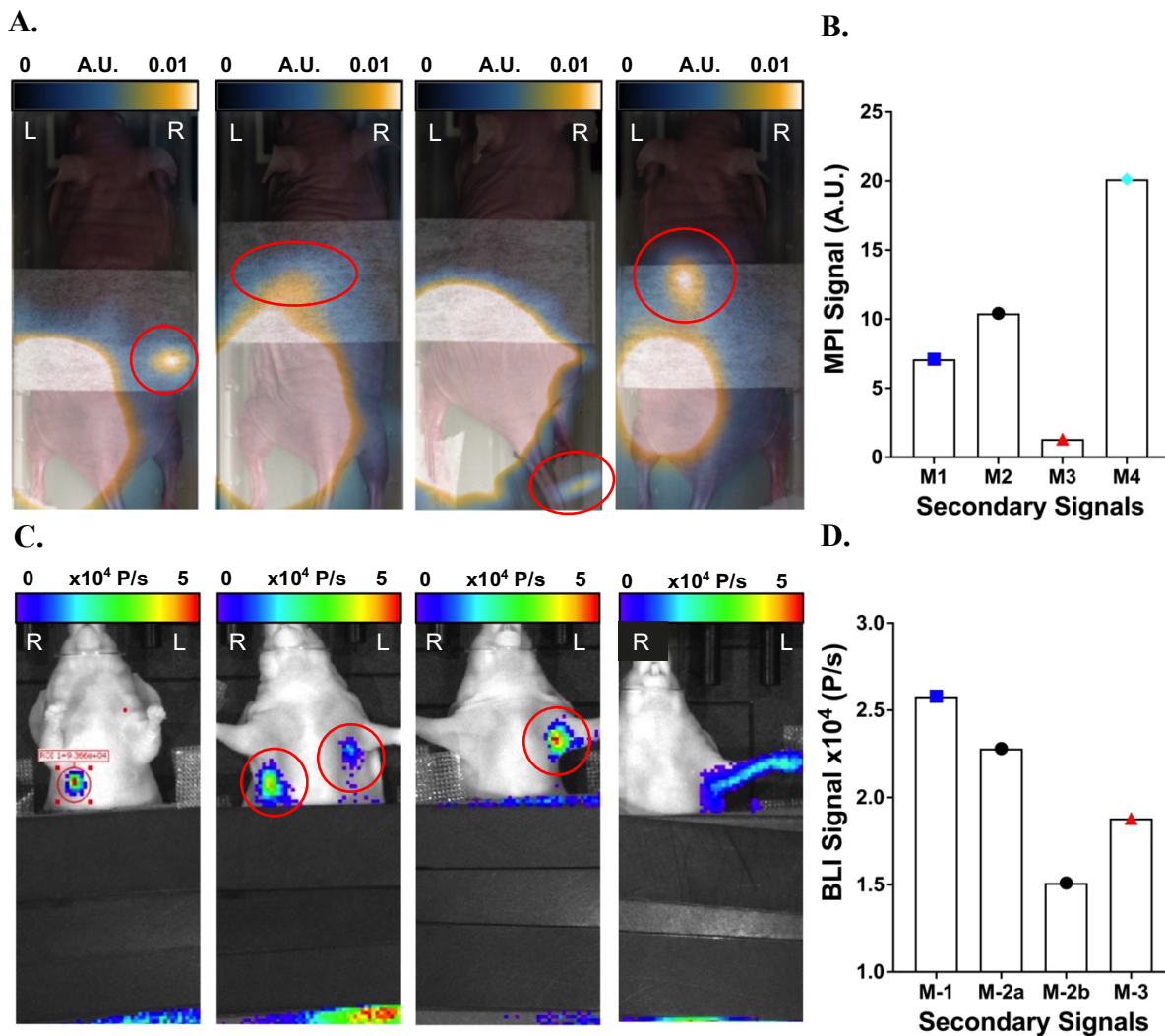
### *2.3.7 In Vivo Imaging of Spontaneous Metastases*

On day 14, MPI signal was detected at secondary sites throughout the body in all four mice (Figure 2.8A,B). All signals had an SNR of 5 or greater suggesting the distant MPI signal observed was true signal and not background. It is possible that these signals were the result of iron-labeled metastatic cancer cells. The locations of distant signal included the right footpad, the epigastric region and the right middle abdominal quadrant, although no two mice had metastases in the exact same location (Figure 2.8A,B). A representative image of a mouse with distant MPI signal in the right middle abdominal region on the contralateral side is shown in Figure 2.9B. In order to visualize this distant MPI signal a lower window level was needed. Primary signal highlighted in figure 8A is presented in the standard full dynamic range, corresponding to a max window level of 1.08. In comparison, the secondary lesion shown in figure 2.8B is presented with a max window level of 0.01.

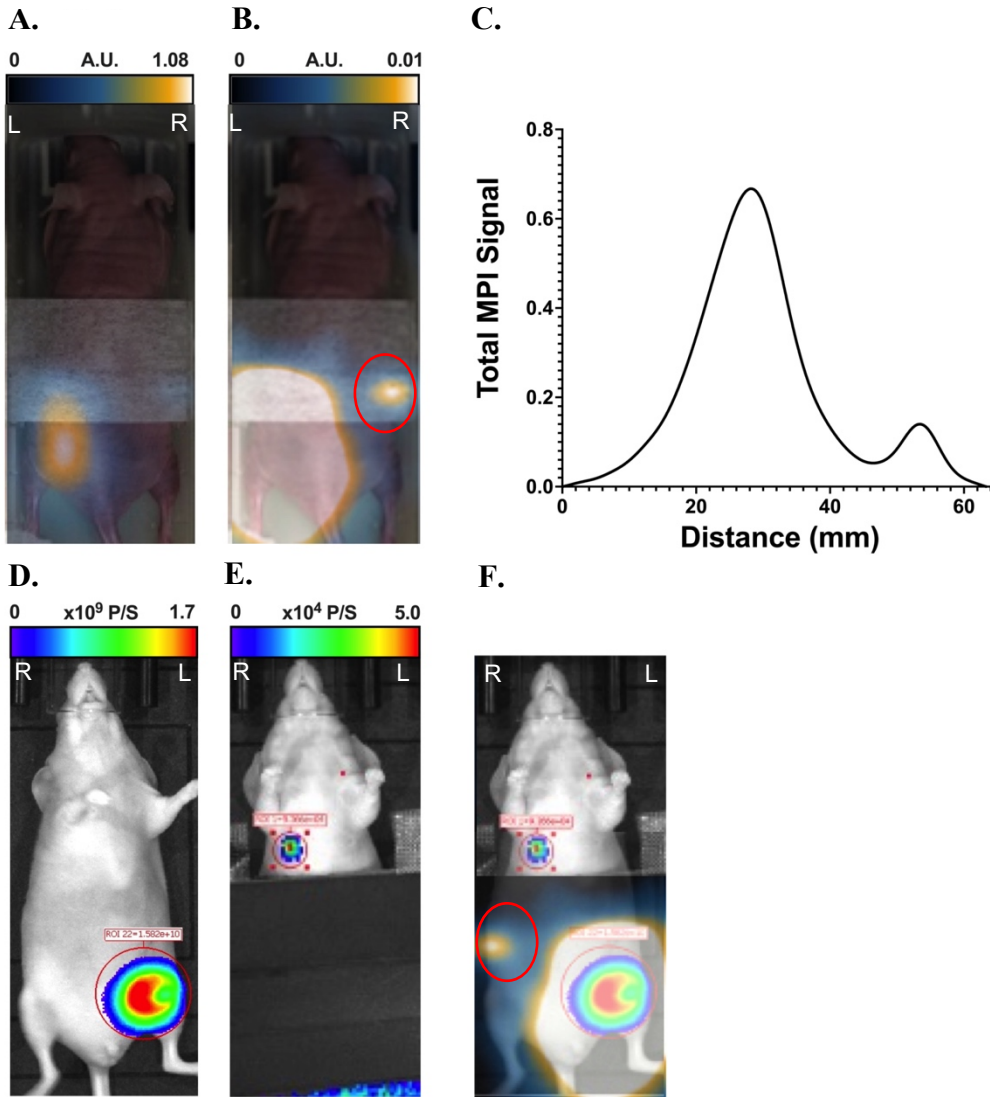
BLI signal was also detected at secondary sites in 3 of the 4 mice (Figure 2.8C,D) on day 13 by covering the lower abdomen of the animal (Figure 2.8E,G). This blocked a large portion of the signal coming from the primary tumour, allowing for longer exposure times and thus, smaller signals to be visualized. Without this, the strong primary signal masks any other signals that may be present in the mice (Figure 2.8D). A representative mouse with secondary signal observed in the upper right abdomen can be seen in Figure 2.9E. Two other mice showed BLI signal in the region of the ipsilateral armpit, and one mouse showed BLI signal in the contralateral armpit (Figure 2.8CD). Overlaying the MPI and BLI scans allowed for comparison of signal location between both modalities (Figure 2.8F) with distinct MPI and BLI signal regions noted.



Figure 2.8:



**Figure 2.8.** All secondary signals observed in MPI and Akaluc BLI *in vivo*. (A) MPI signals, separate from the primary signal are enclosed by red circles. Scans were overlaid on a bright field image for anatomical reference. (B) Quantification of secondary signals from each mouse, with M denoting mouse, followed by a number (M1, M2, M3, M4). (C) Akaluc BLI signals separate from the primary signal. A dark covering was taped to the bottom half of each mouse to prevent signal saturation. This allowed for visualization of the secondary signals as circled in red. (D) Quantification of secondary signals from each mouse. Mouse 2 had two secondary signals (M-2a, M-2b) while mouse 4 had no secondary signals. The signal observed for mouse 4 was due to scattering.

**Figure 2.9:**

**Figure 2.9. In vivo MPI and Akaluc BLI signal in distant regions.** All images are from the same representative mouse on day 13/14. The left and right of the mouse are marked by “L” and “R”. The MPI scan in (A) is windowed to the full dynamic range, while (B) is the same scan set to a lower window level. This allows visualization of a secondary signal location, marked by the red circle. A histogram (C) was made by drawing a line through both the primary and secondary signal locations in (B) and plotting signal intensity relative to location. Two distinct peaks can be observed indicating that the signals are indeed separate. BLI of the primary tumour signal (D) is the same image as seen in Figure 2.7. A dark covering was taped to the bottom half of the mouse in (E) to prevent signal saturation. This allowed for visualization of the secondary metastasis as circled in red. An overlay of MPI and BLI scans (G) allows for comparison of signal location anatomically. MPI signal was flipped to align with BLI scans.

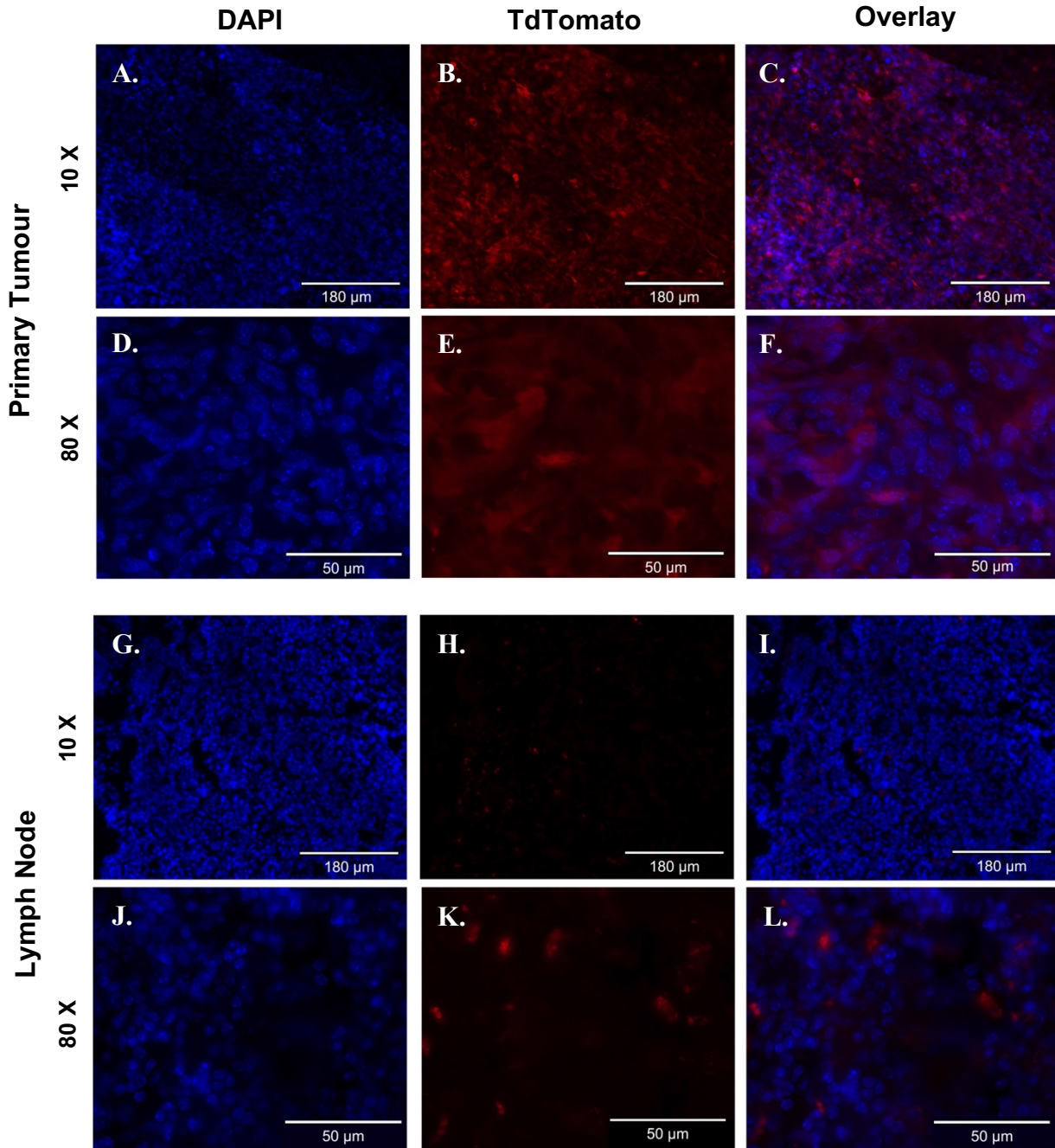
### ***2.3.8 Ex vivo Histology for transduced TdTomato-Akaluc reporter***

Post sacrifice, a representative mouse was assessed for the expression of TdTomato and Synomag-D in tissues. The presence of TdT (red) was determined through fluorescence microscopy using a DAPI (blue) counterstain. Cells expressing DAPI are seen in Figure 2.10A, D, G, J. Cells expressing TdT are represented by Figure 2.10B, E, H, K. An overlay of DAPI and TdT are presented in Figure 2.10C, F, I, L. Virtually all cells from the primary tumour were positive for both DAPI, and TdT, highlighted by the high level of signal overlap (Fig 2.10 A-F). Sections from the axillary lymph node which had displayed BLI signal during *in vivo* experiments exhibit a small fraction of TdT expressing cells in comparison to the number of DAPI expressing cells (Figure 2.10G-I), which can be seen more clearly at 80 X magnification (J-L). Some areas of the lymph node did not express TdT at all.

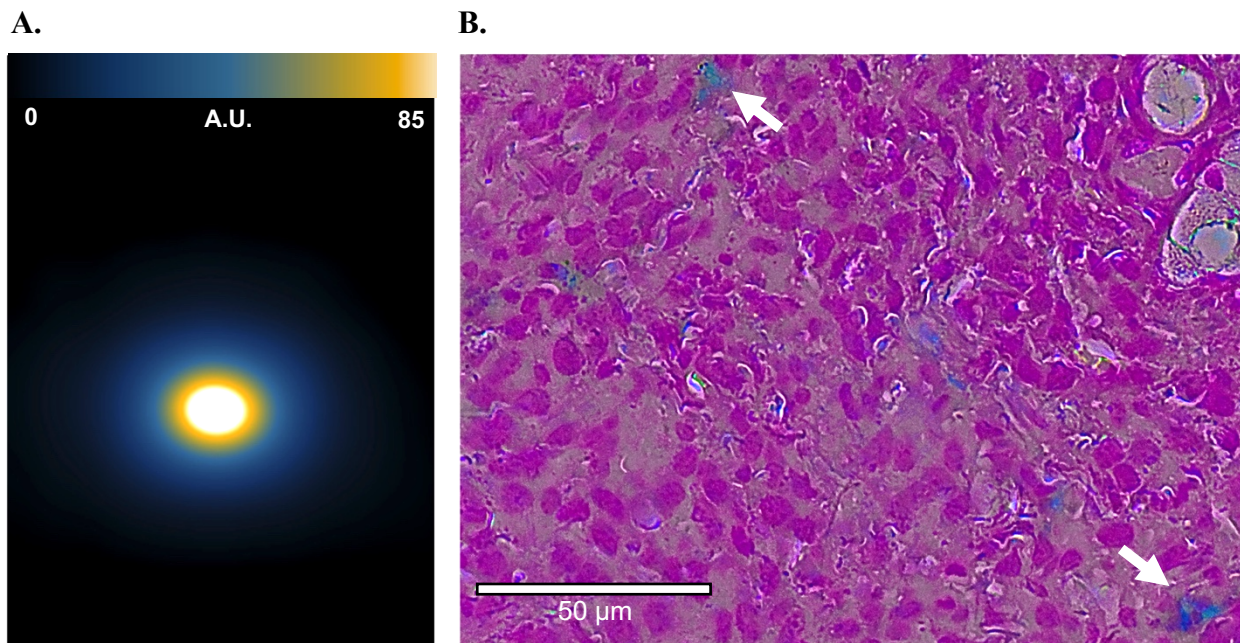
### ***2.3.9 Ex vivo Analysis of the MPI reporter Synomag-D***

The presence of Synomag-D in the tumour and lymph node was assessed using a 2D MPI scan, and through a PPB stain of the sectioned tissues. MPI signal was produced from the primary tumour (Figure 2.11A), but not from the lymph node (not shown). A PPB stain (Figure 2.11B) of sectioned tissues further confirmed the presence of iron (blue), in the primary tumour but not in the lymph node.

Figure 2.10:



**Figure 2.10. Ex vivo fluorescence microscopy of primary tumour and axillary lymph node.** Representative histology from one mouse, after tissue perfusion. DAPI (blue) stains all cell nuclei (A,D,G,J). Fluorescence in the TdTomato (red) channel, confirms expression of the transduced reporter (B, E, H, K). An overlay of DAPI and TdTomato was done to compare expression (C,F,I,L). Sections are shown at both 10 X (A-C,G-I) and 8 X (D-F,J-L) magnification. All cells of the primary tumour (A-F) were positive for TdTomato. A small fraction of cells in the lymph node were positive for TdTomato (G-L). All images taken on an ECHO Resolve microscope.

**Figure 2.11:**

**Figure 2.11. Ex vivo analysis of primary tumour for the MPI reporter Synomag-D.** 2D MPI of excised primary tumour (A), highlights that Synomag-D was present in the tumour. A representative PPB stain is displayed for one section of the primary tumour. Iron (blue) can be seen amongst the pink cancer cells, further confirming the presence of Synomag-D within the primary tumour. White arrows point to two examples of iron present in the tumour. Image of slide taken on an ECHO Resolve microscope.

## 2.4 Discussion

With the ever-increasing prevalence of metastatic cancer deaths (3), there is an urgent need for highly sensitive imaging technologies that can noninvasively visualize and quantify tumour burden in preclinical cancer models. Iron-based cellular MRI has historically been one of the most widely used techniques for tracking the fate and biodistribution of cancer cells *in vivo* (11-14), however, the indirect detection of SPIO through signal blooming, makes quantifying cell number difficult (16). Alternatively, MPI, a new player in the field of cell tracking, can directly detect SPIO labeled cells allowing for quantitative hotspot imaging (22,23), although the sensitivity is not yet on par with cellular MRI, and *in vivo* resolution has been an ongoing problem. BLI, has often been paired with MRI or MPI, due to its ability to reliably track both proliferation and viability, something not possible with probe-based modalities. BLI has been traditionally limited its low depth penetration, however, the development of Akaluc, and Akalumine, a NIR BLI reporter system, greatly mitigates this. Akaluc BLI has been shown to offer lower signal attenuation, superior depth penetration, and higher sensitivity for small animal imaging compared to the traditional luciferase reporter systems (51-53).

This is the first study to combine MPI and Akaluc BLI for quantitative, high sensitivity tracking of metastatic cancer cells in a preclinical breast cancer model. We believe the implementation of this strategy will be extremely valuable in studying the underlying mechanisms of cancer metastasis as well as provide the imaging framework to more accurately evaluate therapeutic efficacy *in vivo* during the development of new anti-cancer agents.

Several groups have previously demonstrated the ability of MPI to track cancer cells, however few have combined MPI with an optical imaging technique, and none have combined it with Akaluc BLI. Yu et al., in 2017, became the first group to visualize cancer cells *in vivo* with MPI when they tracked the uptake of IV administered MPI nanoparticles by a subcutaneous breast cancer tumour via the EPR effect (27). BLI was used on day 1, as a positive control for cell location. In 2018, both Song et al., and Jung et al., tracked MPI cancer cells labelled with MPI nanoparticles expressing fluorescent moieties. However, by using fluorescent moieties, rather than a fluorescent reporter gene, this method did not allow for visualization of proliferation or viability (32,55). Parkins et al., in 2020, tracked circulating tumour cells with MPI, however no optical imaging system was used (56). Later in 2020, Melo et al.,

used MPI to track the metastasis of cancer cells to the brain of mice (57). In 2021, Knier et al., tracked patient derived xenografts with both MPI and BLI, however the same mice were not imaged on both modalities (58). Makela et al., in 2021, used MPI and Red-Fluc BLI to track 4T1 cell implantation, tumour growth, and the subsequent spontaneous metastasis to the lymph node. However, BLI signal was not quantified (59). Based on the emission spectra of Red-Fluc and Akaluc BLI, Akaluc should have far superior depth penetration and sensitivity *in vivo*.

While the literature on the implementation of Akaluc BLI for cancer cell tracking is sparse, this system has demonstrated the ability to sensitively track both tumour burden and metastasis, although it has yet to be paired with MPI. In 2018, Iwano et al., were able to detect single Akaluc expressing cells implanted in the lungs of mice, mimicking metastasis to one of the deepest regions (53). In 2021, both Liu et al., and Ichise et al., tracked spontaneous lung metastases *in vivo* using MPI (60,61). Additionally, the treatment of these metastases by NK cells was evaluated in the Ichise paper, however, at the time of writing this has yet to be peer reviewed (61).

Here, for the first time, we were able to detect and quantify cancer cells in the same mouse using MPI and Akaluc BLI. There was high concordance between the location of MPI and BLI signal at early time points, indicating that the same cell populations were being imaged on both modalities. Additionally, there was no observable background signal in the gut for either MPI or Akaluc BLI. A reoccurring problem in MPI is a gut signal caused by contamination of food and bedding (62,63), however by fasting as well as the removal of bedding prior to imaging, this was mitigated. Removing this background signal allows for the detection of cells in regions that may have otherwise been hidden such as in the lower abdomen. Additionally, several sources have reported background liver signal with Akalumine, in the absence of Akaluc (27,64), however, this was not observed for this experiment.

By the experimental endpoint, MPI and BLI signal differed greatly. MPI signal decreased by roughly 40% by day 14, suggesting probe dilution because of highly proliferative cells losing their iron label through cell division. Interestingly, this drop in signal occurred at a far more rapid rate than what was previously reported by Song et al., in 2018. In that paper, MPI signal only decreased by 20% over a 20-day span (32). This increased rate in signal loss may suggest that for highly proliferative cell lines, MPI may not be a reliable tool for long-term quantification of cells. In contrast, the BLI signal observed on day 13 was more than a 28-fold increase from the signal detected on day 1, which was expected as primary tumours grew. These inversed trends between MPI and BLI data match the results

reported by Knier et al., and Makela et al., in 2021 and demonstrates that BLI can provide information on cell proliferation for future MPI studies (58,59).

Additionally, by the experimental endpoint, both MPI and BLI were able to detect signal from regions outside of the primary MFP tumour. These signals are possibly a result of metastases. Both BLI and MPI have previously demonstrated the ability to detect metastases in mice (53,57,59,60), however, in this study, MPI was able to detect iron signal that was covered up during our BLI metastases imaging protocol. Specifically, Akaluc BLI was able to detect signal in distal regions such as the armpit or upper gut, however, doing so required covering the primary tumour. MPI signal was not detected in these distant lesions. This was likely due to the dilution of tracer minimizing the amount of iron present within the cells that seeded the metastasis. The *ex vivo* histology supports this theory, as no iron was detected in a lymph node which was positive for BLI signal and negative for MPI signal *in vivo*. However, MPI signal was detectable in more proximal regions to the primary tumours, as no covering was needed. Although no histology was done to confirm that these were metastases, a line plot through the primary tumour and the secondary lesion revealed two distinct signal peaks, indicating that this secondary signal was not associated with the primary tumour. The discrepancy between secondary locations observed through MPI and BLI highlight the benefits of using both modalities to give a more complete picture of cancer cell fate in this spontaneous metastasis model. The use of a single modality may result in missing critical information, hindering the true assessment of disease progression.

While the sensitivity of Akaluc as a BLI reporter gene has been well established, it is important to also consider the added sensitivity of Synomag-D for MPI cell tracking. In concurrence with Vogel et al., 2021 and Sehl et al., 2020, we found that Synomag-D was nearly 4 times as sensitive as the standard Vivotrax, with a similar resolution for detecting particles *in vitro* (21,30). This reflects an *in vivo* detection limit of 0.01 µg of iron or approximately 8000 cells. In a similar experiment by our lab, as few as 4000 Synomag-D labelled dendritic cells could be detected *in vivo*, corresponding to an iron volume of 0.02 µg. The discrepancy in values can be attributed to the concentration of iron present within each cell ( $2.18 \pm 0.8$  pg/cell vs. 5.5 pg/cell) (63). Unlike many immune cells, cancer cells are not naturally phagocytic. This makes labelling cancer cells with high concentrations of iron difficult and may limit the sensitivity future MPI cancer cell tracking experiments. MPI has not yet reached the



single cell sensitivity that is possible with MRI or Akaluc BLI however, advancements in tailored MPI tracers and imaging techniques will soon allow for detection of smaller metastases at earlier timepoints. Additionally, our study provides evidence that labeling cells with Synomag-D has no significant effects on cell viability or BLI signal. These findings are encouraging for the potential clinical use of Synomag-D as an MPI tracer for additional studies.

MPI studies are often limited by the dilution of MPI tracer over time, as well as bystander cell labeling (11-13,34,65). By adding complementary Akaluc-BLI to our MPI study, this was no longer a concern, however there are still a few limitations to be considered. First, while the *in vivo* results are promising, a small sample size was used. Future studies should be conducted to assess the reproducibility of these findings as well as explore other imaging time points. Second, due to the potential stress of isoflurane anaesthesia, MPI and BLI were performed on different days, which limited the comparison that could be made between the two modalities. Additionally, mice were imaged in the prone position for MPI, and the supine position for BLI. Images needed to be flipped horizontally, before the signals could be aligned. Quantification of MPI signal provides its own challenges. While the primary and secondary signal locations were distinct from one another, the tails of each signal overlapped to some degree, as seen in the histogram (Figure 2.8C). As a result, the exact quantification of secondary lesions is unlikely. Finally, no histology was done for MPI positive secondary lesions, which prevented us from confirming that these were in fact metastases. By the time the BLI and MPI signals were aligned, tissues had already been collected for *ex vivo* analysis, and we were unaware that the signals originated from different locations. A faster pipeline of aligning the images at endpoint will hopefully prevent this from happening in the future.

In this study, we demonstrated for the first time the ability to track metastatic cancer cells *in vivo* with both MPI and Akaluc BLI. As highlighted by the differences in secondary metastasis detection, MPI and BLI provide complementary information on cell fate, which will provide a more complete picture on the intricacies of cancer metastasis. In this study, breast cancer cells are the first and only cell type of any kind to be tracked with this multimodal imaging approach. Future experiments will use this framework to track both proliferative and non-proliferative cell populations including other cancers, stem cells and immune cells. Specifically, we hope to use this model to track the delivery and therapeutic effect of cellular therapies such as CAR-T or NK cells, the former which has already begun separately with both modalities (66,67). Additionally, in the future, MPI may be combined with other reporter gene modalities that are clinically relevant such as PET

## 2.5 References

1. Dillekås, H., Rogers, M. S., & Straume, O. (2019). Are 90% of deaths from cancer caused by metastases? *Cancer Medicine*, 8(12), 5574–5576. <https://doi.org/https://doi.org/10.1002/cam4.2474>
2. Patanaphan, V., Salazar, O. M., & Risco, R. (1988). *Breast cancer: metastatic patterns and their prognosis*. *Southern medical journal*, 81(9), 1109–1112.
3. Cagan, R., & Meyer, P. (2017). Rethinking cancer: current challenges and opportunities in cancer research. *Disease models & mechanisms*, 10(4), 349–352. <https://doi.org/10.1242/dmm.030007>
4. Condeelis, J., & Weissleder, R. (2010). In vivo imaging in cancer. *Cold Spring Harbor perspectives in biology*, 2(12), a003848. <https://doi.org/10.1101/cshperspect.a003848>
5. Bulte, J. W., & Kraitchman, D. L. (2004). Iron oxide MR contrast agents for molecular and cellular imaging. *NMR in biomedicine*, 17(7), 484–499. <https://doi.org/10.1002/nbm.924>
6. Frank, J. A., Zywicke, H., Jordan, E. K., Mitchell, J., Lewis, B. K., Miller, B., Bryant, L. H., Jr, & Bulte, J. W. (2002). Magnetic intracellular labeling of mammalian cells by combining (FDA-approved) superparamagnetic iron oxide MR contrast agents and commonly used transfection agents. *Academic radiology*, 9 Suppl 2, S484–S487. [https://doi.org/10.1016/s1076-6332\(03\)80271-4](https://doi.org/10.1016/s1076-6332(03)80271-4)
7. Frank, J. A., Miller, B. R., Arbab, A. S., Zywicke, H. A., Jordan, E. K., Lewis, B. K., Bryant, L. H., Jr, & Bulte, J. W. (2003). Clinically applicable labeling of mammalian and stem cells by combining superparamagnetic iron oxides and transfection agents. *Radiology*, 228(2), 480–487. <https://doi.org/10.1148/radiol.2281020638>
8. Yurt, A., & Kazancı, N. (2008). Investigation of magnetic properties of various complexes prepared as contrast agents for MRI. *Journal of Molecular Structure*, 892(1), 392–397. <https://doi.org/https://doi.org/10.1016/j.molstruc.2008.06.024>
9. Shokrollahi, H. (2013). Contrast agents for MRI. *Materials Science and Engineering: C*, 33(8), 4485–4497. <https://doi.org/https://doi.org/10.1016/j.msec.2013.07.012>
10. Hinds, K. A., Hill, J. M., Shapiro, E. M., Laukkanen, M. O., Silva, A. C., Combs, C. A., Varney, T. R., Balaban, R. S., Koretsky, A. P., & Dunbar, C. E. (2003). Highly efficient endosomal labeling of progenitor and stem cells with large magnetic particles allows magnetic resonance imaging of single cells. *Blood*, 102(3), 867–872. <https://doi.org/10.1182/blood-2002-12-3669>
11. Heyn, C., Ronald, J. A., Mackenzie, L. T., MacDonald, I. C., Chambers, A. F., Rutt, B. K., & Foster, P. J. (2006). In vivo magnetic resonance imaging of single cells in mouse brain with optical validation. *Magnetic resonance in medicine*, 55(1), 23–29. <https://doi.org/10.1002/mrm.20747>

12. Heyn, C., Ronald, J. A., Ramadan, S. S., Snir, J. A., Barry, A. M., MacKenzie, L. T., Mikulis, D. J., Palmieri, D., Bronder, J. L., Steeg, P. S., Yoneda, T., MacDonald, I. C., Chambers, A. F., Rutt, B. K., & Foster, P. J. (2006). In vivo MRI of cancer cell fate at the single-cell level in a mouse model of breast cancer metastasis to the brain. *Magnetic resonance in medicine*, *56*(5), 1001–1010. <https://doi.org/10.1002/mrm.21029>
13. Foster, P. J., Dunn, E. A., Karl, K. E., Snir, J. A., Nycz, C. M., Harvey, A. J., & Pettis, R. J. (2008). Cellular magnetic resonance imaging: in vivo imaging of melanoma cells in lymph nodes of mice. *Neoplasia (New York, N.Y.)*, *10*(3), 207–216. <https://doi.org/10.1593/neo.07937>
14. Shapiro, E.M., Sharer, K., Skrtic, S. and Koretsky, A.P. (2006), In vivo detection of single cells by MRI. *Magnetic Resonance in Medicine*, *55*: 242-249. <https://doi.org/10.1002/mrm.20718>
15. Shapiro, E. M., Medford-Davis, L. N., Fahmy, T. M., Dunbar, C. E., & Koretsky, A. P. (2007). Antibody-mediated cell labeling of peripheral T cells with micron-sized iron oxide particles (MPIOs) allows single cell detection by MRI. *Contrast media & molecular imaging*, *2*(3), 147–153. <https://doi.org/10.1002/cmml.134>
16. Liu, W., Dahnke, H., Jordan, E. K., Schaeffter, T., & Frank, J. A. (2008). In vivo MRI using positive-contrast techniques in detection of cells labeled with superparamagnetic iron oxide nanoparticles. *NMR in Biomedicine*, *21*(3), 242–250. <https://doi.org/https://doi.org/10.1002/nbm.1187>
17. Shetty, A. S., Sipe, A. L., Zulfiqar, M., Tsai, R., Raptis, D. A., Raptis, C. A., & Bhalla, S. (2019). In-phase and opposed-phase imaging: Applications of chemical shift and magnetic susceptibility in the chest and abdomen. *Radiographics*, *39*(1), 115–135. <https://doi.org/10.1148/rg.2019180043>
18. Liu, W., & Frank, J. A. (2009). Detection and quantification of magnetically labeled cells by cellular MRI. *European journal of radiology*, *70*(2), 258–264. <https://doi.org/10.1016/j.ejrad.2008.09.021>
19. Cromer Berman, S. M., Walczak, P., & Bulte, J. W. M. (2011). Tracking stem cells using magnetic nanoparticles. *WIREs Nanomedicine and Nanobiotechnology*, *3*(4), 343–355. <https://doi.org/https://doi.org/10.1002/wnan.140>
20. Bulte, J. W., Walczak, P., Janowski, M., Krishnan, K. M., Arami, H., Halkola, A., Gleich, B., & Rahmer, J. (2015). Quantitative "Hot Spot" Imaging of Transplanted Stem Cells using Superparamagnetic Tracers and Magnetic Particle Imaging (MPI). *Tomography (Ann Arbor, Mich.)*, *1*(2), 91–97. <https://doi.org/10.18383/j.tom.2015.00172>
21. Sehl, O. C., Gevaert, J. J., Melo, K. P., Knier, N. N., & Foster, P. J. (2020). A perspective on cell tracking with magnetic particle imaging. *Tomography*, *6*(4), 315–324. <https://doi.org/10.18383/j.tom.2020.00043>
22. Gleich, B. (2001). Verfahren zur Ermittlung der räumlichen Verteilung magnetischer Partikel. *German Patent DE-10151778-A1*.
23. Gleich, B., & Weizenecker, J. (2005). Tomographic imaging using the nonlinear response of magnetic particles. *Nature*, *435*(7046), 1214–1217. <https://doi.org/10.1038/nature03808>

24. Wu, L. C., Zhang, Y., Steinberg, G., Qu, H., Huang, S., Cheng, M., Bliss, T., Du, F., Rao, J., Song, G., Pisani, L., Doyle, T., Conolly, S., Krishnan, K., Grant, G., & Wintermark, M. (2019). A Review of Magnetic Particle Imaging and Perspectives on Neuroimaging. *AJNR. American journal of neuroradiology*, *40*(2), 206–212. <https://doi.org/10.3174/ajnr.A5896>
25. Saritas, E. U., Goodwill, P. W., Croft, L. R., Konkle, J. J., Lu, K., Zheng, B., & Conolly, S. M. (2013). Magnetic particle imaging (MPI) for NMR and MRI researchers. *Journal of magnetic resonance (San Diego, Calif. : 1997)*, *229*, 116–126. <https://doi.org/10.1016/j.jmr.2012.11.029>
26. Zheng, B., Yu, E., Orendorff, R., Lu, K., Konkle, J. J., Tay, Z. W., Hensley, D., Zhou, X. Y., Chandrasekharan, P., Saritas, E. U., Goodwill, P. W., Hazle, J. D., & Conolly, S. M. (2017). Seeing SPIOs Directly In Vivo with Magnetic Particle Imaging. *Molecular imaging and biology*, *19*(3), 385–390. <https://doi.org/10.1007/s11307-017-1081-y>
27. Yu, E. Y., Bishop, M., Zheng, B., Ferguson, R. M., Khandhar, A. P., Kemp, S. J., Krishnan, K. M., Goodwill, P. W., & Conolly, S. M. (2017). Magnetic Particle Imaging: A Novel in Vivo Imaging Platform for Cancer Detection. *Nano letters*, *17*(3), 1648–1654. <https://doi.org/10.1021/acs.nanolett.6b04865>
28. Talebloo, N., Gudi, M., Robertson, N., & Wang, P. (2020). Magnetic Particle Imaging: Current Applications in Biomedical Research. *Journal of magnetic resonance imaging*, *51*(6), 1659–1668. <https://doi.org/10.1002/jmri.26875>
29. Grüttner, A., Kowalski, F., Fidler, M., Steinke, F., Westphal, & Teller, H. (2018). Nanoflower particles: A new tracer for mpi, physical characterization and initial in vitro toxicity studies. *International Workshop on Magnetic Particle Imaging*, 17-18.
30. Vogel, P., Kampf, T., Rückert, M. A., Grüttner, C., Kowalski, A., Teller, H., & Behr, V. C. (2021). Synomag®: The new high-performance tracer for magnetic particle imaging. *International Journal on Magnetic Particle Imaging*, *7*(1). <https://doi.org/10.18416/IJMPI.2021.2103003>
31. Zheng, B., Vazin, T., Goodwill, P. W., Conway, A., Verma, A., Saritas, E. U., Schaffer, D., & Conolly, S. M. (2015). Magnetic Particle Imaging tracks the long-term fate of in vivo neural cell implants with high image contrast. *Scientific reports*, *5*, 14055. <https://doi.org/10.1038/srep14055>
32. Song, G., Chen, M., Zhang, Y., Cui, L., Qu, H., Zheng, X., Wintermark, M., Liu, Z., & Rao, J. (2018). Janus Iron Oxides @ Semiconducting Polymer Nanoparticle Tracer for Cell Tracking by Magnetic Particle Imaging. *Nano letters*, *18*(1), 182–189. <https://doi.org/10.1021/acs.nanolett.7b03829>
33. Tay, Z. W., Savliwala, S., Hensley, D. W., Fung, K. L. B., Colson, C., Fellows, B. D., Zhou, X., Huynh, Q., Lu, Y., Zheng, B., Chandrasekharan, P., Rivera-Jimenez, S. M., Rinaldi-Ramos, C. M., & Conolly, S. M. (2021). Superferromagnetic Nanoparticles Enable Order-of-Magnitude

Resolution & Sensitivity Gain in Magnetic Particle Imaging. *Small Methods*, 2100796.  
<https://doi.org/https://doi.org/10.1002/smt.202100796>

34. Amsalem, Y., Mardor, Y., Feinberg, M. S., Landa, N., Miller, L., Daniels, D., Ocherashvilli, A., Holbova, R., Yosef, O., Barbash, I. M., & Leor, J. (2007). Iron-oxide labeling and outcome of transplanted mesenchymal stem cells in the infarcted myocardium. *Circulation*, 116(11 Suppl), I38–I45. <https://doi.org/10.1161/CIRCULATIONAHA.106.680231>
35. Alsawaftah, N., Farooq, A., Dhou, S., & Majdalawieh, A. F. (2021). Bioluminescence Imaging Applications in Cancer: A Comprehensive Review. *IEEE reviews in biomedical engineering*, 14, 307–326. <https://doi.org/10.1109/RBME.2020.2995124>
36. Bu, L., Ma, X., Tu, Y., Shen, B., & Cheng, Z. (2013). Optical image-guided cancer therapy. *Current pharmaceutical biotechnology*, 14(8), 723–732. <https://doi.org/10.2174/1389201014666131226112507>
37. Söling, A., & Rainov, N. G. (2003). Bioluminescence imaging in vivo - application to cancer research. *Expert opinion on biological therapy*, 3(7), 1163–1172. <https://doi.org/10.1517/14712598.3.7.1163>
38. Edinger, M., Sweeney, T. J., Tucker, A. A., Olomu, A. B., Negrin, R. S., & Contag, C. H. (1999). Noninvasive assessment of tumor cell proliferation in animal models. *Neoplasia (New York, N.Y.)*, 1(4), 303–310. <https://doi.org/10.1038/sj.neo.7900048>
39. Kozlowski, J. M., Fidler, I. J., Campbell, D., Xu, Z. L., Kaighn, M. E., & Hart, I. R. (1984). Metastatic behavior of human tumor cell lines grown in the nude mouse. *Cancer research*, 44(8), 3522–3529.
40. Sweeney, T. J., Mailänder, V., Tucker, A. A., Olomu, A. B., Zhang, W., Cao, Y. a., Negrin, R. S., & Contag, C. H. (1999). Visualizing the kinetics of tumor-cell clearance in living animals. *Proceedings of the National Academy of Sciences of the United States of America*, 96(21), 12044–12049. <https://doi.org/10.1073/pnas.96.21.12044>
41. Bhang, H. E., Gabrielson, K. L., Larterra, J., Fisher, P. B., & Pomper, M. G. (2011). Tumor-specific imaging through progression elevated gene-3 promoter-driven gene expression. *Nature medicine*, 17(1), 123–129. <https://doi.org/10.1038/nm.2269>
42. Stollfuss, J., Landvogt, N., Abenstein, M., Ziegler, S., Schwaiger, M., Senekowitsch-Schmidtke, R., & Wieder, H. (2015). Non-invasive imaging of implanted peritoneal carcinomatosis in mice using PET and bioluminescence imaging. *European Journal of Nuclear Medicine and Molecular Imaging: Research*, 5(1), 44. <https://doi.org/10.1186/s13550-015-0125-z>
43. Kircher, M. F., Gambhir, S. S., & Grimm, J. (2011). Noninvasive cell-tracking methods. *Nature Reviews Clinical Oncology*, 8(11), 677–688. <https://doi.org/10.1038/nrclinonc.2011.141>
44. James, M. L., & Gambhir, S. S. (2012). A molecular imaging primer: Modalities, imaging agents, and applications. *Physiological Reviews*, 92(2), 897–965. <https://doi.org/10.1152/physrev.00049.2010>
45. Modo, M. (2008). Noninvasive imaging of transplanted cells. *Current Opinion in Organ Transplantation*, 13(6), 654–658. <https://doi.org/10.1097/MOT.0b013e328317a43c>

46. Puaux, A.-L., Ong, L. C., Jin, Y., Teh, I., Hong, M., Chow, P. K. H., Golay, X., & Abastado, J.-P. (2011). A Comparison of Imaging Techniques to Monitor Tumor Growth and Cancer Progression in Living Animals. *International Journal of Molecular Imaging*, 2011, 1–12. <https://doi.org/10.1155/2011/321538>
47. Sadikot, R. T., & Blackwell, T. S. (2005). Bioluminescence imaging. *Proceedings of the American Thoracic Society*, 2(6), 537–512. <https://doi.org/10.1513/pats.200507-067DS>
48. Welsh, D. K., & Noguchi, T. (2012). Cellular bioluminescence imaging. *Cold Spring Harbor protocols*, 2012(8), pdb.top070607. <https://doi.org/10.1101/pdb.top070607>
49. Yao, Z., Zhang, B. S., & Prescher, J. A. (2018). Advances in bioluminescence imaging: new probes from old recipes. *Current opinion in chemical biology*, 45, 148–156. <https://doi.org/10.1016/j.cbpa.2018.05.009>
50. Close, D. M., Xu, T., Sayler, G. S., & Ripp, S. (2011). In vivo bioluminescent imaging (BLI): noninvasive visualization and interrogation of biological processes in living animals. *Sensors (Basel, Switzerland)*, 11(1), 180–206. <https://doi.org/10.3390/s110100180>
51. Iwano, S., Obata, R., Miura, C., Kiyama, M., Hama, K., Nakamura, M., ... & Niwa, H. (2013). Development of simple firefly luciferin analogs emitting blue, green, red, and near-infrared biological window light. *Tetrahedron*, 69(19), 3847–3856.
52. Kuchimaru, T., Iwano, S., Kiyama, M., Mitsumata, S., Kadonosono, T., Niwa, H., Maki, S., & Kizaka-Kondoh, S. (2016). A luciferin analogue generating near-infrared bioluminescence achieves highly sensitive deep-tissue imaging. *Nature Communications*, 7(1), 11856. <https://doi.org/10.1038/ncomms11856>
53. Iwano, S., Sugiyama, M., Hama, H., Watakabe, A., Hasegawa, N., Kuchimaru, T., Tanaka, K. Z., Takahashi, M., Ishida, Y., Hata, J., Shimozono, S., Namiki, K., Fukano, T., Kiyama, M., Okano, H., Kizaka-kondoh, S., Mchugh, T. J., Yamamori, T., Hioki, H., ... Miyawaki, A. (2018). *Moving Animals*. 939(February), 935–939.
54. Rose, A. (1984). *Vision: Human and Electronic*. Plenum Press.
55. Jung, K. O., Jo, H., Yu, J. H., Gambhir, S. S., & Pratz, G. (2018). Development and MPI tracking of novel hypoxia-targeted theranostic exosomes. *Biomaterials*, 177, 139–148. <https://doi.org/10.1016/j.biomaterials.2018.05.048>
56. Parkins, K. M., Melo, K. P., Ronald, J. A., & Foster, P. J. (2020). Visualizing tumour self-homing with magnetic particle imaging. *BioRxiv*. <https://doi.org/10.1101/2020.02.17.953232>
57. Melo, K. P., Makela, A. V, Hamilton, A. M., & Foster, P. J. (2020). Development of Magnetic Particle Imaging (MPI) for Cell Tracking and Detection. *BioRxiv*. <https://doi.org/10.1101/2020.07.12.197780>

58. Knier, N. N., & Foster, P. J. (2021). Tracking cancer cells in the mouse brain with magnetic resonance imaging (MRI) and magnetic particle imaging (MPI). (2021). *International Society for Magnetic Resonance in Medicine*. <https://www.ismrm.org/21/program-files/TeaserSlides/TeasersPresentations/1213-Teaser.html>
59. Makela, A. V., Schott, M. A., Sehl, O. C, Gevaert, J. J., Foster, P. J., Contag, C. H. (2021). Tracking the fates of iron-labeled tumor cells in vivo using Magnetic Particle Imaging. *BioRxiv*. <https://doi.org/10.1101/2021.10.06.463387>.
60. Liu, S., Nyström, N. N., Kelly, J. J., Hamilton, A. M., Fu, Y., & Ronald, J. A. (2021). Molecular Imaging Reveals a High Degree of Cross-Seeding of Spontaneous Metastases in a Novel Mouse Model of Synchronous Bilateral Breast Cancer. *Molecular Imaging and Biology*. <https://doi.org/10.1007/s11307-021-01630-z>
61. Ichise, H., Tsukamoto, S., Hirashima, T., Konishi, Y., Oki, C., Tsukiji, S., Iwano, S., Miyawaki, A., Sumiyama, K., Terai, K., & Matsuda, M. (2021). Metastatic Single Tumor Cells Evade NK Cell-mediated Killing by Thrombin-mediated Loss of the Activating Ligand CD155/PVR/Necl-5. *BioRxiv*.
62. Sehl, O. C., Foster, P. J. (2021). The sensitivity of magnetic particle imaging and fluorine-19 magnetic resonance imaging for cell tracking. *BioRxiv*, <https://doi.org/10.1101/2021.08.31.458286>
63. Gevaert, J. J., Fink, C., Dikeakos, J., Dekaban, G. A., Foster, P. J. (2021). Magnetic Particle Imaging is a sensitive *in vivo* imaging modality for the quantification of dendritic cell migration. *BioRxiv*, <https://doi.org/10.1101/2021.09.22.461401>
64. Amadeo, F., Plagge, A., Chacko, A., Wilm, B., Hanson, V., Liptrott, N., Murray, P., & Taylor, A. (2021). Firefly luciferase offers superior performance to AkaLuc for tracking the fate of administered cell therapies. *European Journal of Nuclear Medicine and Molecular Imaging*. <https://doi.org/10.1007/s00259-021-05439-4>
65. Makela, A. V., Murrell, D. H., Parkins, K. M., Kara, J., Gaudet, J. M., & Foster, P. J. (2016). Cellular imaging with MRI. *Topics in Magnetic Resonance Imaging*, 25(5), 177–186. <https://doi.org/10.1097/RMR.000000000000101>
66. Su, Y., Walker, J., Park, Y., Smith, T., Liu, L., Hall, M., Labanieh, L., Hurst, R., Wang, D., Encell, L., Kim, N., Zhang, F., Kay, M., Casey, K., Majzner, R., Cochran, J., Mackall, C., Kirkland, T., & Lin, M. (2020). Novel NanoLuc substrates enable bright two-population bioluminescence imaging in animals. *Nature Methods*, 17, 1–9. <https://doi.org/10.1038/s41592-020-0889-6>
67. Rivera-Rodriguez, A., Hoang-Minh, L. B., Chiu-Lam, A., Sarna, N., Marrero-Morales, L., Mitchell, D. A., & Rinaldi-Ramos, C. M. (2021). Tracking adoptive t cell immunotherapy using magnetic particle imaging. *Nanotheranostics*, 5(4), 431–444. <https://doi.org/10.7150/ntno.55165>

## Chapter 3

This chapter serves to summarize the findings presented in this thesis, as well as to highlight limitations and future work.

### 3.1 Chapter 2 Summary and Discussion

The experiments conducted in this thesis were done with the overarching goal of developing a multimodal preclinical imaging system for quantitative and sensitive tracking of breast cancer cells *in vivo*. MPI and Akaluc BLI were chosen as our core imaging modalities as we believe their individual characteristics could complement one another to give a more complete picture of cell fate and biodistribution. MPI offers remarkable specificity, positive hotspot imaging, and the ability to quantify cells based on the concentration of iron within them, all without the use of radiation. Additionally, there are no depth effects associated with MPI, allowing for deep tissue imaging (1-8). Despite these advantageous characteristics, MPI is limited by poor spatial resolution (9), and limited sensitivity compared to other modalities such as MRI (10-15). Additionally, being a probe-based system, MPI cannot provide a measure of cell viability or proliferation for dividing cell populations over time (12-17).

BLI on the other hand is an optical imaging system, often used as a marker for cell viability and proliferation over long durations (18-25). Due to light attenuation by tissues, traditional FLuc BLI is limited by depth effects, low 3D spatial resolution, and low sensitivity for deeply situated tissues (18,26-29). Akaluc BLI utilizes NIR light, which has lower attenuation in biological tissue. This has allowed for single cell sensitivity for deeply situated cells (30-32).

Our work successfully combined these two modalities, demonstrating for the first time, the ability to track transplanted cells with MPI and Akaluc BLI. Dual labelled (Akaluc and the SPIO Synomag-D), implanted into the mammary fat pad of nude mice were visualized and quantified on MPI and Akaluc BLI over a 2-week period. The location of the signal for both MPI and Akaluc BLI corresponded to the location of the primary tumour (as confirmed through *ex vivo* histology), indicating successful cell implantation. From Day 1 to day 14, the MPI signal decreased by 40%, corresponding to a 1.57  $\mu\text{g}$  decrease in iron content. This can likely be attributed to a combination of cell proliferation, dispersion,



and clearance. The continued decrease in signal may suggest that MPI cannot be used to indefinitely track proliferating cell populations, especially for experiments where lower cell numbers are initially implanted. Conversely, the signal produced in Akaluc BLI increased by orders of magnitude over the course of the experiment (28-fold increase), demonstrating the ability of Akaluc BLI to track rapid cell proliferation in cancer models.

Secondary signals, separate from the primary tumour were observed on day 13/14 of this experiment on both Akaluc BLI and MPI. It is possible that these secondary signals corresponded to metastases, as highlighted by the *ex vivo* histology of a BLI positive lymph node. What was interesting about these findings was that when the Akaluc BLI and MPI scans were overlaid it was clear that the same secondary signal locations were not seen on Akaluc BLI and MPI. Instead, each modality was able to visualize completely unique cell locations. Akaluc BLI detected signal from mice in the ipsilateral and contralateral armpits, as well as the upper mid right abdomen. A major limitation in the detection of these signals, however, was that a dark covering was needed to prevent camera saturation by the intense primary tumour. This prevented visualization of regions in the lower half of the mouse, close to the primary tumour. MPI detected signals from the right footpad, the epigastric region, and the right middle abdominal quadrant.

For a few reasons, we believe that Akaluc BLI may be more sensitive than MPI for detection of potential metastases. First, literature has demonstrated that Akaluc BLI has single cell sensitivity *in vivo* (32), while the highest reported sensitivity for MPI is 200-250 cells (33,34). Second, by the time secondary lesions form, multiple cell passages have already occurred, resulting in dilution of SPIO. Based on this, it is possible that cells seeding the secondary lesion fall below the threshold for detection. Further, when Akaluc transduced cells seed a metastasis, their continued proliferation will increase the BLI signal in the tissue. This theory is supported by the *ex vivo histology*, in which cells of the metastatic lymph node were positive for the transduced reporter construct but did not contain detectable iron. The increased sensitivity resulting from these factors allowed Akaluc BLI to detect signal from regions distal to the primary tumour, however, due to the required shielding Akaluc BLI could not detect potential metastases proximal to the primary tumour. No shielding was required for MPI allowing the visualization of proximal lesions, previously covered for BLI. These findings give credence to the belief that combining imaging modalities, in this case Akaluc BLI and MPI can give a more complete picture of cell fate. By limiting research to a single modality, researchers run the risk of missing important information due to limitations inherent to the modality.

A key aspect of MPI is that iron content is directly and linearly quantitative based on generated signal. This allows us to calculate the amount of iron present in a region based on the signal it produces (2-8). In order to do this, calibration lines were made for all scan modes used in the experiment. The slopes of these lines can then be used to calculate unknown iron concentration. This method was used for both the *in vivo* experiments listed above, as well as for determining an *in vitro* detection limit of 8000 Synomag-D labelled cells with a 3D scan. This limit was possible due to nearly 4-fold increase in sensitivity offered by Synomag-D in comparison to Vivotrax, as shown by the relaxometry data. While more sensitive than Vivotrax, other MPI tracers have shown higher sensitivity which could be used to improve dual tracking with MPI and Akaluc BLI (34,35).

## 3.2 Challenges and Limitations of MPI

### 3.2.1 Contamination

The MPI system can easily become contaminated due to the presence of iron in a variety of common lab materials. Examples of this includes residual iron from dust, scissor cuts, paper towels, dirt from shoes, and specific tapes. If this iron contaminates the bore or bed of the MPI, it can result in signal, causing unwanted hotspots, or a higher-than-average background signal. As the SNR of an image is calculated using the background of an empty bed scan, contamination will decrease the cell detection sensitivity of MPI. Early on during my MPI experiments, our lab had a contamination problem which made any data collected at that time unusable. *In vitro* calibration, and cell detection experiments needed to be repeated before a solution was found to the contamination issue.

Our lab has introduced protocols to minimize the amount of contamination present. A plastic shield has been installed to cover the bore of the MPI. This covering is left on at all times unless a scan is being conducted. Secondly beds are cleaned with 70% ethanol prior to use and wiped down thoroughly with Kimwipes. A compressed air hose was installed to the wall of the MPI use to blow out any serious contaminants inside the bore, or on the bed. All lab surfaces, equipment, and floors are regularly cleaned to minimize dust and dirt build up. These protocols have significantly reduced the amount and frequency of contamination.

### *3.2.2 Unwanted sources of signal*

Mice scanned with MPI occasionally show a large gastrointestinal signal, even in the absence of an injected tracer. We have concluded that this is due iron present in mouse feed, and some beddings. This is especially concerning when trying to quantify low cell numbers or looking at an area close to the gut region. Our lab has minimized this limitation by fasting mice for 12 hours prior to scanning, as well as replacing bedding with a corn-based alternative, as described by Gevaert et al., in 2021 (36). This technique was used in this thesis, and as a result gut signal fell below the threshold of detection, although it is possible that small traces of this contamination remain.

### *3.2.3 MPI hardware failure*

In March of 2021, a resistor for the x transmit channel had to be replaced. This hardware failed due to overheating. This occurred during my 3D Calibration experiment, resulting in all acquired data to be unusable. Data for the 3D calibration line had to be recollected on a later date. To avoid this problem in the future it was advised that the MPI system should not be in operation for more than 5 hours at a time. After this time, a 2 hour cool down period is needed to ensure that no hardware components overheat.

### *3.2.4 Limitations of MPI*

As MPI is still an emerging imaging modality, the limitations associated with MPI have not been fully flushed out. The primary limitation associated to MPI is the low spatial resolution. This makes the delineation of signal from closely situated regions difficult. Often signal is summated, producing one larger combined signal rather than smaller individual signals. Although this wasn't a concern for this project, future experiments may be impacted by this. While resolution is currently a major limitation, it is expected that over time advances in MPI tracer technology will drastically improve the resolution of MPI. An example of this progress can be seen in work done by the Conolly and Rinaldi labs who have recently shown resolution improvements in the order of magnitudes with their superferromagnetic chain tracers (35).

One of the main features of MPI is that only superparamagnetic iron is believed to produce signal. As tissues are paramagnetic, background tissue does not produce a signal (1-8). This serves as both a useful feature and a limitation. No anatomical reference is produced by MPI, making it difficult to register signal to specific organs or tissues. The addition of separate scans from either MRI or CT are required for co-registration of signal. Magnetic Insight has developed a dual MPI/CT system for this

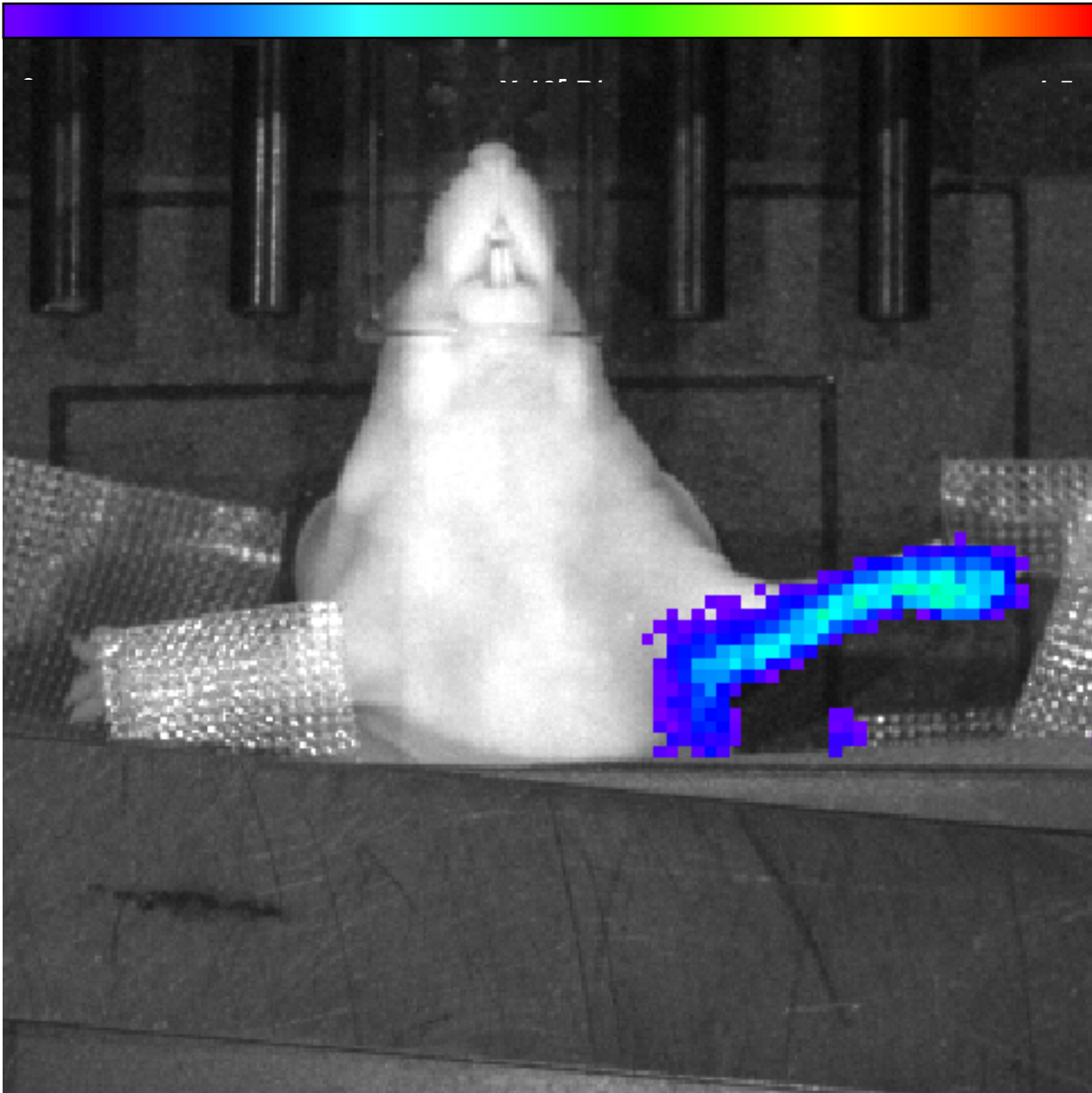
purpose, allowing both MPI signal and anatomical reference to be generated without moving the mouse, or the introduction of time-delays. The MPI system used at Robarts does not have a CT component and rather has a standard camera attached to it. Bright field photographs are taken which can be overlaid on the MPI scan for reference.

As highlighted throughout this thesis, MPI is also subject to many of the limitations prominent in other probe-based imaging modalities. Firstly, MPI cannot be used as a marker of cell proliferation. The concentration of SPIO is diluted upon cell division and may be passed asymmetrically to daughter cells. The dispersion of these cells results in a lower signal for your region of interest. Due to this quantification of cells becomes imprecise at later time points, as the signal is not representative of the number of cells in a region. Further, MPI cannot be used to indefinitely image dividing cell populations (11-13,16,17), although Song et al., demonstrated that over a 20-day period, MPI signal only decreased by approximately 20% (34). Additionally, when cells die, SPIO may be expelled from the cell. This free SPIO will continue to produce a signal. Alternatively, this SPIO can be taken up by bystander cells such as macrophages for hepatic clearance (16, 37) For these reasons, MPI cannot be used as a measure of cell viability. These limitations prompted the additional use of BLI for cell tracking in this thesis.

### 3.3 Challenges and Limitations of BLI

#### 3.3.1. *BLI light scattering*

As BLI is dependent on the detection of light by a CCD camera, it is susceptible to unwanted light scattering. One prominent example of this is light reflecting off the fur or skin of mice, resulting in false signal. This is most pressing for mice with white fur, as white colours deflect light more readily. The use of nude mice in this thesis minimizes this effect, although the skin itself will also scatter light (38). During the *in vivo* experiments for this thesis, one of the 4 mice exhibited this on day 14. A false signal was observed around the arm of the mouse, due to the positioning of the arm relative to the camera. This can be seen in figure 3.1 below. This false signal can cause problems if it masks regions of low cell numbers such as potential metastases.

**Figure 3.1:**

**Figure 3.1 BLI light scattering observed on the arm of a mouse.** One limitation of BLI is that skin and fur will scatter light giving false signal. An example of this was observed in one of the mice during the *in vivo* experiments described in chapter 2. The left arm has a signal due to the scattering of light off the extended arm, making detection of secondary lesions difficult.

### 3.3.2 Akaluc BLI background signal

In a Nature Methods paper published by Su et al., in 2020, they noted that Akalumine produced clear background liver signal in mice, even in the absence of Akaluc. This finding was unique to Akalumine and was not observed for other substrates (39). Nakayama et al., further demonstrated this characteristic of Akalumine and hypothesized that Akalumine is metabolized by the liver to produce micro-luminescence, a trait most often observed in hydrophobic molecules (40). Background signal from the liver reduces the sensitivity of Akaluc BLI, especially when trying to detect signal from small numbers of cells at or around the liver. No liver signal was observed in this experiment. Although hepatic signal was not directly visible in this thesis, this could be a concern in future experiments.

### 3.3.3 BLI Signal Saturation

One limitation of BLI which was especially relevant during this thesis was signal saturation. Due to extreme differences in cell numbers, the signal produced by the primary tumours in this experiment were magnitudes greater than those from secondary lesions. While this high signal gives BLI a high SNR, it also completely masks signal from any other location. Secondary signal sites were not visible in BLI unless an opaque covering was placed on the mouse to shield the signal from the camera. This shield blocked out the entire bottom half of the mouse, preventing the visualization of any region proximal to the primary tumour. This may have resulted in potential sites of metastasis being overlooked in BLI. An alternative solution to this problem would be to excise the primary tumour from the mouse prior to imaging, however, this method is highly invasive.

### 3.3.4 Akalumine Cytotoxicity

Compared to most other BLI substrates, Akalumine-HCl has shown higher cytotoxicity. In 2017, Yeh et al., demonstrated that at a concentration of 500  $\mu\text{M}$ , cell viability of cells in the presence of Akalumine decreased to 40%. At 1000  $\mu\text{M}$  the viability was less than 20%. This was lower than any of the other BLI reporters they tested (diphenylterazine, D-luciferin, Furizamine, and streptozotocin) (41). In 2020, Nakayama et al., saw a rapid fall in heart rate, following the administration of Akalumine via IP injection. It was found that Akalumine had a pH of 2.25, making it highly acidic. They hypothesized that at concentrations greater than 10 mM this resulted in cardiac damage by acidosis. D-luciferin and

the Akalumine derivate seMpai did not exhibit this (40). Additionally, in 2021, Amadeo et al., noticed lesions at the site of subcutaneous injections, not observed with d-luciferin or IP injection. They also hypothesized that this was due to the low pH (42).

### *3.3.5 Limitations of BLI*

As mentioned before, no imaging modality is without its inherent limitations. Historically the biggest limitation associated with BLI is signal attenuation (Sadikot et al., 2005; Kircher et al., 2011; Welsh & Nouguchi, 2012; Yao et al., 2018; Close et al., 2011; Alsawaftah et al., 2021). Biological tissues absorb light, which reduces the amount of signal which can reach the camera. Akaluc BLI significantly minimizes this through its use of NIR light ((Kobayashi et al., 2010), although it is impossible to completely remove this limitation. Signal from more deeply situated tissues will be more attenuated than superficial tissues due to the volume of tissue that the light is interacting with. This gives BLI limited three-dimensional spatial resolution (18,26-31).

Similar to PET, BLI is reliant on substrate availability and kinetics. In order to produce a signal, the luciferin substrate must encounter the luciferase and be catalyzed to produce light. The interaction of substrate and enzyme is random but is heavily influenced by the amount of substrate available to the enzyme (26-29). This has a large impact on the amount of signal being produced. To reduce this effect, Akalumine was administered in excess for this experiment. This, however, leads to the next limitation of BLI: enzyme saturation. As the concentration of substrate increases, the luciferase enzyme will eventually become saturated. Any increases in substrate concentration after this will have no impact on the amount of signal produced. This sets the maximum signal that can be produced by any one cell. It is important to note that the saturation point for Fluc (5.12 mM), is approximately 32-fold greater than that of Akalumine-HCl (160  $\mu$ M) which allows for the administration of more substrate. Amadeo et al., found that when substrates are administered subcutaneously (at saturation concentrations) this will result in Fluc BLI having a higher signal than Akaluc BLI, although the same was not found following intraperitoneal injection of substrates (42).

## **3.4 General Challenges and Limitations**

### *3.4.1 Covid-19 Pandemic*

To state the obvious, the COVID-19 pandemic has created its own set of challenges for everyone. Following Western University protocols, our research lab at Robarts was shut down from mid-March until June 2020. During this time, I was unable to conduct any experiments needed for the progression

of this thesis. Both *in vitro* and *in vivo* experiments were affected by the shutdown. Ongoing cell experiments were prematurely ended, requiring the thawing and recharacterization of a new cell batch post lockdown. Additionally, the start of animal experiments was delayed as the Veterinary Services at Robarts was understaffed, and a preference was given to ongoing experiments. This reduced the number of cohorts which could be used in this experiment. Despite these problems, I completed as many experiments as possible.

### 3.4.2 Limitations of Study

Limitations specific to the experiments conducted in this thesis are listed below:

1. The number of mice used in this experiment (n=4) should be increased to confirm any trends observed in this data.
2. Mice were imaged on MPI and BLI on separate days, limiting the comparison that could be made between the two modalities. This was done to minimize stress on mice, from prolonged isoflurane anaesthesia exposure (20-40 min per scan).
3. Mice were imaged in the supine position for BLI, but the prone position for MPI. This change makes direct comparison of signal locations difficult.
4. No *ex vivo* histology was done to confirm the presence of iron in MPI positive secondary lesions, preventing us from confirming that these were metastases. By the time MPI and BLI scans were aligned, tissues had already been collected and we were unaware that the signals originated from different locations.
5. By day 14, the tumor burden on the mice became too large to continue the experiment. Mice could not be imaged at later dates as originally planned.
6. Labelling cells with Synomag-D may result in extracellular iron. While cells were washed thoroughly to avoid this, it is possible that trace amounts of iron remained which will lead to an overestimation of iron content measure in MPI.
7. Iron content was not calculated using ICP-MS. When this experiment began, our lab did not have access to ICP-MS to precisely measure the amount of iron in each cell. Numbers used in this experiment were calculated from calibration lines, which may be less accurate.

Future work described in the following section could address some of these concerns.



## 3.5 Future Work

### 3.5.1 Short Term Work

This research would benefit from additional mice. Due to time restraints associated with COVID-19, only 4 mice were used in this study. The *in vivo* work described in this study should be repeated with new cohorts of mice to reduce the impact of biological variance, and to draw conclusions about data trends.

For the mouse experiments described in chapter 2, one million dual labelled cells were administered. Later experiments should consider the use of fewer cells. This would serve 2 purposes. First, a lower initial cell number would reduce the tumour burden, allowing for imaging over longer durations and a more in-depth comparison of Akaluc BLI and MPI. Secondly, this may limit the camera saturation observed in BLI at later time points. As the primary signal decreases, secondary lesions may become more visible.

In the summer of 2020, the Foster lab was granted access to an advanced user interface for MPI by Magnetic Insight Inc. This interface allows for fine-tuning of various imaging parameters to optimize image acquisition. Our lab is working on testing out this new interface for future experiments. These changes may increase the sensitivity and resolution of MPI for cell tracking experiments such as the one outlined in this thesis.

This project would benefit from a faster pipeline of aligning BLI and MPI signals at endpoint. By aligning the signals prior to tissue collection, we can ensure that secondary lesions positive for both BLI and MPI can be examined *ex vivo*. This will allow for confirmation of metastases with both modalities.

Since the start of this thesis, new tracers have become available which may improve sensitivity of both MPI and BLI. For MPI we were able to detect as few as 8000 Synomag-D labelled cells *in vitro* (0.02  $\mu\text{g}$  of iron;  $2.18 \pm 0.8$  pg of iron/cell), however researchers have been able to detect as low as 250 cells (7.5 ng of iron; 30 pg iron/cell) (34). If cells were labelled with higher concentrations of iron, fewer cells would be detectable. Tracers such as the superferromagnetic chains developed by Conolly and Rinaldi labs should be considered as they offer superior resolution and sensitivity, although these tracers are currently cytotoxic (35). Recently an analogue of Akalumine has been developed known as seMpai. SeMpai has almost the exact same emission spectra as Akalumine but has better solubility in neutral solutions, which results in lower background hepatic signal. This could be useful in detecting

metastases to the liver or in nearby regions such as the lungs. Additionally, seMpai has a pH of 7.91 making it less cytotoxic than Akalumine-HCl (40).

### 3.5.2 Long-Term Goals

In addition to the short-term work described in section 3.5.3, there are some long-term goals which exceed the scope of this thesis. This was the first paper to apply Akaluc BLI and MPI for tracking of any cell type. We chose to track breast cancer; however, this system could provide unique insight into tracking of any cell type. MPI has been used in literature to track stem cells (43-47), pancreatic islets (48,49), T cells (50), tumor associated macrophages (37), neural progenitor cells (33), dendritic cells (36) and patient derived xenografts (51). It would be interesting to determine what benefits the addition of Akaluc BLI could bring to tracking any of these cell lines. In addition to disease progression, this system could also be used to visualize the efficacy of cell-based therapeutics. Specifically, the Ronald lab is interested in tracking CAR-T and NK cells for immunotherapies. CAR-T cells have been tracked with both MPI and Akaluc BLI independently (39,50).

Different routes of cell administration can result in cells localizing to different locations. This could provide an avenue to test the ability of our Akaluc BLI MPI system for visualizing of cells in different tissue types and organs. For example, intracardiac injection of cells results in approximately 15% of cells arresting in the brain of mice (52). As the brain is one of the most difficult regions to image with standard BLI, it would be interesting to see if this system provides any advantages for this particular application.

We have demonstrated in this thesis, the advantages of combining Akaluc BLI, and MPI for cell tracking, however, there are a plethora of other imaging modalities which could be used to complement this multimodal system. A modality such as CT or MRI which provide anatomical information would make localizing signal locations far easier. A CT/MPI system from Magnetic Insight has recently become available, however our lab does not have access to such a system at this time. Alternatively, MRI which can utilize the same SPIO tracers as MPI may make a simple accompaniment for anatomical reference. MRI would also add a clinical probe-based imaging component which is currently missing in this research. Further, PET could provide clinical reporter

gene imaging for cell tracking. Each modality comes with its own set of advantages which could help provide a more complete picture of cell fate.

### 3.6 Significance and Impact

Here we present for the first time the ability to track breast cancer cells with a dual Akaluc BLI and MPI system. To date, no other cell type has been tracked using this multimodal approach. Akaluc BLI offers a measurement of cell viability and proliferation which can be used in conjunction with the high specificity, and direct quantification capabilities of MPI for long-term tracking of proliferative cell populations. Both Akaluc BLI and MPI were able to detect cells from the primary tumor over the full 2-week study. Secondary lesions, corresponding to potential metastases were detected with both modalities. What is interesting however, is that none of the sites visualized with Akaluc BLI were visible with MPI and visa-versa. While a larger n size is needed to corroborate these results, this data highlights an important example of why these two modalities should be used in conjunction. Use of a single imaging modality may lead to missing important information, giving an incomplete picture of cell fate. The research presented in this thesis lays the groundwork for multimodal Akaluc BLI and MPI cell tracking of various cell types which would give valuable information on both disease progression and the effect of potential therapeutics.

### 3.7 References

1. Gleich, B. (2001). Verfahren zur Ermittlung der räumlichen Verteilung magnetischer Partikel. *German Patent DE-10151778-A1*.
2. Gleich, B., & Weizenecker, J. (2005). Tomographic imaging using the nonlinear response of magnetic particles. *Nature*, *435*(7046), 1214–1217. <https://doi.org/10.1038/nature03808>
3. Wu, L. C., Zhang, Y., Steinberg, G., Qu, H., Huang, S., Cheng, M., Bliss, T., Du, F., Rao, J., Song, G., Pisani, L., Doyle, T., Conolly, S., Krishnan, K., Grant, G., & Wintermark, M. (2019). A Review of Magnetic Particle Imaging and Perspectives on Neuroimaging. *AJNR. American journal of neuroradiology*, *40*(2), 206–212. <https://doi.org/10.3174/ajnr.A5896>
4. Saritas, E. U., Goodwill, P. W., Croft, L. R., Konkle, J. J., Lu, K., Zheng, B., & Conolly, S. M. (2013). Magnetic particle imaging (MPI) for NMR and MRI researchers. *Journal of magnetic resonance (San Diego, California : 1997)*, *229*, 116–126. <https://doi.org/10.1016/j.jmr.2012.11.029>
5. Zheng, B., Yu, E., Orendorff, R., Lu, K., Konkle, J. J., Tay, Z. W., Hensley, D., Zhou, X. Y., Chandrasekharan, P., Saritas, E. U., Goodwill, P. W., Hazle, J. D., & Conolly, S. M. (2017). Seeing SPIOs Directly In Vivo with Magnetic Particle Imaging. *Molecular imaging and biology*, *19*(3), 385–390. <https://doi.org/10.1007/s11307-017-1081-y>
6. Yu, E. Y., Bishop, M., Zheng, B., Ferguson, R. M., Khandhar, A. P., Kemp, S. J., Krishnan, K. M., Goodwill, P. W., & Conolly, S. M. (2017). Magnetic Particle Imaging: A Novel in Vivo Imaging Platform for Cancer Detection. *Nano letters*, *17*(3), 1648–1654. <https://doi.org/10.1021/acs.nanolett.6b04865>
7. Talebloo, N., Gudi, M., Robertson, N., & Wang, P. (2020). Magnetic Particle Imaging: Current Applications in Biomedical Research. *Journal of magnetic resonance imaging*, *51*(6), 1659–1668. <https://doi.org/10.1002/jmri.26875>
8. Sehl, O. C., Gevaert, J. J., Melo, K. P., Knier, N. N., & Foster, P. J. (2020). A perspective on cell tracking with magnetic particle imaging. *Tomography*, *6*(4), 315–324. <https://doi.org/10.18383/j.tom.2020.00043>
9. Tay, Z. W., Hensley, D. W., Vreeland, E. C., Zheng, B., & Conolly, S. M. (2017). The relaxation wall: experimental limits to improving MPI spatial resolution by increasing nanoparticle core size. *Biomedical Physics & Engineering Express*, *3*(3), 035003. <https://doi.org/10.1088/2057-1976/aa6ab6>
10. Hinds, K. A., Hill, J. M., Shapiro, E. M., Laukkanen, M. O., Silva, A. C., Combs, C. A., Varney, T. R., Balaban, R. S., Koretsky, A. P., & Dunbar, C. E. (2003). Highly efficient endosomal labeling of progenitor and stem cells with large magnetic particles allows magnetic resonance imaging of single cells. *Blood*, *102*(3), 867–872. <https://doi.org/10.1182/blood-2002-12-3669>

11. Heyn, C., Ronald, J. A., Mackenzie, L. T., MacDonald, I. C., Chambers, A. F., Rutt, B. K., & Foster, P. J. (2006). In vivo magnetic resonance imaging of single cells in mouse brain with optical validation. *Magnetic resonance in medicine*, 55(1), 23–29. <https://doi.org/10.1002/mrm.20747>
12. Heyn, C., Ronald, J. A., Ramadan, S. S., Snir, J. A., Barry, A. M., MacKenzie, L. T., Mikulis, D. J., Palmieri, D., Bronder, J. L., Steeg, P. S., Yoneda, T., MacDonald, I. C., Chambers, A. F., Rutt, B. K., & Foster, P. J. (2006). In vivo MRI of cancer cell fate at the single-cell level in a mouse model of breast cancer metastasis to the brain. *Magnetic resonance in medicine*, 56(5), 1001–1010. <https://doi.org/10.1002/mrm.21029>
13. Foster, P. J., Dunn, E. A., Karl, K. E., Snir, J. A., Nycz, C. M., Harvey, A. J., & Pettis, R. J. (2008). Cellular magnetic resonance imaging: in vivo imaging of melanoma cells in lymph nodes of mice. *Neoplasia (New York, N.Y.)*, 10(3), 207–216. <https://doi.org/10.1593/neo.07937>
14. Shapiro, E.M., Sharer, K., Skrtic, S. and Koretsky, A.P. (2006), In vivo detection of single cells by MRI. *Magnetic Resonance in Medicine*, 55: 242-249. <https://doi.org/10.1002/mrm.20718>
15. Shapiro, E. M., Medford-Davis, L. N., Fahmy, T. M., Dunbar, C. E., & Koretsky, A. P. (2007). Antibody-mediated cell labeling of peripheral T cells with micron-sized iron oxide particles (MPIOs) allows single cell detection by MRI. *Contrast media & molecular imaging*, 2(3), 147–153. <https://doi.org/10.1002/cmml.134>
16. Amsalem, Y., Mardor, Y., Feinberg, M. S., Landa, N., Miller, L., Daniels, D., Ocherashvilli, A., Holbova, R., Yosef, O., Barbash, I. M., & Leor, J. (2007). Iron-oxide labeling and outcome of transplanted mesenchymal stem cells in the infarcted myocardium. *Circulation*, 116(11 Suppl), I38–I45. <https://doi.org/10.1161/CIRCULATIONAHA.106.680231>
17. Makela, A. V., Murrell, D. H., Parkins, K. M., Kara, J., Gaudet, J. M., & Foster, P. J. (2016). Cellular imaging with MRI. *Topics in Magnetic Resonance Imaging*, 25(5), 177–186. <https://doi.org/10.1097/RMR.000000000000101>
18. Alsawaftah, N., Farooq, A., Dhou, S., & Majdalawieh, A. F. (2021). Bioluminescence Imaging Applications in Cancer: A Comprehensive Review. *IEEE reviews in biomedical engineering*, 14, 307–326. <https://doi.org/10.1109/RBME.2020.2995124>
19. Bu, L., Ma, X., Tu, Y., Shen, B., & Cheng, Z. (2013). Optical image-guided cancer therapy. *Current pharmaceutical biotechnology*, 14(8), 723–732. <https://doi.org/10.2174/1389201014666131226112507>
20. Söling, A., & Rainov, N. G. (2003). Bioluminescence imaging in vivo - application to cancer research. *Expert opinion on biological therapy*, 3(7), 1163–1172. <https://doi.org/10.1517/14712598.3.7.1163>
21. Edinger, M., Sweeney, T. J., Tucker, A. A., Olomu, A. B., Negrin, R. S., & Contag, C. H. (1999). Noninvasive assessment of tumor cell proliferation in animal models. *Neoplasia (New York, N.Y.)*, 1(4), 303–310. <https://doi.org/10.1038/sj.neo.7900048>
22. Kozlowski, J. M., Fidler, I. J., Campbell, D., Xu, Z. L., Kaighn, M. E., & Hart, I. R. (1984). Metastatic behavior of human tumor cell lines grown in the nude mouse. *Cancer research*, 44(8), 3522–3529.

23. Sweeney, T. J., Mailänder, V., Tucker, A. A., Olomu, A. B., Zhang, W., Cao, Y. a., Negrin, R. S., & Contag, C. H. (1999). Visualizing the kinetics of tumor-cell clearance in living animals. *Proceedings of the National Academy of Sciences of the United States of America*, *96*(21), 12044–12049. <https://doi.org/10.1073/pnas.96.21.12044>
24. Bhang, H. E., Gabrielson, K. L., Larterra, J., Fisher, P. B., & Pomper, M. G. (2011). Tumor-specific imaging through progression elevated gene-3 promoter-driven gene expression. *Nature medicine*, *17*(1), 123–129. <https://doi.org/10.1038/nm.2269>
25. Stollfuss, J., Landvogt, N., Abenstein, M., Ziegler, S., Schwaiger, M., Senekowitsch-Schmidtke, R., & Wieder, H. (2015). Non-invasive imaging of implanted peritoneal carcinomatosis in mice using PET and bioluminescence imaging. *European Journal of Nuclear Medicine and Molecular Imaging: Research*, *5*(1), 44. <https://doi.org/10.1186/s13550-015-0125-z>
26. Sadikot, R. T., & Blackwell, T. S. (2005). Bioluminescence imaging. *Proceedings of the American Thoracic Society*, *2*(6), 537–512. <https://doi.org/10.1513/pats.200507-067DS>
27. Welsh, D. K., & Noguchi, T. (2012). Cellular bioluminescence imaging. *Cold Spring Harbor protocols*, *2012*(8), pdb.top070607. <https://doi.org/10.1101/pdb.top070607>
28. Yao, Z., Zhang, B. S., & Prescher, J. A. (2018). Advances in bioluminescence imaging: new probes from old recipes. *Current opinion in chemical biology*, *45*, 148–156. <https://doi.org/10.1016/j.cbpa.2018.05.009>
29. Close, D. M., Xu, T., Sayler, G. S., & Ripp, S. (2011). In vivo bioluminescent imaging (BLI): noninvasive visualization and interrogation of biological processes in living animals. *Sensors (Basel, Switzerland)*, *11*(1), 180–206. <https://doi.org/10.3390/s110100180>
30. Iwano, S., Obata, R., Miura, C., Kiyama, M., Hama, K., Nakamura, M., ... & Niwa, H. (2013). Development of simple firefly luciferin analogs emitting blue, green, red, and near-infrared biological window light. *Tetrahedron*, *69*(19), 3847-3856.
31. Kuchimaru, T., Iwano, S., Kiyama, M., Mitsumata, S., Kadonosono, T., Niwa, H., Maki, S., & Kizaka-Kondoh, S. (2016). A luciferin analogue generating near-infrared bioluminescence achieves highly sensitive deep-tissue imaging. *Nature Communications*, *7*(1), 11856. <https://doi.org/10.1038/ncomms11856>
32. Iwano, S., Sugiyama, M., Hama, H., Watakabe, A., Hasegawa, N., Kuchimaru, T., Tanaka, K. Z., Takahashi, M., Ishida, Y., Hata, J., Shimosono, S., Namiki, K., Fukano, T., Kiyama, M., Okano, H., Kizaka-kondoh, S., Mchugh, T. J., Yamamori, T., Hioki, H., ... Miyawaki, A. (2018). *Moving Animals*. *939*(February), 935–939.
33. Zheng, B., Vazin, T., Goodwill, P. W., Conway, A., Verma, A., Saritas, E. U., Schaffer, D., & Conolly, S. M. (2015). Magnetic Particle Imaging tracks the long-term fate of in vivo neural

cell implants with high image contrast. *Scientific reports*, 5, 14055.  
<https://doi.org/10.1038/srep14055>

34. Song, G., Chen, M., Zhang, Y., Cui, L., Qu, H., Zheng, X., Wintermark, M., Liu, Z., & Rao, J. (2018). Janus Iron Oxides @ Semiconducting Polymer Nanoparticle Tracer for Cell Tracking by Magnetic Particle Imaging. *Nano letters*, 18(1), 182–189.  
<https://doi.org/10.1021/acs.nanolett.7b03829>
35. Tay, Z. W., Savliwala, S., Hensley, D. W., Fung, K. L. B., Colson, C., Fellows, B. D., Zhou, X., Huynh, Q., Lu, Y., Zheng, B., Chandrasekharan, P., Rivera-Jimenez, S. M., Rinaldi-Ramos, C. M., & Conolly, S. M. (2021). Superferromagnetic Nanoparticles Enable Order-of-Magnitude Resolution & Sensitivity Gain in Magnetic Particle Imaging. *Small Methods*, 2100796.  
<https://doi.org/https://doi.org/10.1002/smt.202100796>
36. Gevaert, J. J., Fink, C., Dikeakos, J., Dekaban, G. A., Foster, P. J. (2021). Magnetic Particle Imaging is a sensitive *in vivo* imaging modality for the quantification of dendritic cell migration. *BioRxiv*, <https://doi.org/10.1101/2021.09.22.461401>
37. Makela, A. V., Gaudet, J. M., Schott, M. A., Sehl, O. C., Contag, C. H., & Foster, P. J. (2020). Magnetic Particle Imaging of Macrophages Associated with Cancer: Filling the Voids Left by Iron-Based Magnetic Resonance Imaging. *Molecular imaging and biology*, 22(4), 958–968.  
<https://doi.org/10.1007/s11307-020-01473-0>
38. Edinger, M., Cao, Y. A., Hornig, Y. S., Jenkins, D. E., Verneris, M. R., Bachmann, M. H., Negrin, R. S., & Contag, C. H. (2002). Advancing animal models of neoplasia through *in vivo* bioluminescence imaging. *European journal of cancer (Oxford, England : 1990)*, 38(16), 2128–2136. [https://doi.org/10.1016/s0959-8049\(02\)00410-0](https://doi.org/10.1016/s0959-8049(02)00410-0)
39. Su, Y., Walker, J., Park, Y., Smith, T., Liu, L., Hall, M., Labanieh, L., Hurst, R., Wang, D., Encell, L., Kim, N., Zhang, F., Kay, M., Casey, K., Majzner, R., Cochran, J., Mackall, C., Kirkland, T., & Lin, M. (2020). Novel NanoLuc substrates enable bright two-population bioluminescence imaging in animals. *Nature Methods*, 17, 1–9. <https://doi.org/10.1038/s41592-020-0889-6>
40. Nakayama, J., Saito, R., Hayashi, Y., Kitada, N., Tamaki, S., Han, Y., Semba, K., & Maki, S. A. (2020). High Sensitivity *In Vivo* Imaging of Cancer Metastasis Using a Near-Infrared Luciferin Analogue seMpai. *International journal of molecular sciences*, 21(21), 7896.  
<https://doi.org/10.3390/ijms21217896>
41. Yeh, H. W., Wu, T., Chen, M., & Ai, H. W. (2019). Identification of Factors Complicating Bioluminescence Imaging. *Biochemistry*, 58(12), 1689–1697.  
<https://doi.org/10.1021/acs.biochem.8b01303>
42. Amadeo, F., Plagge, A., Chacko, A., Wilm, B., Hanson, V., Liptrott, N., Murray, P., & Taylor, A. (2021). Firefly luciferase offers superior performance to AkaLuc for tracking the fate of administered cell therapies. *European Journal of Nuclear Medicine and Molecular Imaging*.  
<https://doi.org/10.1007/s00259-021-05439-4>
43. Bulte, J. W., Walczak, P., Janowski, M., Krishnan, K. M., Arami, H., Halkola, A., Gleich, B., & Rahmer, J. (2015). Quantitative "Hot Spot" Imaging of Transplanted Stem Cells using

Superparamagnetic Tracers and Magnetic Particle Imaging (MPI). *Tomography (Ann Arbor, Mich.)*, 1(2), 91–97. <https://doi.org/10.18383/j.tom.2015.00172>

44. Nejadnik, H., Pandit, P., Lenkov, O., Lahiji, A. P., Yerneni, K., & Daldrup-Link, H. E. (2019). Ferumoxytol Can Be Used for Quantitative Magnetic Particle Imaging of Transplanted Stem Cells. *Molecular imaging and biology*, 21(3), 465–472. <https://doi.org/10.1007/s11307-018-1276-x>
45. Lemaster, J. E., Chen, F., Kim, T., Hariri, A., & Jokerst, J. V. (2018). Development of a Trimodal Contrast Agent for Acoustic and Magnetic Particle Imaging of Stem Cells. *American Chemical Society: applied nano materials*, 1(3), 1321–1331. <https://doi.org/10.1021/acsnm.8b00063>
46. Sehl, O. C., Makela, A. V., Hamilton, A. M., & Foster, P. J. (2019). Trimodal Cell Tracking In Vivo: Combining Iron- and Fluorine-Based Magnetic Resonance Imaging with Magnetic Particle Imaging to Monitor the Delivery of Mesenchymal Stem Cells and the Ensuing Inflammation. *Tomography (Ann Arbor, Mich.)*, 5(4), 367–376. <https://doi.org/10.18383/j.tom.2019.00020>
47. Zheng, B., Yu, E., Orendorff, R., Lu, K., Konkle, J. J., Tay, Z. W., Hensley, D., Zhou, X. Y., Chandrasekharan, P., Saritas, E. U., Goodwill, P. W., Hazle, J. D., & Conolly, S. M. (2017). Seeing SPIOs Directly In Vivo with Magnetic Particle Imaging. *Molecular imaging and biology*, 19(3), 385–390. <https://doi.org/10.1007/s11307-017-1081-y>
48. Wang, P., Goodwill, P. W., Pandit, P., Gaudet, J., Ross, A., Wang, J., Yu, E., Hensley, D. W., Doyle, T. C., Contag, C. H., Conolly, S., & Moore, A. (2018). Magnetic particle imaging of islet transplantation in the liver and under the kidney capsule in mouse models. *Quantitative imaging in medicine and surgery*, 8(2), 114–122. <https://doi.org/10.21037/qims.2018.02.06>
49. Hayat, H., Sun, A., Hayat, H., Liu, S., Talebloo, N., Pinger, C., Bishop, J. O., Gudi, M., Dwan, B. F., Ma, X., Zhao, Y., Moore, A., & Wang, P. (2021). Artificial Intelligence Analysis of Magnetic Particle Imaging for Islet Transplantation in a Mouse Model. *Molecular imaging and biology*, 23(1), 18–29. <https://doi.org/10.1007/s11307-020-01533-5>
50. Rivera-Rodriguez, A., Hoang-Minh, L. B., Chiu-Lam, A., Sarna, N., Marrero-Morales, L., Mitchell, D. A., & Rinaldi-Ramos, C. M. (2021). Tracking adoptive T cell immunotherapy using magnetic particle imaging. *Nanotheranostics*, 5(4), 431–444. <https://doi.org/10.7150/ntno.55165>
51. Knier, N. N., & Foster, P. J. (2021). Tracking cancer cells in the mouse brain with magnetic resonance imaging (MRI) and magnetic particle imaging (MPI). (2021). *International Society for Magnetic Resonance in Medicine*. <https://www.ismrm.org/21/program-files/TeaserSlides/TeasersPresentations/1213-Teaser.html>



52. Melo, K. P., Makela, A. V, Knier, N. N., Hamilton, A. M., & Foster, P. J. (n.d.). Magnetic microspheres can be used for magnetic particle imaging of cancer cells arrested in the mouse brain. *Magnetic Resonance in Medicine*, <https://doi.org/https://doi.org/10.1002/mrm.28987>

# Ryan James Williams

(Curriculum Vitae)

## EDUCATION

Sept 2019 – Dec 2021	<b>M.Sc Candidate, Medical Biophysics</b> Western University (UWO) <i>Supervisor:</i> Dr. John Ronald & Dr. Paula Foster <i>Thesis:</i> Exploring Multimodal Cancer Cell Tracking Using Magnetic Particle Imaging and Akaluc BLI	London, ON
Sept 2015 – June 2019	<b>B.Sc Honors Biomedical Sciences</b> University of Waterloo (UW) Minor in Biophysics	Waterloo, ON

## AWARDS AND SCHOLARSHIPS

Sept 2021 – Dec 2021	<b>Western Graduate Research Scholarship</b>	Academic merit (\$5000)	London, ON
Sept 2020 – Aug 2021	<b>Western Graduate Research Scholarship</b>	Academic merit (\$5000)	London, ON
Sept 2019 – Aug 2021	<b>Western Graduate Research Scholarship</b>	Academic merit (\$5000)	London, ON
Sept 2015	<b>University of Waterloo Merit Scholarship</b>	Academic merit (\$1000)	Waterloo, ON

## WORK EXPERIENCE

---

- Apr 2018 – Sept 2018      **Undergraduate Research Assistant**      Toronto, ON  
Princess Margaret Cancer Research Centre  
Comparison of Various CRISPR - Cas9  
Systems for Acute Myeloid Leukemia
- Apr 2017 – Sept 2017      **Undergraduate Research Assistant**      Toronto, ON  
Princess Margaret Cancer Research Centre  
Targeting Mitochondrial Translation to  
Overcome Venetoclax Resistance in Acute  
Myeloid Leukemia

## PUBLISHED ABSTRACTS

---

- 1) Williams, R., Ronald, J., Foster, P. (2021). Exploring Dual Magnetic Particle Imaging (MPI) and Akaluc Bioluminescence Imaging (BLI) for In Vivo Cell Tracking. *World Molecular Imaging Society*.
- 2) Williams, R., Foster, P. J., Ronald J.A. (2021) Exploring Dual Magnetic Particle Imaging (MPI) and Akaluc Bioluminescence Imaging (BLI) for In Vivo Cell Tracking. London Health Research Day.
- 3) Sharon, D., Cathelin, S., Subedi, A., Williams, R., Benicio, M., Ketela, T., Chan., S. (2017). Targeting Mitochondrial Translation Overcomes Venetoclax Resistance in Acute Myeloid Leukemia (AML) through Activation of the Integrated Stress Response. American Society of Hematology: *Blood* 130 (Supplement 1): 297.

## INVITED PRESENTATIONS

---

- 1) Exploring Dual Magnetic Particle Imaging (MPI) and Akaluc Bioluminescence Imaging (BLI) for In Vivo Cell Tracking. World Molecular Imaging Congress. Virtual. October 2021.
- 2) Exploring Dual Magnetic Particle Imaging (MPI) and Akaluc Bioluminescence Imaging (BLI) for In Vivo Cell Tracking. Poster Presentation. London Health Research Day. Virtual. London, ON. May 2021.